POLAR SEA ICE MAPPING FOR SEAWINDS

by

Hyrum S. Anderson

A thesis submitted to the faculty of

Brigham Young University

in partial fulfillment of the requirements for the degree of

Master of Science

Department of Electrical and Computer Engineering

Brigham Young University

August 2003

BRIGHAM YOUNG UNIVERSITY

GRADUATE COMMITTEE APPROVAL

of a thesis submitted by

Hyrum S. Anderson

This thesis has been read by each member of the following graduate committee and by majority vote has been found to be satisfactory.

Date	Dr. David G. Long, Chair
Date	Dr. Karl F. Warnick
Date	Dr. Travis E. Oliphant

BRIGHAM YOUNG UNIVERSITY

As chair of the candidate's graduate committee, I have read the thesis of Hyrum S. Anderson in its final form and have found that (1) its format, citations, and bibliographical style are consistent and acceptable and fulfill university and department style requirements; (2) its illustrative materials including figures, tables, and charts are in place; and (3) the final manuscript is satisfactory to the graduate committee and is ready for submission to the university library.

Date

Dr. David G. Long
Chair, Graduate Committee

Accepted for the Department

Dr. A. Lee Swindlehurst
Graduate Coordinator

Accepted for the College

Dr. Douglas M. Chabries
Dean, College of Engineering and Technology

ABSTRACT

POLAR SEA ICE MAPPING FOR SEAWINDS

Hyrum S. Anderson

Department of Electrical and Computer Engineering

Master of Science

In recent years, the scientific community has expressed interest in the ability to observe global climate indicators such as polar sea ice. Advances in microwave remote sensing technology have allowed a large-scale and detailed study of sea ice characteristics. This thesis provides the analysis and development of sea ice mapping algorithms for the SeaWinds scatterometer. First, an in-depth analysis of the Remund Long (RL) algorithm for SeaWinds is performed. From this study, several improvements are made to the RL algorithm which enhance its performance. In addition, a new method for automated polar sea ice mapping is developed for the SeaWinds instrument. This method is rooted in Bayes decision theory, and incorporates an adaptive model for seasonally fluctuating sea ice and ocean microwave signatures. The new approach is compared to the RL algorithm, to passive microwave data, and to high-resolution SAR imagery for validation.

ACKNOWLEDGMENTS

Special thanks to my advisor, Dr. David Long, for his guidance and encouragement as my research ability was being developed. He had the wisdom to allow me to develop my creativity in approaching a problem. This has required him to see beyond the dead ends. From this I have learned something of patience and Long-suffering.

To my good family I owe an appreciation for work, and an invaluable sense of perspective. I have always been encouraged by my father and mother to secure advanced education. I have been inspired by my parents and each of my ten siblings to pursue real meaning and lasting happiness. I am fortunate to be called their son and brother.

Although silent on the matter, many choice experiences are interwoven with my educational experience at BYU that culminates with this thesis.

Contents

List of Tables

List of Figures

Chapter 1

Introduction

The primary method used today for determining polar sea ice extent is remote sensing. Microwave remote sensing instruments, in particular, have shown great utility in their ability to retrieve information about polar sea ice with good temporal and spatial resolution. Several methods have been developed to retrieve sea ice parameters such as density, type and extent. These methods have been developed for passive microwave sensors (radiometers), synthetic aperture radar (SAR), and for active microwave sensors (scatterometers). The contributions in this thesis represent progress in the accuracy of automated polar sea ice mapping methods using data from the SeaWinds scatterometer.

Scatterometers are active microwave instruments which measure the amount of returned microwave energy from a distributed target. Unlike radiometers, which measure microwave energy (brightness temperature) emitted naturally from objects above 0 K, scatterometers illuminate the objects of interest and measure how much energy is reflected back. For radiometers, the magnitude of the brightness temperature is a function of physical temperature and the emissivity of the object. For scatterometers, the returned power (related to the radar cross section, or RCS) is a function of the permittivity and physical roughness of the object.

In the early days of radar, clutter from the ocean contaminated radar returns from ships. It was later found that this sea clutter was a function of speed and direction of the wind which agitated the ocean's surface. Today, one of the principal uses of scatterometers is inferring near-surface wind speed and direction over the ocean. However, scatterometers are used for a variety of other applications.

Prior to the advent of remote sensing instruments, a thorough study of the cryosphere was impossible. The cryosphere (from the Greek word *kryos*, meaning frost) includes all portions of the Earth's surface water in solid form. This region includes freshwater ice, permafrost, glaciers, icebergs, and polar sea ice. The latter is rather inaccessible for large scale scientific research. Until remote sensing data became available, the extent of polar sea ice was regularly monitored mostly by ships and coastal stations. Such data were sparse, both spatially and temporally.

Sea ice observation from spaceborne instruments has evolved over three decades. The first images were from optical and infrared instruments aboard polar orbiting satellites. These images, however, were hampered by extensive cloud cover and months of complete darkness in the polar regions. Observation methods using microwaves, which are able to penetrate clouds and are not dependent on light conditions, became highly useful. The first passive microwave remote sensing systems for Earth observation were launched by Russia on the Cosmos 243 and Cosmos 384 satellites in 1968 and 1970, and later by the U.S. on the Nimbus 5 satellite in 1972 [1]. The first regular monitoring of polar sea ice was done by the the Scanning Multichannel Microwave Radiometer (SMMR) aboard the Nimbus 7 satellite in 1978. This mission was highly successful, and was continued by a series of other radiometer missions. The first of the Special Sensor Microwave/Image (SSM/I) instruments was launched in 1987 by the Defense Meteorological Satellite Program (DMSP), the same year that the SSMR instrument failed. SSM/I instruments have continued to operate through the present. Together, SMMR and the series of SSM/I instruments provide a nearly uninterrupted set of radiometer data of the polar regions dating back to 1978.

The first spaceborne earth-observation scatterometer, the SeaSat-A Satellite Scatterometer (SASS), was launched in 1978. Its primary purpose was to infer wind speed and direction over the ocean. The system produced imagery covering many millions of square kilometers of ocean, land, and sea ice. Although the mission was only operational from June to October, its success prompted future missions. Among these were the European Space Agency's Remote Sensing Satellite-1 (ERS-1) in 1991, ERS-2 in 1995, and the NASA Scatterometer (NSCAT) in 1996. NSCAT operated

from September 1996 until June 1997, when power failure on the platform prematurely terminated the mission. The QuikSCAT (or QSCAT) mission, a quick replacement for NSCAT, was launched in 1999 and is currently operational. The SeaWinds scatterometer aboard QSCAT is primarily a wind scatterometer, as the name implies. The SeaWinds instrument aboard the Advanced Earth Observing Satellite-2 (ADEOS-II) was launched in late 2002 as an anticipated replacement for SeaWinds on QSCAT. However, at the time of printing of this thesis, ADEOS-II data were still unavailable. With both SeaWinds instruments operational, we will enjoy joint-SeaWinds data with collection times separated by only 6 hours.

SAR instruments represent another important group of sensors used for monitoring polar sea ice. The first spaceborne SAR was launched with SASS in 1978. Additional SAR have been launched with ERS-1 and ERS-2. Perhaps the most notable use of SAR on a large scale is RadarSat, launched in 1995 by the Canadian Space Agency. SAR systems, in general, provide high resolution, but have very limited coverage. In this thesis, RadarSat images are used for validation purposes.

Microwave remote sensing instruments give scientists the ability to study polar sea ice in a way not possible with *in situ* data. *In situ* measurements, however, still hold an important place in the science of polar sea ice, particularly because of their first-hand nature—they are viewed as reliable. Due to the scarcity of *in situ* data and the difficulty in attaining measurements, scientists rely on studying sea ice indirectly through remote sensing instruments. For this reason, we hope that the reliability of microwave data for polar sea ice studies will continue to advance. This thesis presents a method for polar sea ice mapping which can be used with confidence in polar sea ice studies.

1.1 The Importance of Polar Sea Ice

The past several decades have seen a heightened interest in polar sea ice. This interest has stemmed mainly from the realization that conditions in the polar regions are linked to global climate change. In fact, polar sea ice is a crucial factor in many geophysical phenomena. It also affects biological and human activities.

Sea ice is an important component in several geophysical processes. The degree to which sea ice affects these processes is largely a function of its extent and thickness distribution. Sea ice acts as a barrier to the exchange of gases between the ocean and the atmosphere. It also insulates the relatively warm ocean from the colder atmosphere. Near-surface ocean water, whose brine content prohibits its temperature from falling below -1.9° C, experiences diminished heat loss of up to two orders of magnitude when insulated by sea ice. In addition, sea ice dramatically increases the albedo of the ocean surface, causing much of the incoming solar energy to be reflected back into space. Sea ice is also important in oceanic geophysical processes. During the formation of sea ice, salt rejected from the formation of ice structures alters the salinity and density of the surrounding ocean water. This process contributes to vertical convection currents that lift minerals from deeper ocean to the surface. Conversely, melting sea ice creates a thin layer of nearly fresh water at the ocean surface.

Despite the uninhabitable appearance of the polar regions, polar sea ice, in fact, supports a diverse biota. On the microscopic scale, a sympagic community of unicellular organisms exist in brine pockets that form within the ice. These ice organisms tolerate a wide range of environmental conditions. They experience large fluctuations in light intensity, temperature and salinity which vary with the dynamics of sea ice. On a larger scale, a variety of polar vertebrates depend on polar sea ice. For example, polar bears use sea ice for migration and as a platform for hunting seals. The seals feed on Arctic cod that dwell beneath sea ice floes. In the Antarctic, krill feed on the phytoplankton that depend on algae within the sea ice, and in turn provide a major food source for larger animals such as whales, seals, and penguins. The ecosystems involved are extremely intricate and dependent on the dynamics of polar sea ice.

The importance of polar sea ice is not solely an issue of climate or biology. The cyclic nature of polar sea ice growth and retreat affects human activities. Shipping and transportation vessels must carefully schedule voyages so that collisions with icebergs or large floes may be circumvented. For example, raw materials such as oil

and coal must be transported out of the Arctic during periods of low ice concentration. The most notable tragedy of a transportation vessel is, of course, the sinking of the "unsinkable" Royal Mail Ship *Titanic* in 1912.

Recently, a knowledge of polar sea ice extent has been used to refine wind vector fields over open ocean using wind scatterometers. Wind speed and direction are inferred from the radar cross-section of the ocean surface, which is affected by small-scale capillary waves induced by near-surface winds. For complete global coverage, ice extent maps are required to determine where valid regions of open ocean are located. Polar sea ice is highly variable: ice extent varies from approximately 9 million to 19 million square kilometers in the Antarctic, and from approximately 4 million to 15 million square kilometers in the Arctic. In order to retrieve an extensive map of wind vector fields, daily knowledge of sea ice extent is required. These precise wind speed and direction measurements are used in weather models for weather forecasting.

In summary, remote sensing provides a way to indirectly analyze many of the issues described above. Scientists have developed methods to extract many of these geophysical parameters from the microwave signatures of sea ice. Many such methods have yet to be developed. The research described in this thesis contributes to the problem of inferring polar sea ice extent from microwave signatures of the Earth's surface. This information is crucial in a variety of studies including total spatial extent, sea ice thickness (which influences heat transfer), sea ice motion (ocean currents and winds), surface concentration (spatial coverage of ice vs. open ocean), surface melting, snow distribution, sea ice salinity (brine concentration), and many other parameters linked with global climate change.

1.2 Research Problem Description

The scientific community has a great interest in many of the sea ice parameters mentioned above. These parameters must be known with sufficient accuracy and spatial/temporal resolution in order to understand how they interact with other geophysical processes. Thus, sea ice extent estimates must be known with similar accuracy and resolution.

The accuracy of polar sea ice extent maps can be measured by two metrics. First, the ice edge must be close to the true ice edge. "Ice edge" can be misleading here. In the winter, the ice in many cases has a fairly abrupt edge. However, in the melt season or during a storm, the ice edge can be somewhat diffuse. Thus, the accuracy of ice extent maps can be measured by how closely the reported edge follows some predefined concentration contour, such as 15%.

Secondly, the accuracy of ice extent estimates can be determined by the number of misclassifications, where ice is labeled ocean or vice versa by the algorithm. Algorithms make this confusion because in some instances the microwave signature of open water "looks like" the signature of sea ice. Microwave signatures of sea ice can vary greatly, depending on the age, composition, thickness, and surface roughness of the ice. Algorithms for scatterometers typically depend on the power return over areas of sea ice (looking off-nadir) to discriminate between sea ice and ocean, or classify the sea ice. The high power return from sea ice is due to surface and volume scattering in the ice. Ocean typically has low normalized RCS values, which makes discrimination simple. However, during a storm, wind induces capillary waves on the ocean surface which increases the surface roughness, and therefore the off-nadir reflectivity. This is, in fact, the very principle used in determining near-surface wind speed and direction from wind scatterometers. However, the high-power returns from the ocean surface associated with high wind speed can confuse ice detection algorithms ("one man's signal is another man's noise").

As discussed previously, microwave remote sensing instruments typically provide high spatial coverage. For example, with the exception of a small no-coverage gap directly at the poles, the SeaWinds instrument provides 100% coverage of the polar regions each day. In addition, microwave sensors are not hampered by the lack of solar illumination to collect measurements of the surface. They also are less sensitive to atmospheric distortions than optical instruments. This is particularly an issue in the polar regions where extensive cloud cover is common.

Although radiometers and scatterometers provide excellent spatial coverage, this benefit comes at the expense of spatial resolution. Synthetic aperture radar

(SAR) systems provide excellent resolution, but low coverage. In an effort to enhance the spatial resolution of radiometers and scatterometers, image reconstruction techniques are employed. These methods use multiple passes of a satellite instrument to increase surface sampling. In effect, it is a tradeoff between temporal and spatial resolution. The reconstruction technique uses the irregularly spaced surface samples to retrieve high spatial frequency information from the attenuated side lobes of the footprint pattern. While this increases resolution, it also amplifies noise in the reconstructed image which can adversely affect sea ice mapping when the image is used as an input.

Methods to map polar sea ice extent must be relatively insensitive to noise caused from the turbulent ocean and from reconstruction techniques. In addition, methods should maximize effective temporal and spatial resolution. It is undesirable to reduce noise through a temporal or spatial low-pass filter.

A polar sea ice extent algorithm for SeaWinds on QSCAT was developed by Remund and Long [2, 3]. This method is based on an iterative maximum likelihood (ML) approach where sea ice and ocean distributions are assumed to be Gaussian; however, in many cases, sea ice and ocean statistics do not fit the Gaussian model. In some cases, this leads to misclassification in the sea ice extent algorithm. Nevertheless, the Remund-Long algorithm is effective, and at the time of this print is used by NASA's JPL for wind retrieval and by NOAA for sea ice studies. An algorithm which does not assume that sea ice statistics are Gaussian can be expected to perform better.

In summary, various sources of noise and modeling errors can contribute to degrade the performance of sea ice extent algorithms. The aim of this research is to provide high resolution (temporal and spatial) ice extent maps using a method that is relatively insensitive to noise, dynamic with varying ice and ocean statistics, and generally robust in operation. In this thesis, the Remund-Long algorithm is modified to deal with non-Gaussian sea ice statistics, and to properly filter misclassification errors. In addition, a new algorithm is developed which incorporates statistical and spatial *a priori* information to generate accurate sea ice extent estimates.

1.3 Research Contributions

Several contributions are made by this research in the field of remote sensing of polar sea ice. These contributions include (1) an analysis of the seasonal dependence of sea ice and open ocean statistics as observed with the SeaWinds scatterometer, (2) improvements to the Remund-Long algorithm for SeaWinds, and (3) a new sea ice extent mapping algorithm for SeaWinds. In addition, valuable contributions are made in the implementation of Bayes detection and modeling, namely the use of variable loss functions in Bayes detection, and the use of the Karhunen-Loeve transform to parameterize empirical distributions.

The first contribution is an in-depth analysis of polar sea ice and open ocean statistics of Ku-band scatterometer data. In this study, it is found that the statistics vary greatly with season. During the melt season, distributions deviate significantly from Gaussian. The Gaussian model used in the method developed by Remund and Long [2, 3] performs poorly in these conditions.

Modifications are made to the Remund-Long algorithm to improve its performance based on the analysis of the algorithm. First, the algorithm is modified to prevent divergence. Secondly, modifications to the binary processing phase of the algorithm (sea ice growth/retreat constraints) increase autonomy be improving the algorithm's ability to recover from poor prior information. These changes are have been implemented at NOAA and JPL in the operational code.

These contributions give sufficient motivation for the next contribution—a new algorithm for polar sea ice mapping using SeaWinds data. The new method is developed within the framework of Bayes detection, where statistical and spatial *a priori* information are used to yield a better estimate of sea ice extent. This method is designed to adapt to temporal (seasonal) changes in the microwave signatures of polar sea ice, without the heavy dependence of binary processing that is used in the Remund-Long algorithm. This work has been submitted to the journal *IEEE Transactions on Geoscience and Remote Sensing* for publication.

Since statistics deviate from Gaussian during the melt season, a new model is developed which is able to capture a wide range of distributions. The new method

uses an empirical distribution which is parameterized using a truncated set of the principal components (PCs) of the set of previously observed distributions. There are several advantages to parameterizing an empirical distribution in this way. First, a sophisticated distribution can be represented by relatively few parameters. Secondly, the parameterized distribution conforms to the set of expected distributions, i.e., poor statistical information captured in the empirical histogram is rejected (filtered out) when reconstructed from the PCs.

The empirical model solution to non-Gaussian statistics is readily facilitated within the framework Bayes detection. In addition, the loss functions used in Bayes detection theory are related to the expected position of polar sea ice. In this way spatial *a priori* information is incorporated in the detection algorithm.

In summary, this thesis provides important contributions to the field of microwave remote sensing of the polar regions. It is a multidisciplinary endeavor, utilizing concepts from multivariate stochastic signal processing, detection and estimation theory, electromagnetic theory, and image processing.

1.4 Thesis Outline

The research presented in this thesis covers two major topics—algorithm (and statistical) analysis and algorithm development. A synopsis of each chapter is given in the following paragraphs.

Chapter 2 provides general background information needed for an understanding of the discussed research. An overview and specifications of the remote sensing instruments used in this thesis is reported. In addition, the image reconstruction techniques used to generate the enhanced resolution imagery for the study is described. Chapter 2 also provides an overview of the Remund-Long algorithm for SeaWinds [3, 4]. This information provides a basis for the subsequent chapters.

In Chapter 3, an analysis is performed on the Remund-Long algorithm for SeaWinds. The convergence characteristics of the algorithm are explored. It is found that the algorithm is unstable under certain conditions. Non-Gaussian statistics during the melt season cause the Gaussian model to perform poorly. The study

suggests an approach to avoid algorithm divergence. Binary methods are employed to improve algorithm performance. This study also motivates a new histogram-based model, which does not rely as heavily on post-processing binary methods.

The first chapters provide sufficient background for Chapter 4, which details a new approach for polar sea ice extent mapping. This includes the development of the empirical distribution, parameterized by a truncated set of principal components, as discussed above. It also includes the implementation of Bayes detection theory to incorporate spatial and statistical *a priori* information. The adaptive nature of the algorithm performs well in both summer and winter conditions, and is not hampered by a significant need for post-processing. Results are compared to RadarSat imagery, the Remund-Long algorithm for SeaWinds, and passive microwave sea ice concentration data (reported using the NASA Team algorithm on SSM/I data).

Finally, Chapter 5 contains a summary of the research as well as possible lines of future research.

Chapter 2

Background

Microwave remote sensing has been adapted to the study of polar sea ice. An understanding of polar sea ice detection schemes requires an awareness of remote sensing principles, the operation of remote sensing instruments, and an understanding of previously developed algorithms. In this chapter, a brief background of microwave remote sensing of sea ice is given, both for active and passive sensors. The SeaWinds instrument is introduced, as well as methods for SeaWinds imagery enhancement. The chapter concludes with an overview of the NASA Team algorithm for estimating sea ice concentration from SSM/I data, as well as a verbose description of the Remund Long (RL) sea ice extent mapping algorithm for SeaWinds. These concepts provide a foundation for the research in subsequent chapters.

2.1 Microwave Remote Sensing of Sea Ice

The boundaries of the microwave region within the electromagnetic spectrum have no firm definitions. However, convention has it that microwaves exist in the 0.3 to 300 GHz range (1 m to 1 mm in wavelength). This region lies below the infrared and visible frequencies and overlaps on the low end with radio frequencies. The microwave spectrum provides a "sweet spot" for remote sensing applications—a good compromise between signal penetration and achievable image resolution. Lower frequencies enjoy greater penetration of the atmosphere, ground, canopy, etc., while higher frequencies allow for resolving smaller elements of a target scene.

Within the microwave region, there exist several bands in which microwaves are attenuated in the atmosphere. These bands correspond to the water vapor and

oxygen absorption bands. Water vapor absorption bands exist near 22 GHz and 180 GHz, and oxygen absorption bands exist near 56 GHz and 118 GHz [1]. For this reason, microwave sensors designed for detecting water or oxygen typically operate near the peaks of these absorption bands. In contrast, microwave sensors designed to detect surface phenomena typically operate in areas not effected by absorption bands. Often, instruments of this type are designed, in part, such that the wavelength of the transmitted signal is no smaller than the size of the surface detail of interest.

Although scatterometers and radiometers are both used in a myriad of remote sensing applications, the principles behind their operation is distinct. This thesis focuses on a particular scatterometer, the SeaWinds instruments, for mapping polar sea ice. However, radiometer and SAR data are used in this research for comparison and validation. Therefore, the basics of scatterometers, radiometers, and SARs are reviewed in this sections.

2.1.1 Active Microwave Remote Sensing

Microwave scatterometers are active remote sensing instruments that illuminate a target with microwave energy, and measure the reflected (backscattered) power. The received and transmitted power are related through the radar equation [1],

$$P_r = \frac{P_t G^2 \lambda^2 A}{(4\pi)^3 R^4} \sigma^o \ , \tag{2.1}$$

where P_r is the received power, P_t is the transmitted power, G is the scatterometer antenna gain, λ is the wavelength of the transmitted pulse, A is the area of the illuminated scene, R is the slant range to the target, and σ^o is the normalized radar cross section (NRCS) of the scene. The latter is a function of the surface characteristics, particularly the permittivity, surface geometry, and subsurface scattering mechanisms in a scene. However, σ^o is not solely a function of the surface characteristics. It is also related to the incidence angle θ, azimuth angle ϕ, frequency, and polarization of the transmitted signal.

The sensitivity of σ^o to the surface characteristics of polar sea ice is evidenced in several ways. First, the dependence on permittivity is important in surface and

volume scattering. Pure water has a relative permittivity of 80, where the average relative permittivity for sea ice is around 3.5 and very near 1 for snow (which is mostly air) [5]. Hence, brine-free melt ponds on the surface of the ice are highly reflective in comparison with ice or snow of similar roughness. Because they have small (and real) dielectric constants, ice and snow allow electric fields to form, propagate, and eventually scatter within the media. Thus, both surface scattering and volume scattering mechanisms are in operation.

The contribution of surface scattering to σ° is dependent on the surface geometry, as well. The interface between sea ice and the atmosphere may be smooth or rough, depending on the ice type. Many ice types, in fact, are aptly named to describe their surface geometry: smooth first-year ice, rough first-year ice, etc. The surface geometry of rough ice types contains features whose size is larger than the microwave wavelength. Multiple, randomly-oriented surface scattering mechanisms contribute to backscatter much of the incident microwave energy. Multi-year ice is typically much thicker than first-year ice types. Frequently, it is covered with a layer of snow which has accumulated through multiple seasons. Dry snow is nearly transparent to microwave frequencies, which allows the signal to interact with the ice beneath.

The volume scattering component of σ^o over ice is particularly significant for incidence angles greater than 20° [1]. When sea ice forms, small spaces between the ice crystals remain and are frequently filled with brine. Thus, sea ice is a non-homogeneous mixture of ice crystals, salt, brine channels, and air pockets. Brine channels form a three-dimensional network of tubes within the ice that have diameters of a few micrometers to several centimeters. This multi-layer structure—and the associated thicknesses and permittivities of the layers—create multiple scattering surfaces for the electric field within the sea ice.

The contribution of surface and volume scattering components to σ^o are dependent on sea ice type and seasonal surface dependencies. A study by Remund and Long [6] of microwave backscatter modeling of sea ice showed that volume scattering is much less important than surface scattering during the melt season. This agrees with intuition, since surface melting permits very little microwave energy to propagate

beneath the surface. During the winter months, volume scattering is very significant to the overall scatter.

In contrast, ocean water is often modeled as a lossy conductor at microwave frequencies. In this case, incident radiation is reflected, with very little penetration—surface scattering dominates. At off-nadir look angles, smooth ocean water scatters very little back to the scatterometer since the specular component of the reflected energy is large. However, a wind-agitated ocean surface is nearly Lambertian and the diffuse scattering component dominates, causing an increase in σ^o. The difference in how incoming radiation is reflected from sea water as opposed to sea ice is crucial in sea ice/open ocean discrimination.

2.1.2 Passive Microwave Remote Sensing

Microwave radiometry is also used extensively in remote sensing applications. As suggested by its name, radiometers measure naturally emitted radiation from objects in a scene. The term quantifying the emission by the observed scene is "brightness temperature," T_B, which may range from 0 K to a value equal to the physical temperature T_0. A T_B of 0 K suggests that the medium in the scene is non-emitting, while a T_B equal to T_0 represents perfect blackbody emission (a perfect emitter). Emissivity $e = T_b/T_0$ (which varies between zero and one) represents how much an object behaves like a perfect blackbody. Theoretically, a perfectly conducting material has zero emissivity. However, although conductors in a scene exhibit low T_B (low emissivity), the emissivity is not identically zero because the conductors reflect down-welling radiation from the atmosphere back to the sensor. In general, the scene temperature is not solely a function of natural emissions, but also scattering from up-welling (subsurface emission) and down-welling radiation.

As with σ^o, emissivity is not solely a function of the scene, but is related to a number of instrument parameters such as sensor frequency, polarization, incidence angle, azimuth angle, and beam-width. However, T_B is a strong function of physical properties of a scene. For example, emissivity is a function of water content, brine

concentration, and snow accumulation. The ability to extract these parameters make it possible to understand important geophysical processes involving sea ice.

Like scatterometers, the smallest element that can be resolved by a radiometer is governed by the antenna beam-width and the distance between the radiometer and the illuminated scene. Spaceborne radiometers typically have spatial resolutions, even at high microwave frequencies, of no finer than 15 km [1]. Nevertheless they are useful in extracting large-scale geophysical parameters such as sea surface temperature, wind speed, atmospheric composition, liquid-water content, rainfall rates, and sea-ice type and concentration.

2.1.3 Synthetic Aperture Radar

When high spatial resolution is required, synthetic aperture radar (SAR) imagery is used. A SAR is a coherent radar which relies heavily on signal processing to enhance the resolution intrinsic to the antenna. This is done by synthesizing a large aperture as the true antenna moves along its trajectory.

SAR systems are prone to geometric distortions, errors due to very small motion perturbations in the platform, and drift in electronic systems. These conditions, in addition to the nature of image reconstruction, creates ambiguity in the true values of the received power. In addition, daily SAR coverage is typically very poor in comparison with scatterometer or radiometer data. Therefore, SAR imagery is used in this thesis only for visual verification of sea ice extent in a small area. In particular, ice edge imagery is used from the SAR sensor on the Canadian Space Agency's RadarSat, a C-band (5.3 GHz), h-h polarized SAR capable of 10 m resolution. The RadarSat SAR has the ability to operate in 25 different imaging modes, but only images from the ScanSAR Wide mode are used in this thesis. In this mode, data are collected at incidence angles from 20°-50° over a 500 km x 500 km swath at 100 m resolution.

In this thesis, the extent of polar sea ice is viewed from scatterometer, radiometer, and SAR data. Each sensor type has advantages, and when used together, the true state of nature can more accurately be determined. An understanding of

the basic operation of these microwave instruments gives insight when interpreting the data or imagery they produce. Physical phenomena inferred from different sensor types may show discrepancies due to their differences in operation. However, reports from each sensor type are expected to show general correlation.

2.2 SeaWinds

The SeaWinds instrument on QuikSCAT was launched in 1999 as a "quick recovery" mission after a platform power failure prematurely terminated the NSCAT mission. Since that time, SeaWinds on QuikSCAT has provided an almost uninterrupted dataset of microwave observations of ocean, land, and sea ice. Another SeaWinds instrument, aboard ADEOS-II, was launched in late 2002 as an anticipated replacement for SeaWinds on QuikSCAT. (The SeaWinds instruments are identical. When distinction is required, it is customary to refer to SeaWinds on QuikSCAT as "QuikSCAT" or "QSCAT", while SeaWinds on ADEOS-II is referred to as "SeaWinds.") At the time of the preparation of this thesis, data from SeaWinds on ADEOS-II was not yet available. However, when imagery becomes available, we will enjoy a joint-SeaWinds dataset with observation times separated by only six hours in the polar regions.

The SeaWinds instrument is a 13.4 GHz (Ku-band) dual-polarized scanning pencil-beam scatterometer with two spot beam scans [7]. The outer beam, at 54° incidence, measures vertically polarized (v-pol) σ^o, denoted σ^o_{vv}, while the inner beam, at 46° incidence, measures horizontally polarized (h-pol) σ^o, denoted σ^o_{hh}. As the platform traverses, the outer beam forms an 1800-km swath, and the inner beam forms a 1400-km swath, each with no nadir gap. Consequently, SeaWinds covers nearly 90% of the earth's surface each day and 100% of the polar regions (excepting a gap directly over the poles due to its orbit geometry). A diagram of the SeaWinds scanning configuration is shown in Figure 2.1. This extent of spatial coverage is ideal for observing polar sea ice, where floes can move kilometers in a single day. Hence, polar SeaWinds imagery reconstructed from multiple swaths is not as subject to motion blur as NSCAT, which took 2-3 days for complete polar coverage [8].

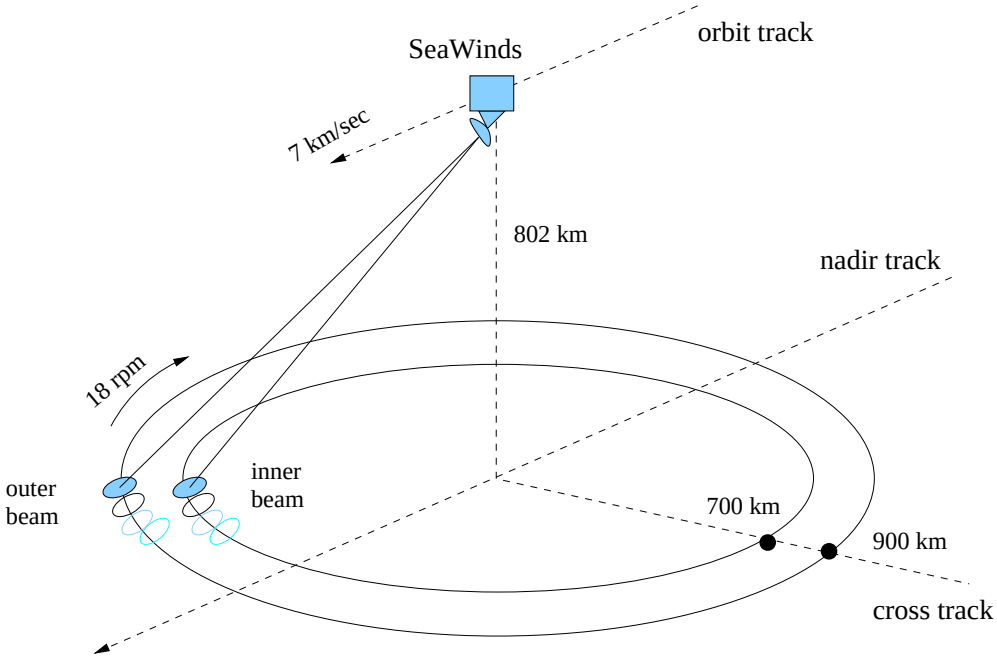

Figure 2.1: SeaWinds scanning configuration.

The SeaWinds instrument operates in two spatial resolution modes [9]. The intrinsic elliptical measurement cells, called "eggs" (or "spots") have nominal resolution of 25-km in azimuth by 37-km in the range direction. These cells are further resolved into "slices" through range and Doppler processing which results in multiple cells with sizes 2- to 10-km in the range direction by 25-km in azimuth. With increased resolution, however, comes an increase in the amount of noise in the data.

2.3 Resolution Enhancement

The intrinsic resolution of scatterometers is insufficient for certain applications of remote sensing data. To improve scatterometer resolution and to conveniently grid data, Long, *et al.*, [10] have developed the Scatterometer Image Reconstruction (SIR) algorithm. SIR is an iterative block multiplicative algebraic reconstruction technique (MART) that increases the intrinsic resolution of reconstructed imagery by using data from multiple satellite passes over the same region. This, in effect, trades temporal

resolution for spatial resolution. SIR utilizes the irregular sampling of multiple swaths to raise the side lobes of the antenna pattern, and thus increases the amount of detail in the reconstructed imagery.

SeaWinds imagery has been reconstructed using the SIR algorithm. For egg data, 4.45 km pixel resolution is achieved, with an effective resolution of 8–10 km. Due to the amplified noise in slice imagery, the SIR with filtering (SIRF) algorithm is used, in which a median filter is employed to decrease noise levels. SIRF reconstructed imagery compared with SAR imagery has demonstrated that the SIRF algorithm brings out additional surface features not present in non-enhanced imagery [11].

The SIR and SIRF algorithms produce several output images which give information such as σ^o, incidence angle information (not applicable for SeaWinds), number of hits per pixel, collection time, variance in σ^o, and many others. Of interest to us are the "A" images and the "V" images. "A" images are σ^o in dB. It is common notation to denote these image products as A_v and A_h for v- and h-pol, respectively. "V" images are the calculated standard deviation of σ^o in dB. As with "A" image products, individual polarizations are denoted as V_v and V_h for v- and h-pol, respectively. Figure 2.2 shows low resolution "A" browse imagery from data collected for a single day over the entire globe. In this figure, data gaps near the equator are visible. Also, sea ice is visually distinguishable from ocean in the images.

2.4 Ice Mapping Algorithms

Several previous algorithms have been developed for inferring polar sea ice concentration and extent [12]. Most notable for radiometer data are the NASA Team and "bootstrap" algorithms for the Defense Meteorological Satellite Program (DMSP) Special Sensor Microwave/Image (SSM/I) [12, 13, 14]. For scatterometer data, the Remund-Long (RL) algorithms for the NASA Scatterometer (NSCAT) and SeaWinds are widely used [2, 4, 15]. Since the emphasis in this thesis centers around the RL algorithm for SeaWinds, and ice concentration data derived from the NASA Team algorithm for SSM/I is used for validation of the new algorithm, these two algorithms are summarized in this section.

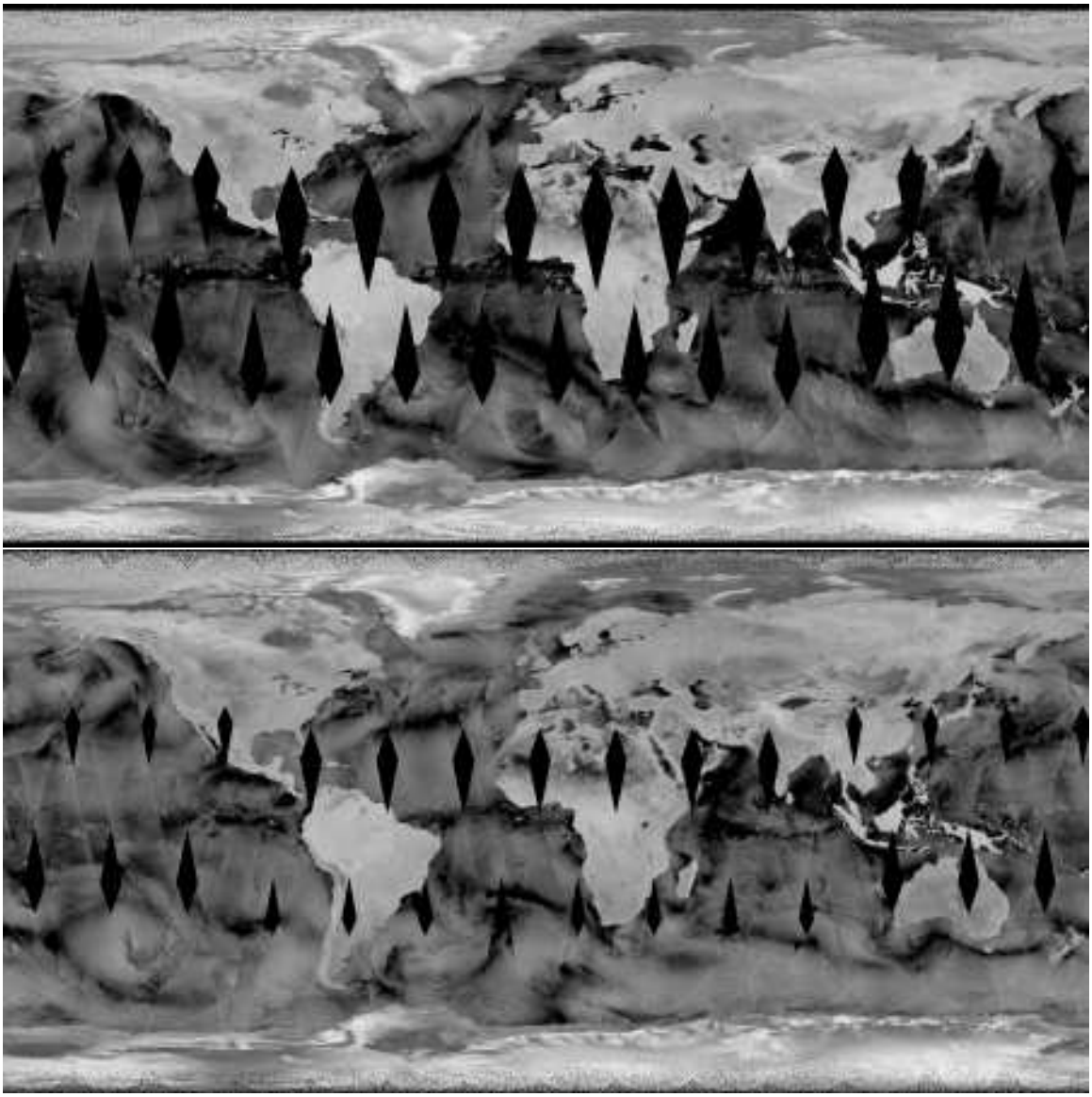

Figure 2.2: SeaWinds A_h (top) and A_v (bottom) imagery for Julian Day 110, 2001. Data gaps are located near the equator. Sea ice can be visually distinguished from open ocean.

2.4.1 NASA Team Algorithm

The NASA Team algorithm is a method for inferring sea ice concentration from passive microwave data, particularly the Scanning Multichannel Microwave Radiometer (SMMR), whose mission terminated in 1987, and the DMSP SSM/I mission, which is still in operation. The SSM/I instrument aboard the DMSP series of satellites is a total-power, seven channel, four frequency radiometer [16]. The channels receive h- and v-pol microwave radiation at 19.35, 37.0, and 85.5 GHz and v-pol only at 22.235 GHz. The elliptical footprint of each channel is rotated in a conical scan. Achievable resolutions are frequency dependent, but range from 13-43 km in the cross-track direction to 15-70 km in the along-track direction, with higher resolutions achieved by higher frequencies.

The NASA Team algorithm [12] is based on the assumption that the polar regions are composed of three primary surface types: open water, first-year sea ice, and multi-year sea ice. In effect, the polarization and spectral gradient ratios between the 19 GHz v-/h- and 37 GHz v- channels are used to compute the percentage contribution to total T_B from open ocean, first-year, and multi-year sea ice in a scene. The polarization ratio (denoted PR' to avoid ambiguity with the SeaWinds co-polarization ratio, PR, discussed later) and the spectral gradient ratio (GR) are defined by

$$\mathrm{PR}'\,[19] = \frac{T_B\,[19V] - T_B\,[19H]}{T_B\,[19V] + T_B\,[19H]} \tag{2.2}$$

$$\mathrm{GR}\,[37V/19V] = \frac{T_B\,[37V] - T_B\,[19H]}{T_B\,[37V] + T_B\,[19H]}. \tag{2.3}$$

These ratios are used to compute first-year and multi-year sea ice, C_{FY} and C_{MY}, respectively, using the relation

$$C_{FY} = \frac{a_0 + a_1\ \mathrm{PR}' + a_2\ \mathrm{GR} + a_3\ \mathrm{PR}'\ \mathrm{GR}}{D} \tag{2.4}$$

$$C_{MY} = \frac{b_0 + b_1\ \mathrm{PR}' + b_2\ \mathrm{GR} + b_3\ \mathrm{PR}'\ \mathrm{GR}}{D}, \tag{2.5}$$

where

$$D = c_0 + c_1\ \mathrm{PR}' + c_2\ \mathrm{GR} + c_3\ \mathrm{PR}'\ \mathrm{GR}. \tag{2.6}$$

The coefficients a_i, b_i, and c_i for $i = 0 \ldots 3$ are based on observed brightness temperatures (known as tie-points) over areas of known ice-free ocean, first-year ice, and multi-year ice. Total ice concentration is reported as $C_T = C_{FY} + C_{MY}$.

The NASA Team algorithm also incorporates a threshold on GR, setting C_T to 0% when GR exceeds the threshold. This reduces illegitimate ice concentrations caused by atmospheric distortion over open ocean.

Cavalieri [17] noted that errors in the sea ice concentration algorithm arise from four major sources. First, the algorithm assumes that there are only two ice types. This results in under- or over-estimates of sea ice concentration for other sea ice types such as new fast ice. Secondly, the algorithm shows inconsistency in sea ice concentration as the emissivity of sea ice varies with season. Third, the emissivity of sea ice shows non-seasonal variations (e.g., spatial dependence). Lastly, at sea ice concentrations greater than about 15%, weather impacts ice concentration estimates. In some cases, storms are reported as patches of ice. In addition, sea ice concentrations lower than 15% are truncated in an effort to reduce spurious reports of low concentration ice in the ocean.

SSM/I sea ice concentration grids are used in this thesis as a means for comparison. This is done noting the aforementioned sources of error. These products are gridded at a resolution of 25 x 25 km, compared to the 4.45 km x 4.45 km grid of SIR format SeaWinds egg imagery. Notwithstanding the coarse resolution and possible misclassifications in the ice concentration data, the products are widely used.

2.4.2 RL Algorithm for SeaWinds: Discrimination Parameters

The Remund-Long (RL) algorithm [4] is a multivariate ice extent mapping method for scatterometer data. It was first developed for the NASA Scatterometer (NSCAT). However, after the failure of NSCAT and the subsequent launch of QSCAT, the algorithm was modified for the SeaWinds instrument.

The RL algorithm for SeaWinds uses four parameters to discriminate between sea ice and open ocean. Each of these parameters is (or is derived from) a SIR image product, namely, PR $= A_v - A_h$ (in dB), A_h, V_v, and V_h. These parameters are

identical to those used in the ice extent mapping method of Chapter 4. Each of these parameters is defined in this section.

Co-Polarization Ratio

The first parameter used in the RL algorithm for SeaWinds is the co-polarization ratio, PR. In some texts, it is referred to as the copol ratio γ [3, 18] because of its incidence angle dependence. PR is defined to be ratio of the v- and h- pol responses, or in dB,

$$\mathrm{PR} = A_v - A_h. \tag{2.7}$$

An example of the utility of PR in sea ice discrimination in the Antarctic is shown in Figure 2.3.

PR couples two microwave signature dependencies. The most obvious is the polarization dependence on sea ice and ocean σ^o values. For ocean, v-pol σ^o values are typically higher than their h-pol counterparts. Sea ice, however, is not as lossy (conductive) as sea water. Microwave energy penetrates deeper into the subsurface. The multi-layer inhomogeneous mixtures of brine, salt, and air pockets act as volume scatterers. This volume scattering exhibits no polarization bias. As a result, v- and h-pol σ^o at the same incidence angles are similar. On the other hand, open ocean exhibits a significant polarization difference in σ^o.

The v- and h-pol components of PR are not at the same incidence angles, however. This brings us to the second dependency of PR—incidence angle. Incidence angle is sensitive to surface roughness [5]. Non-Lambertian surfaces exhibit high backscatter at near-nadir incidence angles, thus A_h at 46° incidence is greater than A_v at 54° incidence, neglecting polarization dependence. Microwave signatures over sea ice typically exhibit greater isotropy in incidence angle than open ocean.

Overall, the polarization and incidence angle dependence of σ^o contribute such that PR is low over sea ice and high over open ocean, with the distributions over each medium being approximately Gaussian. This parameter exhibits good statistical contrast between sea ice and ocean. However, wind-agitated ocean surfaces and

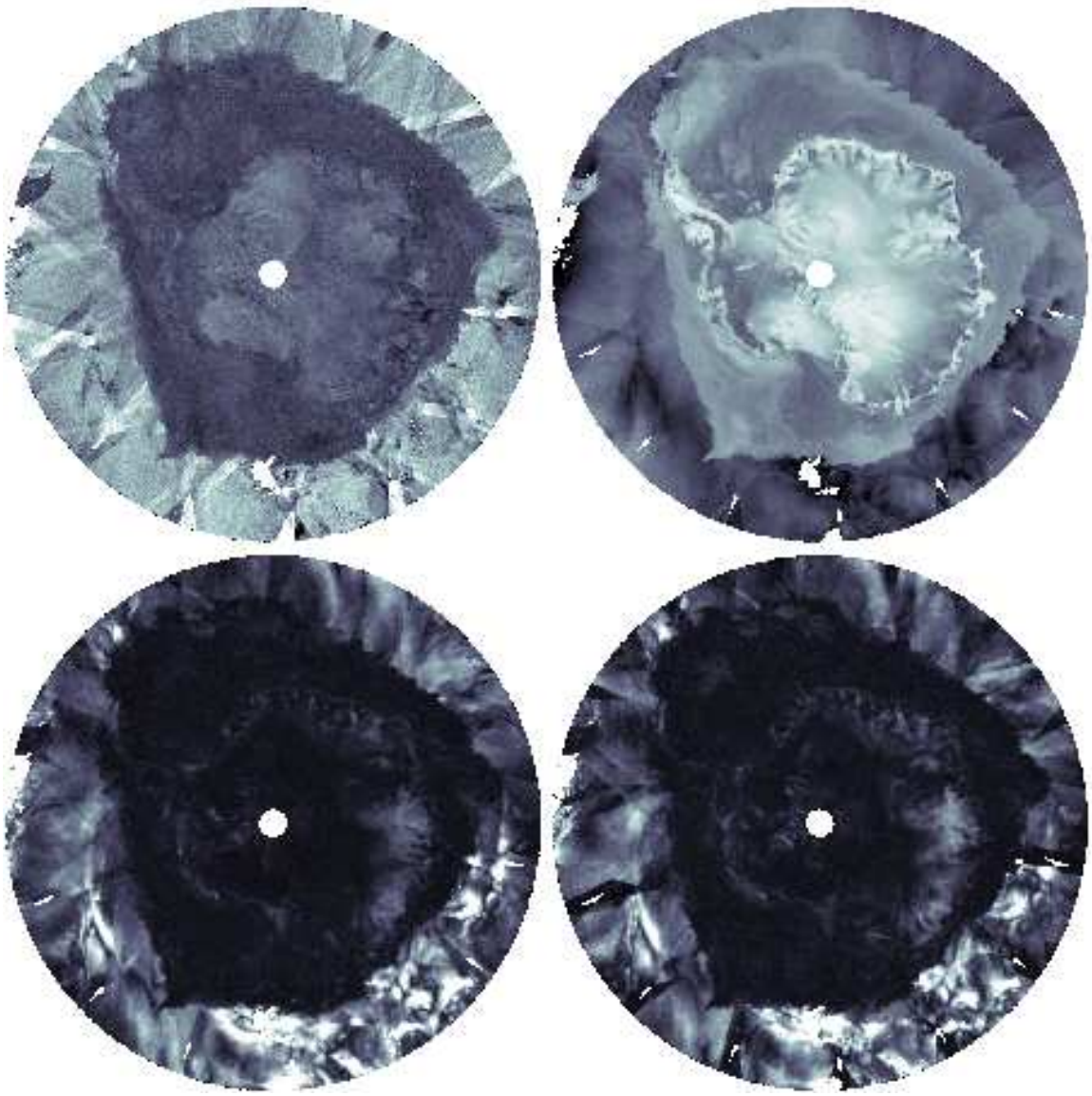

Figure 2.3: SeaWinds discrimination parameters: (left to right, top to bottom) PR, A_h, V_v, and V_h. Original images are each 1940 x 1940 pixels with 4.45 km pixel spacing. Bright V_v and V_h over East Antarctica is due to azimuth modulation from snow dunes.

melt events on sea ice reduce statistical contrast. Therefore, other parameters are introduced to decrease ambiguity.

Horizontal Polarization σ^o

A_h, h-pol σ^o at 46° incidence, is also a useful discriminant in ice/ocean segmentation. Because of the orientation of capillary waves, the ocean surface exhibits an h-pol bias. As discussed previously, volume scattering in sea ice effectively depolarizes microwave radiation. Thus, A_h exhibits greater statistical separation between ice and ocean than does A_v. Thus, to avoid linear redundancy with PR, A_h alone is selected as an additional discrimination parameter. A sample image is shown in Figure 2.3. In general, A_h is high over sea ice, and low over ocean.

As with PR, thresholds using A_h are prone to misclassification errors. Wind-induced capillary waves increase σ^o, greatly decreasing the statistical contrast between sea ice and ocean.

σ^o Standard Deviation Estimate

In addition to PR and A_h, V_v and V_h are used in the ensemble of discrimination parameters for sea ice classification. These images are produced during reconstruction using the SIR algorithm. They are statistically equivalent to the standard deviation of the difference error between the σ^o measurements touching a pixel and their associated forward projections [3]. They represent variations in observed σ^o during an imaging interval due to temporal variation and azimuth modulation. (SeaWinds collects measurements at a fixed incidence angle, so incidence angle is not a contributing factor.)

First, temporal variation in σ^o causes an increase in V_h and V_v. Surface properties change in the time it takes for the satellite to revisit a particular region. These changes are reflected in σ^o. As multiple swaths are combined during image reconstruction, the SIR algorithm reports this variance in V imagery. Temporal variations of this type are most likely to be observed on the ocean surface, which is constantly perturbed by ocean currents and storms. However, diurnal growth and retreat of the

ice edge or melt events during a collection interval is also evidenced in V_h and V_v, which create ice/ocean segmentation difficulties. (This topic is addressed in Appendix C.)

Another component of variation in σ^o is azimuthal variation. Because of the conical scan of the SeaWinds instrument, a single spot on the ground may be illuminated several times during the same swath, but from different azimuth angles. Azimuth modulation over wind-agitated ocean surfaces is fundamental in inverting the geophysical model function for wind speed and direction [19, 20]. In contrast, azimuth modulation over sea ice is negligible [21].

The ensemble of these four parameters—PR, A_h, V_v and V_h—provide for good statistical contrast between polar sea ice and ocean. Each conditional distribution over sea ice and ocean is approximately Gaussian distributed, with the exception of A_h in the Arctic, which is bimodal over sea ice due to high volume scattering contributions in multi-year ice.

2.4.3 RL Algorithm for SeaWinds

The RL algorithm for SeaWinds consists of three principal phases: (1) data fusion, (2) classification, and (3) binary processing. The first phase consists of generating enhanced imagery from the SIR algorithm (namely A_v, A_h, V_v and V_h), computing PR, and joining the data into a large observation matrix. The heart of the RL algorithm lies in the second phase, where a maximum likelihood classifier is used iteratively to estimate polar sea ice extent from the data. Lastly, binary processing is used to filter spurious classifications and constrain artificial ice growth/retreat. An in-depth description of the RL algorithm for SeaWinds can be found in [3]. In this section, the classification phase is discussed, as it is key to the performance of the algorithm.

The RL algorithm relies on a maximum likelihood (ML) classifier to separate observed data into ice and ocean classifications. The ML classifier is defined to be

$$C_{ML} = \arg\max_{C} P(\mathbf{z}|C) \tag{2.8}$$

where $\mathbf{z}$ is an observation vector, $\mathbf{z} = [4\,\mathrm{PR}\ \ A_h\ \ V_v\ \ V_h]^T$, and C is a classification. The weight of the PR component of $\mathbf{z}$ reflects the relative utility of the individual parameters in sea ice/ocean discrimination as demonstrated empirically. The weighting is applied after normalizing each parameter to be zero mean, unit variance. Although the general magnitude of the weights improves algorithm performance, the resulting sea ice extent maps are not particularly sensitive to the precise values [3]. For the RL algorithm, it is assumed that the multivariate conditional distributions, $P(\mathbf{z}|C)$, are close to Gaussian. This assumption allows for simplification as follows,

$$\begin{aligned} C_{ML} &= \arg\max_C \left\{ \frac{1}{(2\pi)^{n/2}|K_C|^{1/2}} e^{-\frac{1}{2}(\mathbf{z}-\mathbf{m}_C)^T K_C^{-1}(\mathbf{z}-\mathbf{m}_C)} \right\} \\ &= \arg\min_C \left\{ \log|K_C| + (\mathbf{z}-\mathbf{m}_C)^T K_C^{-1}(\mathbf{z}-\mathbf{m}_C) \right\}, \end{aligned} \tag{2.9}$$

where $\mathbf{m}_C$ and K_C are the mean vector and covariance matrix for the multivariate distribution ($n = 4$) of $\mathbf{z}$ given C, respectively. Convention for the RL algorithm assigns $C = 0$ for ocean and $C = 1$ for sea ice. It is intuitively appealing to note that the $(\mathbf{z}-\mathbf{m}_C)^T K_C^{-1}(\mathbf{z}-\mathbf{m}_C)$ term is equal to the square of the Mahalanobis distance from the observation vector $\mathbf{z}$ to the centroid $\mathbf{m}_c$. This is akin to a Mahalanobis nearest neighbor (NN) approach.

Since K_C and $\mathbf{m}_C$ are initially unknown, the first step in the classification process is to estimate these parameters for $C = 0$ and $C = 1$. This is done by generating a 4-D histogram, locating the modes, and performing linear discrimination. A 2-D representation of a typical multivariate histogram is shown in Figure 2.4. Linear discrimination is performed by assigning each observation pixel $\mathbf{z}$ to the class C that minimizes the Euclidean norm $||\mathbf{z} - \hat{\mathbf{m}}_C||_2$, where $\hat{\mathbf{m}}_C$ represents the mode of population C. This initial classification allows for computing ML estimates for K_C and $\mathbf{m}_C$, since each observation pixel now belongs to a class.

The ML classifier in Equation (2.9) is used iteratively since the initial estimates of $\mathbf{m}_C$ and K_C are crude. Assuming that the data fits the Gaussian model, convergence is reached after three to five iterations. A 2-D representation of sea ice and ocean population modes, the means located via linear discrimination, and the

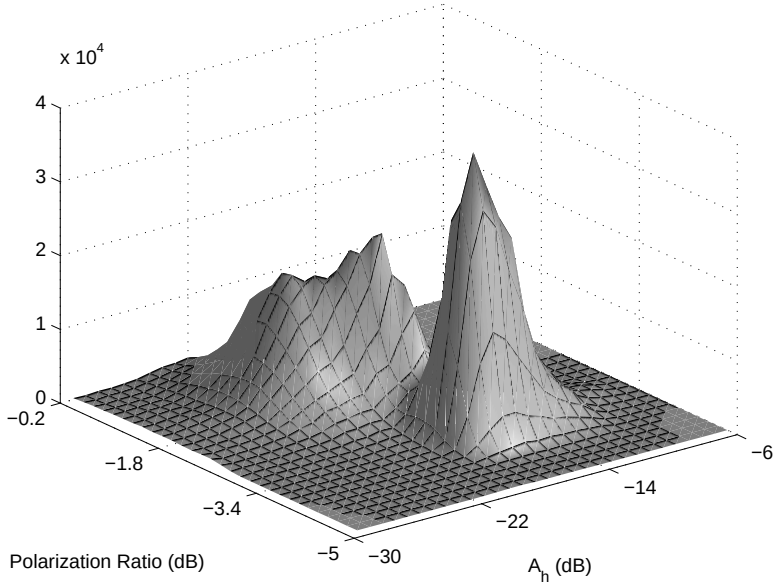

Figure 2.4: Two-dimensional representation of multivariate histogram of SeaWinds discrimination parameters. The sharp peak corresponds to the ice population (low PR, high A_h), while the broader mode correspond to the ocean population (high PR, low A_h).

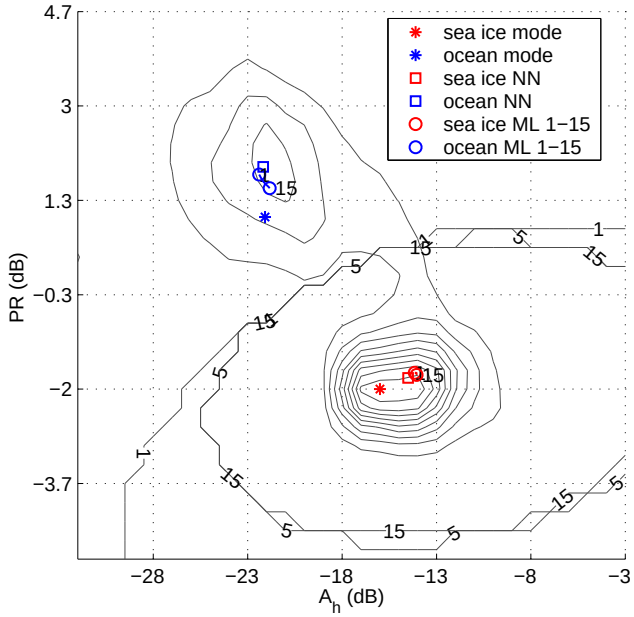

Figure 2.5: A sample 2-D (PR versus A_h) representation of the 4-D histogram generated by the RL algorithm. The population modes, the means calculated via NN discrimination, and the means calculated via ML classification (for 15 iterations) are labeled. The discrimination boundary between sea ice and ocean is also shown for the first, fifth, and fifteenth iterations.

means located via the ML classifier are shown for fifteen ML iterations in Figure 2.5. A sample classification image for the Arctic region is shown in Figure 2.6.

Obvious misclassifications in Figure 2.6 show the need for binary processing/filtering techniques. The RL algorithm filters residual noise through a series of dilation/erosion operations, and region growing techniques. These techniques are external to the theory of the algorithm, and are not discussed here. However, it should be noted that this filtering process smooths the ice edge and fills in polinyas, resulting in cleaner but more coarse estimate of sea ice extent. Binary process techniques are reviewed in Appendix B.

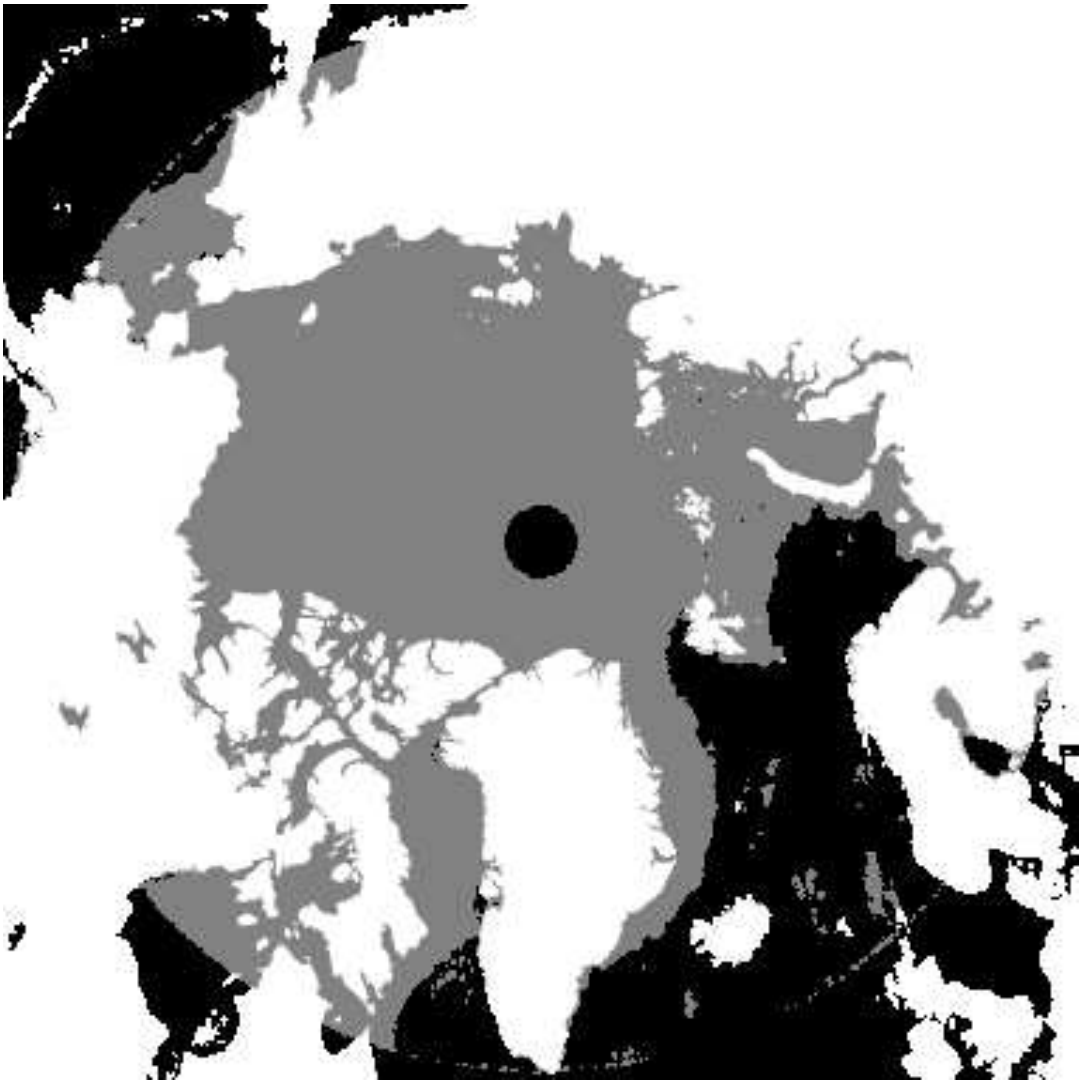

Figure 2.6: Pre-filtered classification from RL algorithm for Arctic region (JD 034, 2002). White represents land, gray represents sea ice, and black represents ocean and no-data points. There are obvious misclassifications.

Chapter 3

Analysis and Improvements of the Remund Long Algorithm

The Remund Long (RL) algorithm for SeaWinds [3] provides high-resolution estimates of polar sea ice extent. Ice extent imagery during normal weather conditions of the polar winter is consistent in accurately representing the ice edge. During the winter, the ice edge is well defined: diurnal temperature variations are small, and the ice types are homogeneous. This provides the scatterometer with consistent measurements at each satellite pass. The RL algorithm performs well when the sea ice and ocean populations are high and the variances of the classification parameters are low.

During the polar summers, however, the ice imagery is not as consistent. This can be ascribed to wide variations in daily temperature that cause surface melt, weather-agitated ocean regions, and the heterogeneity of sea ice type in space and/or time. Melt events dramatically increase the contribution of surface scattering and decrease the volume scattering contribution to σ^o. Sea ice appears much darker in A_h and A_v imagery, and can be confused with calm ocean. In addition, multiple freeze/thaw events within an imaging interval cause V_v and V_h estimates to rise. This also causes sea ice to appear more like ocean. Rapid growth and retreat of sea ice during an imaging interval also create ambiguity in discrimination using V_v and V_h imagery.

Open ocean exhibits microwave signatures similar to sea ice under certain conditions. High near-surface wind speed causes an increase in σ^o, and persistence in wind speed over an imaging interval causes a decrease in V_h and V_v. These conditions cause ocean signatures to be very similar to sea ice signatures. Wind induced

perturbations of sea ice and ocean statistics are particularly an issue in the Antarctic region, where some of the most intense and persistent winds are present, in the form of ocean storms and katabatic winds [22].

Despite the ill-conditioned problem of sea ice discrimination in the polar summer, the RL algorithm performs quite well. Its dynamic nature allows fluctuations in sea ice and ocean statistics without severely degrading performance. Binary processing and ice edge growth/retreat constraints are included in the RL algorithm to ameliorate many of the classification errors induced by anomalous conditions. Because of the robustness of the RL algorithm, it is being used with near real-time data at NASA's Jet Propulsion Laboratory (JPL) for wind retrieval and at the National Oceanic and Atmospheric Administration (NOAA) for polar sea ice studies.

This chapter investigates the convergence of the RL maximum likelihood classifier over a one year span. Time spans where the algorithm converges and diverges are identified. The factors contributing to the divergence of the algorithm are also investigated. Finally, a modification to the RL algorithm is suggested in cases where sea ice and ocean observations do not fit the Gaussian statistical model. In addition, an adjustment is made to the binary processing phase of the algorithm, which improves sea ice growth/retreat constraint.

3.1 Assumptions of the RL Algorithm

The RL algorithm incorporates a maximum likelihood (ML) classifier to separate observed data into sea ice and ocean classes. From Equation (2.9), the ML classifier with a Gaussian model is

$$C_{ML} = \arg\min_{C} \left\{ \log |K_C| + (\mathbf{z} - \mathbf{m}_C)^T K_C^{-1} (\mathbf{z} - \mathbf{m}_C) \right\}, \tag{3.1}$$

where $\mathbf{z}$ is an observation vector, C is a class (sea ice or ocean), $\mathbf{m}_C$ is the centroid for the given class, and K_C is the covariance. The RL algorithm uses ML estimates of the latter two parameters when evaluating Equation (2.9).

The ML classifier is robust and simple. However, errors result if the data population sizes are insufficient, if the ice or ocean populations are not Gaussian

distributed, or if the classifications have poor statistical separability. In the RL algorithm, the ML classifier is used iteratively, so that an early failure of the ML classification can lead to divergence of the algorithm.

3.2 Analysis of RL Algorithm

This section presents an analysis of the convergence characteristics and statistical modeling error of the RL algorithm as a function of season. For this study, the Arctic and Antarctic regions are tested individually. Although the RL algorithm is identical for both the Arctic and Antarctic regions, the Arctic sea ice distribution is typically bimodal—a contribution from the presence of both first-year and multi-year sea ice. The bimodal nature of Arctic sea ice causes different behavior in the RL algorithm than for Antarctic sea ice. Divergence patterns in the Antarctic and Arctic regions motivate an improved algorithm, as described in Chapter 4.

First, the seasonal dependence of algorithm convergence is investigated. It is found that the algorithm exhibits convergence characteristics that are seasonally dependent. Secondly, the apparent departure from Gaussian of the discrimination parameters is investigated.

3.2.1 Seasonal Convergence

For each day of the year 2000, the RL algorithm is applied using fifteen iterations. For each iteration, the class centroids are (1) identified over the year span, (2) compared with the identified modes, and (3) compared with the previous iteration's mean.

Figure 3.1 shows the mode, the mean resulting from nearest-neighbor (NN) classification, and the means resulting from the ML classifications of fifteen iterations of the normalized (zero mean, unit variance over the ensemble of sea ice and ocean populations) PR of the Antarctic sea ice distribution for the year 2000. Note that the large variance in Figure 3.1 is a result of the weighting vector [4 1 1 1] applied to the parameter vector $[\mathrm{PR}\ \ A_h\ \ V_v\ \ V_h]$ in the data fusion step of the RL algorithm.

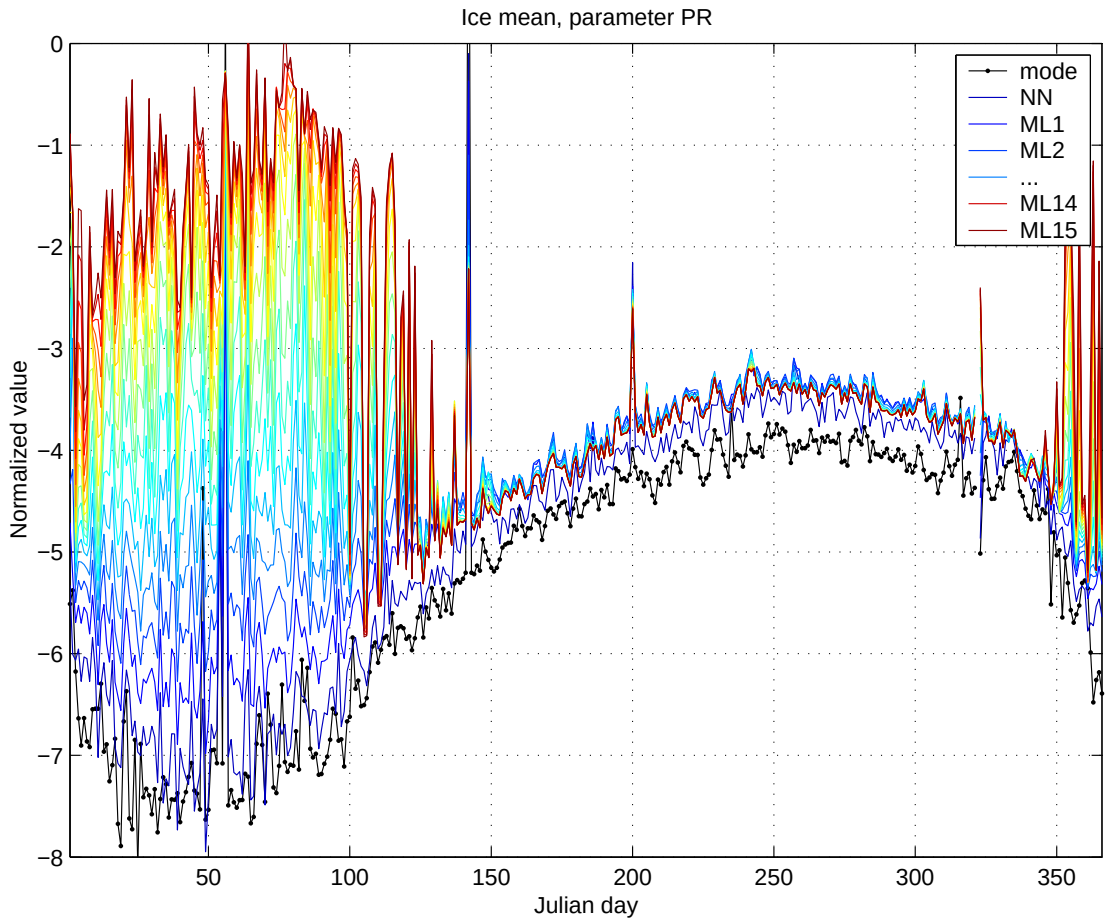

Figure 3.1: Normalized PR of the Antarctic sea ice population versus Julian day (year 2000) of the identified mode, the mean resulting from NN classification, the mean resulting from the ML classification of the first iteration (ML1), the second iteration (ML2), and so on, up to the fifteenth ML iteration (ML15). Note that some spurious spikes in the data (at JD 001-002, JD 141-142, JD 199-200, JD 321-323) are a result of instrument failure/shutdown.

Thus, PR is distributed with zero mean, variance $\sigma^2_{PR} = 16$, as opposed to the other parameters, which are distributed with zero mean, unit variance.

Figure 3.1 reveals that in the austral summer, successive iterations cause the mean to depart from the mode of the PR distribution for Antarctic polar sea ice. The differences between the estimated means of each iteration and the distribution modes are shown in Figure 3.2. In this figure, it is evident that by the fifteenth iteration, there is significant departure of the estimated mean from the distribution mode during the austral summer, whereas the austral winter shows little difference.

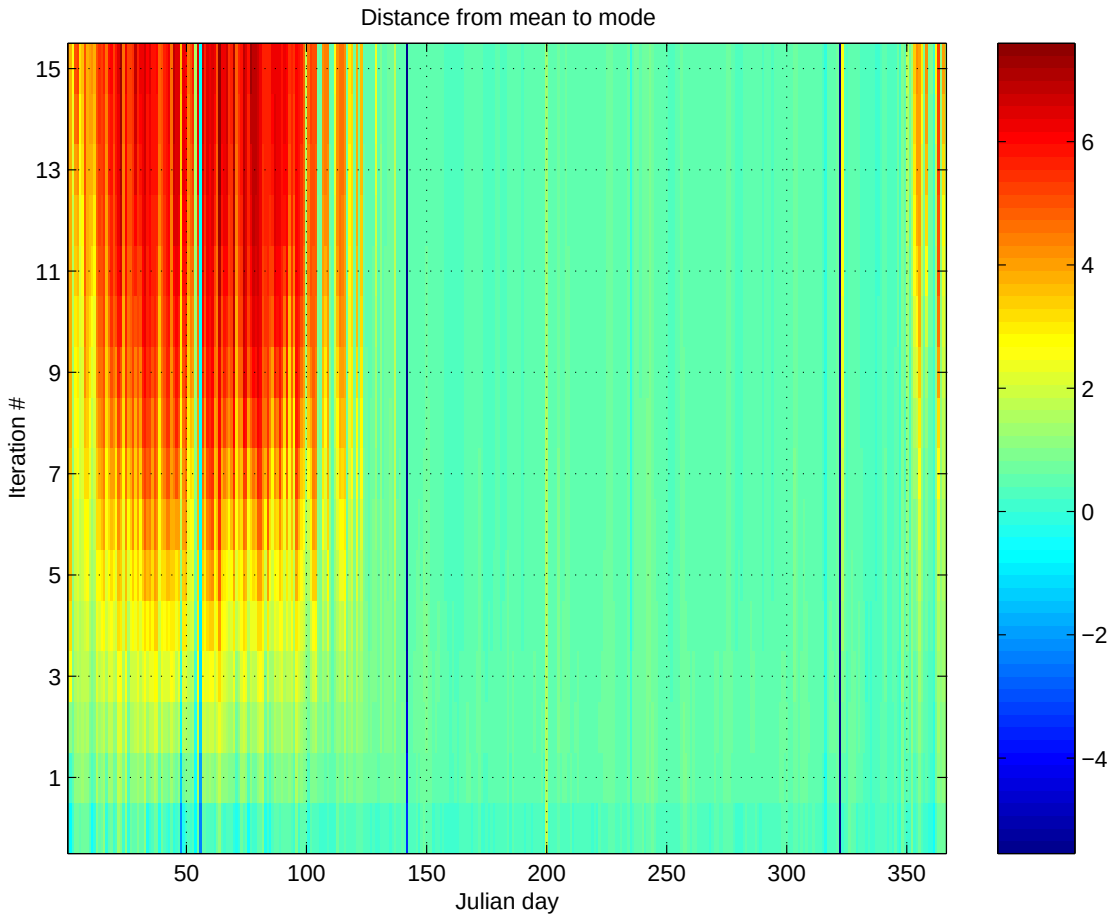

Figure 3.2: Difference between the means of each iteration and the mode of the normalized PR distribution of Antarctic sea ice for the year 2000. The mean resulting from NN classification is labeled as the 0th iteration. Note that a few of the discontinuities are a result of instrument failure/shutdown (see caption of Figure 3.1).

Figure 3.3 shows the relative change of the estimated means from one iteration to the next. Since convergence may be assumed when further iterations yield little or no change in the class centroid, this plot shows evidence that the PR component (in [PR A_h V_v V_h]) converges quickly in the austral winter, but slowly in the austral summer.

Note that the convergence properties of PR shown in Figures 3.1, 3.2, and 3.3 are coupled with the convergence properties of A_h, V_v and V_h for sea ice, as well as the whole ensemble of discrimination parameters for ocean. The dependence of the sea ice centroid on the ocean centroid is a result of the iterative nature of the algorithm, wherein a misclassification causes a bias in the centroid estimate, which subsequently

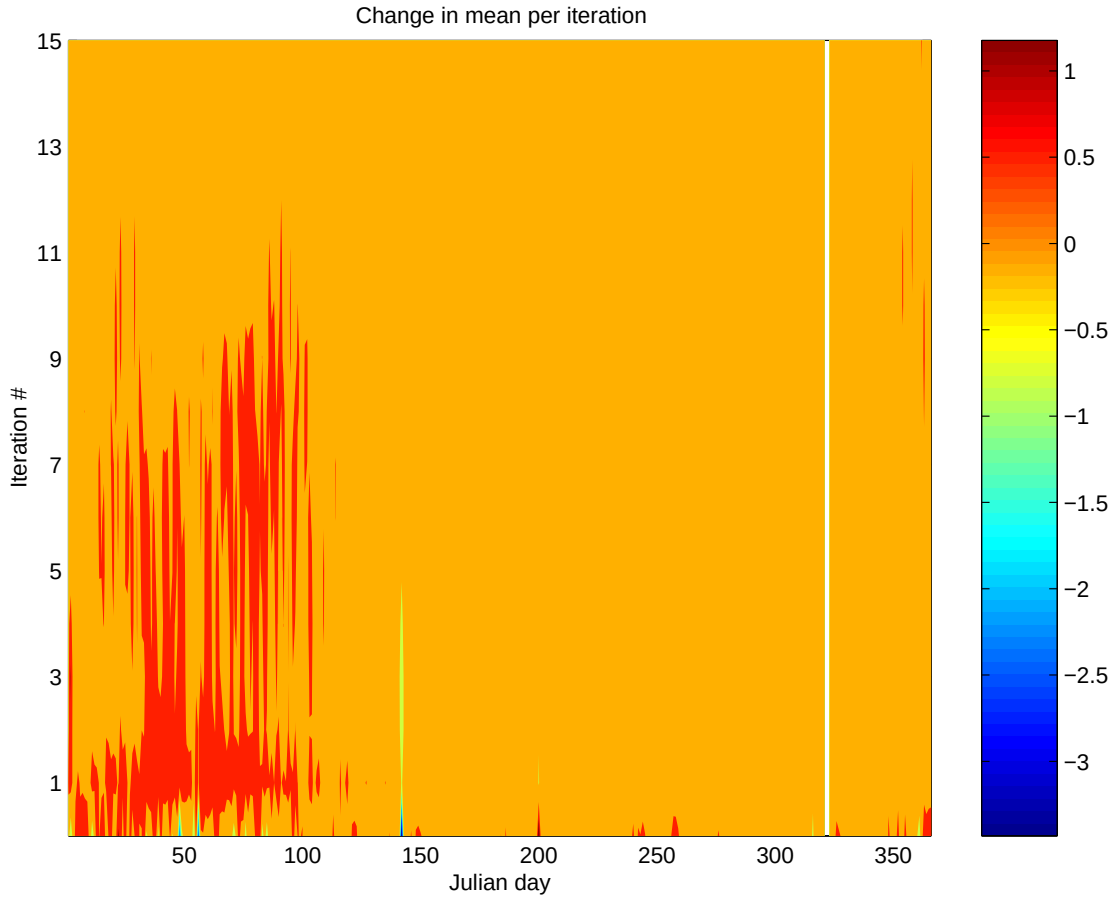

Figure 3.3: Change in mean per iteration of the normalized PR distribution of Antarctic sea ice for the year 2000. The zeroth row corresponds to the difference between the NN mean (see Figure 3.1) and the distribution mode, the first row corresponds to the difference between NN and ML1, and so on. The PR component of [PR A_h V_v V_h] converges slowly in the austral summer, but quickly in the austral winter.

causes a greater centroid drift, and so on. In the Antarctic scenario, this avalanching effect shifts the threshold (a hyper-curve) closer to the ocean centroid, causing a bias in both the sea ice and ocean centroids. The avalanching effect begins because actual sea ice or ocean statistics deviate substantially from Gaussian.

Convergence properties for the ensemble of discrimination parameters are shown in Figure 3.4 for Antarctic sea ice, Figure 3.5, for Antarctic ocean, Figure 3.6 for Arctic sea ice, and Figure 3.7 for Arctic ocean. The convergence properties for the Antarctic and Arctic regions are discussed individually in the following subsections.

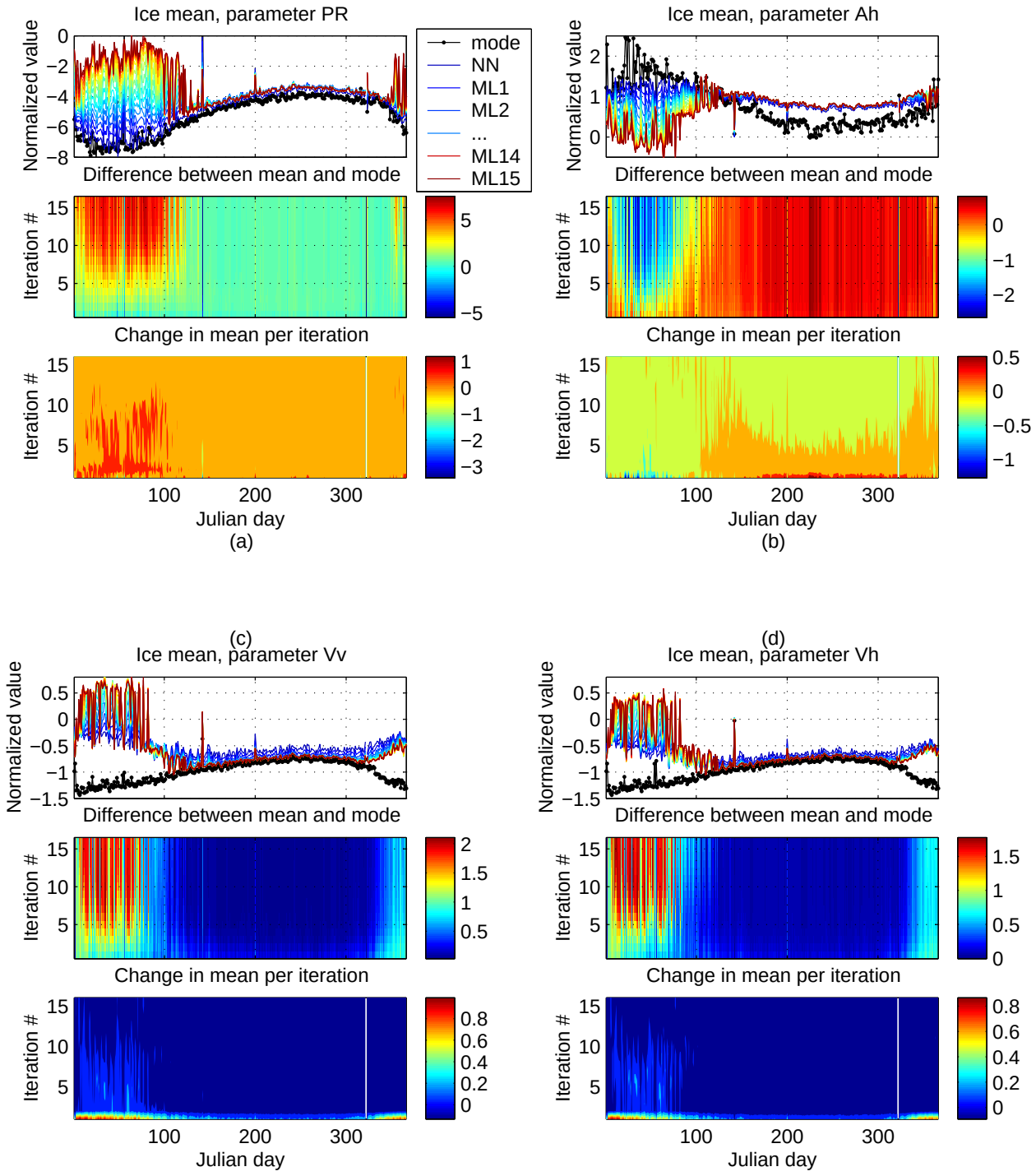

Figure 3.4: Convergence properties of the Antarctic sea ice centroid, [PR A_h V_v V_h], for each component: (a) PR, (b) A_h, (c) V_v, and (d) V_h. The panels (from top to bottom) of each sub-figure are similar to Figures 3.1–3.3, but for each RL parameter.

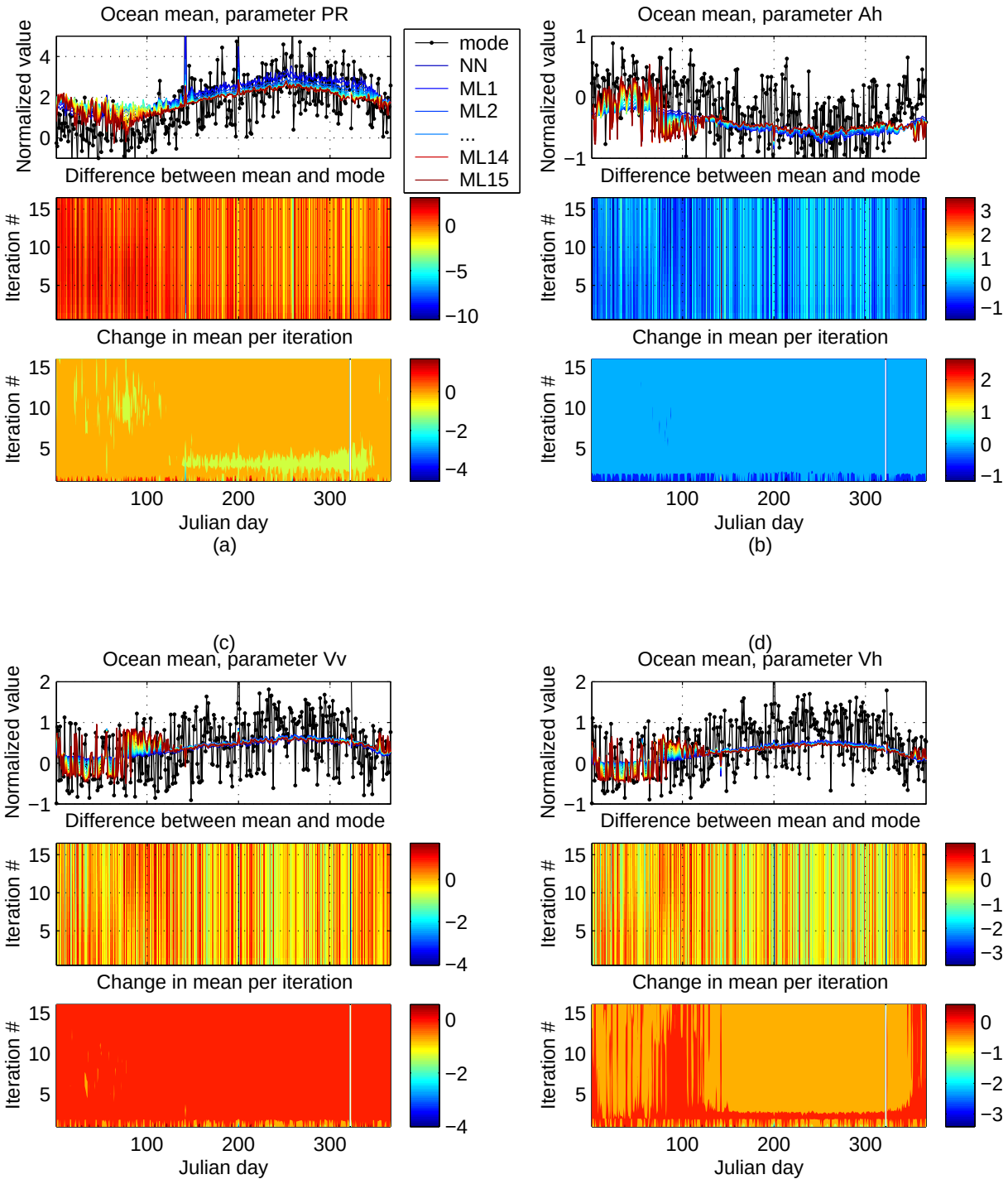

Figure 3.5: Convergence properties of the Antarctic ocean centroid, [PR A_h V_v V_h], for each component: (a) PR, (b) A_h, (c) V_v, and (d) V_h. The panels (from top to bottom) of each sub-figure are similar to Figures 3.1–3.3, but for each RL parameter.

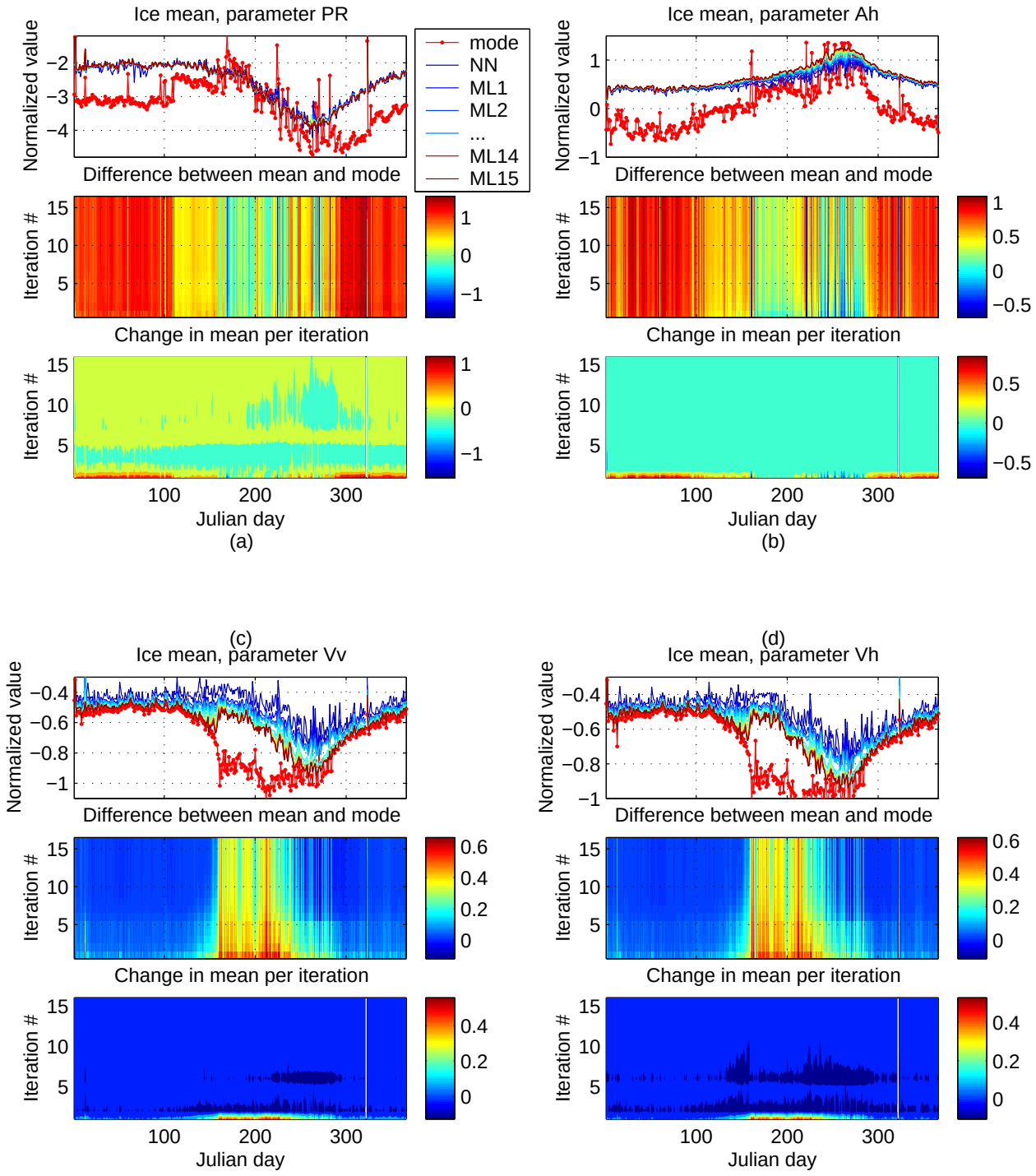

Figure 3.6: Convergence properties of the Arctic sea ice centroid, [PR A_h V_v V_h], for each component: (a) PR, (b) A_h, (c) V_v, and (d) V_h. The panels (from top to bottom) of each sub-figure are similar to Figures 3.1–3.3, but for each RL parameter.

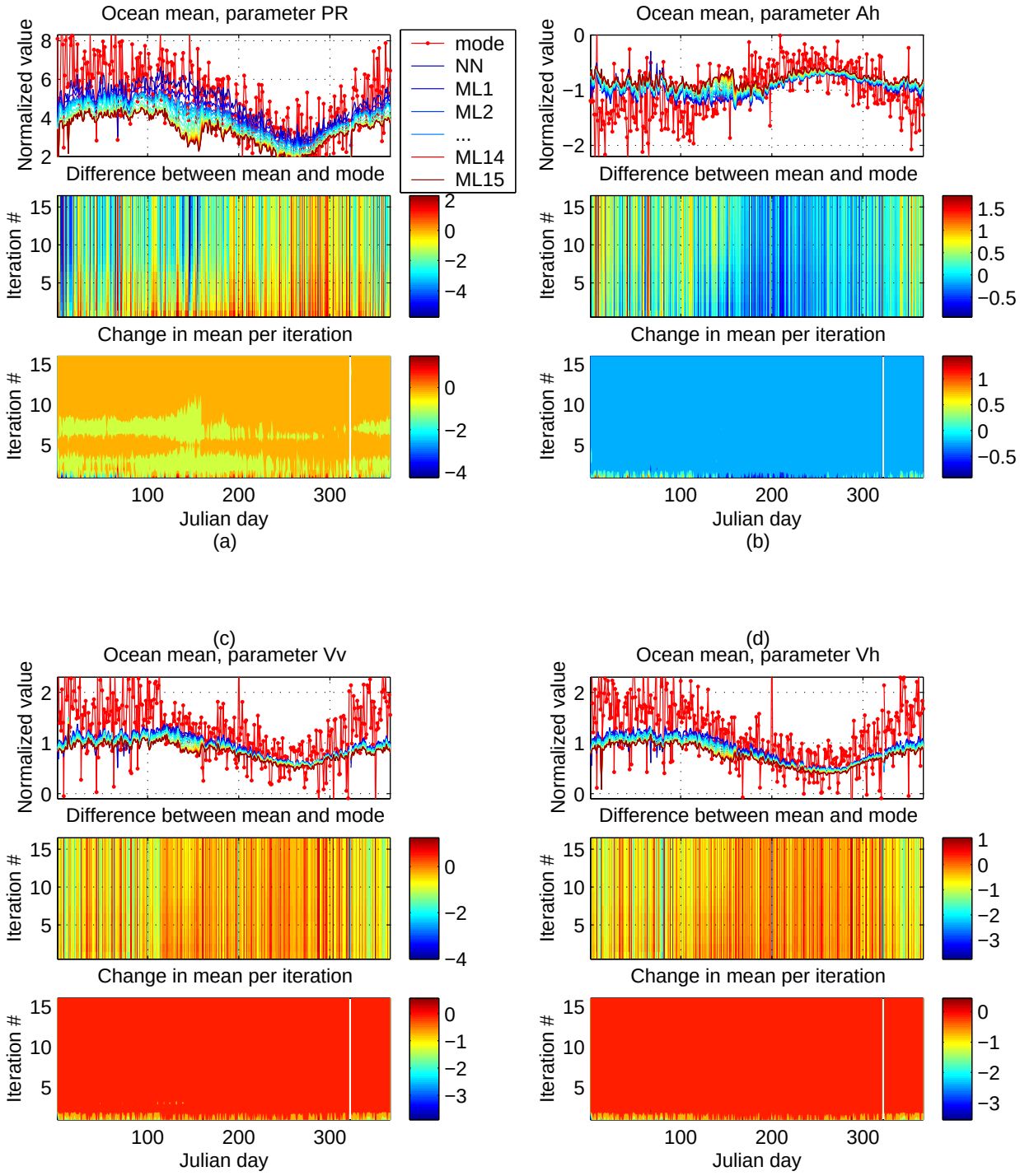

Figure 3.7: Convergence properties of the Arctic ocean centroid, [PR A_h V_v V_h], for each component: (a) PR, (b) A_h, (c) V_v, and (d) V_h. The panels (from top to bottom) of each sub-figure are similar to Figures 3.1–3.3, but for each RL parameter.

3.2.2 RL Convergence Properties in the Antarctic

Figures 3.4 and 3.5 present heuristic evidence about the convergence trends of the RL algorithm for the Antarctic region. First, in comparing sea ice versus ocean convergence, it appears that although the ocean population modes show diurnal variations, the algorithm exhibits more consistent convergence throughout the year. This suggests that the statistical modeling error for ocean populations is generally less significant than the modeling error for sea ice populations during the austral summer.

In addition, a peculiar change in the convergence trend for sea ice is apparent. Divergence is observed from Julian Day (JD) 1 through about JD 100, and again starting from JD 330, although these temporal boundaries are not crisp. These events correspond to changes of season. Melt events are frequent at the beginning and end of the year (austral summer). These alter the microwave signatures and decrease the population size of sea ice. In particular, melt events cause an increase in the variance of sea ice microwave signatures. A further analysis reveals that the algorithm generally diverges when $\det|K_{ice}| > \det|K_{ocean}|$ for initial (NN) estimates of K_{ice} and K_{ocean}.

Further, it is observed that the algorithm generally converges when V_v and V_h initial estimates (NN) for the mean are approximately equal to their respective modes. Nontrivial statistical modeling error is expected when the difference between the mode and mean of a distribution is significant. Note that even for truly Gaussian distributions, thresholding truncates the distribution tails, causing a slight difference in the mean and the mode. The significant difference between the mean and mode evidenced in V_v and V_h in Figure 3.4 suggest that these parameters have skewed distributions (a non-Gaussian cumulant).

To validate the conjecture that sea ice statistics depart from Gaussian, a third- and fourth-order cumulant test is performed on the marginal distributions of Antarctic sea ice (PR, A_h, V_v and V_h). For a truly Gaussian distribution, central moments of order greater than two are identically zero. This test provides a simple means to quantify the departure of the marginal distributions from Gaussian. Although Gaussian marginals do not ensure that the joint 4-D distribution is Gaussian, a truly

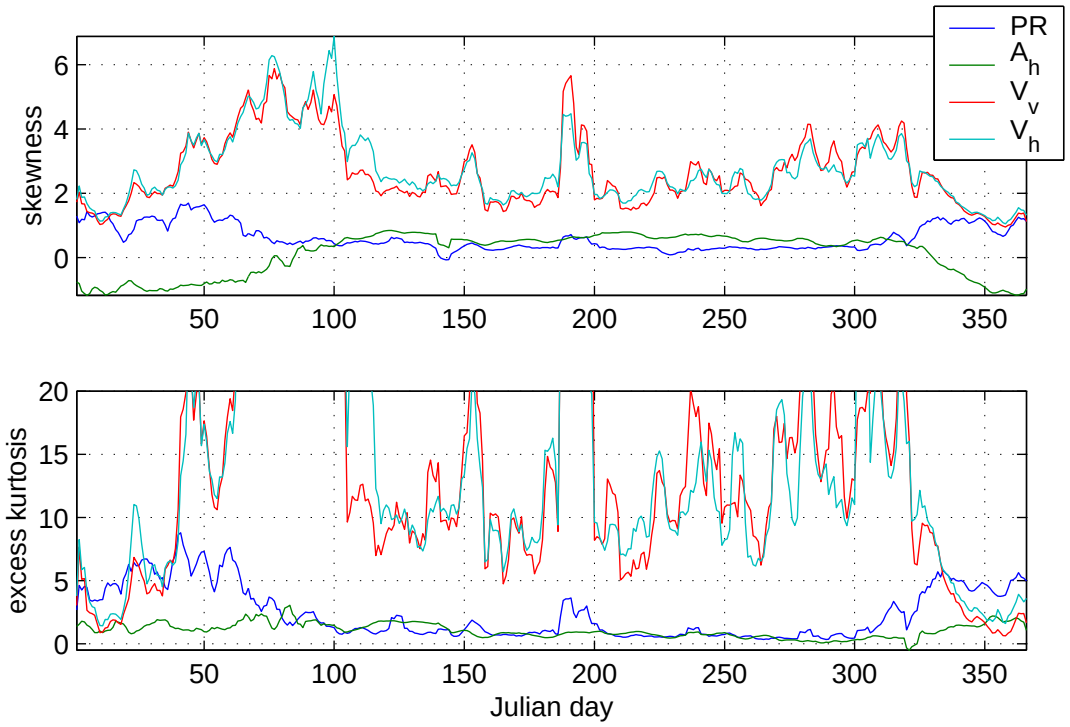

Figure 3.8: Skewness (top) and excess kurtosis (bottom) of the marginal distributions of the RL discrimination parameters (PR, A_h, V_v, and V_h) for Antarctic sea ice for the year 2000. Truly Gaussian distributions have zero skewness and zero excess kurtosis. The excess kurtosis plot is only shown from 0 to 20 for the sake of comparison, but V_v and V_h exhibit kurtosis measurements as high as 50.

Gaussian joint distribution must have Gaussian marginals. The skewness and excess kurtosis is measured for each RL parameter for each day of 2000. The skewness and excess kurtosis of a random variable X are estimated using samples of X, $X_1 \ldots X_N$,

$$\text{skewness} \approx \frac{\sum_{i=1}^{N}(X_i - \bar{X})^3}{(N-1)\sigma^3} \tag{3.2}$$

$$\text{excess kurtosis} \approx \frac{\sum_{i=1}^{N}(X_i - \bar{X})^4}{(N-1)\sigma^4} - 3, \tag{3.3}$$

where $\bar{X}$ is the mean, and σ is the standard deviation of X. (Note that excess kurtosis is used since a Gaussian distribution has kurtosis equal to three.)

Figure 3.8 shows that the ensemble of parameters is "most Gaussian" from JD 120 to JD 320. Note that each parameter is leptokurtic (positive kurtosis), meaning that the distributions have sharper peaks than a Gaussian distribution. Also note that the skew for the parameters is slightly biased due to thresholding. In general, PR and A_h are well-behaved throughout much of the year, while V_v and V_h deviate

significantly from Gaussian. The departure from Gaussian degrades the performance of the ML classifier in Equation (2.9).

3.2.3 RL Convergence Properties in the Arctic

Figures 3.6 and 3.7 show the seasonal convergence trends of the RL algorithm for the Arctic region. In contrast to trends for the Antarctic region, class centroids for the Arctic do not drift significantly in fifteen iterations. This is true for both sea ice and ocean, regardless of the season.

However, Figures 3.6 and 3.7 do suggest that the Gaussian model for Arctic sea ice is inaccurate. First, in the boreal winter, PR and A_h parameter distributions have means that are not consistent with their respective modes. In the boreal summer, however, the means and modes are in agreement. This phenomenon can be attributed to large multi-year and first-year sea ice populations in the boreal winter, resulting in a bimodal distribution, where the first-year sea ice mode is more dominant than the multi-year sea ice mode. (The PR component in Figure 3.6 shows evidence that the dominant sea ice mode switches from first-year ice to multi-year ice at JD 110, before statistics are drastically affected by melting at JD 150.) In the boreal summer, only the multi-year sea ice mode remains.

Conversely, the sea ice distributions for V_v and V_h show consistency between their means and respective modes during the boreal winter. In the boreal summer, due to melt events and sea ice motion during the imaging interval, V_v and V_h distributions deviate from Gaussian, as evidenced by the departure of the means from their respective modes. In the Arctic, PR and A_h show non-Gaussian characteristics during the boreal winter, and V_v and V_h show non-Gaussian characteristics during the boreal summer.

3.2.4 Analysis Summary

In summary, an analysis has shown evidence that the discrimination parameters for sea ice are not jointly Gaussian during the austral summer. This modeling

error is significant enough to cause divergence in the Antarctic region during the austral summer. In most cases, the sea ice centroid drifts into the ocean population, as illustrated in Figure 3.9.

For the Arctic, the RL algorithm does not diverge at any time during the year 2000. However, Gaussian modeling error for Arctic sea ice is evidenced in the departure of distribution means from their respective modes. This is true of PR and A_h during the boreal winter, and V_v and V_h in the boreal summer. An analysis on the performance of the RL algorithm for science (SIR) "slice" data and near real-time (NRT) data exhibit similar, but more pronounced divergence characteristics for the Antarctic region.

3.3 Algorithm Modifications

Two modifications are made to the RL algorithm to improve its performance. First, in light of the discussion in Section 3.2, the RL algorithm is modified to avoid divergence. The algorithm is allowed five iterations during the entire year for the Arctic region and during the austral winter, but is restricted to a single iteration during the austral summer. The number of iterations during the transition between austral summer and winter is ramped from one to five, and from five to one at the onset of the melt season.

Although this modification does not solve the problem of non-Gaussian statistics, it does prevent the RL algorithm from diverging. Classification imagery (prior to binary processing) produced by the modified algorithm contains fewer misclassifications than the original algorithm. However, binary processing methods are still required to filter residual noise, and to constrain sea ice growth/retreat.

In the binary processing phase of the RL algorithm, residual noise is filtered with a sequence of erosion and dilation procedures. This, in effect, produces a low-pass filtered estimate of the classification image. In addition, an ice extent map from a previous day is used to constrain sea ice growth and retreat. The ice edge is not allowed to grow or shrink more than a predetermined distance from the previous day's edge. Sections classified as sea ice which violate the growth constraint are cut

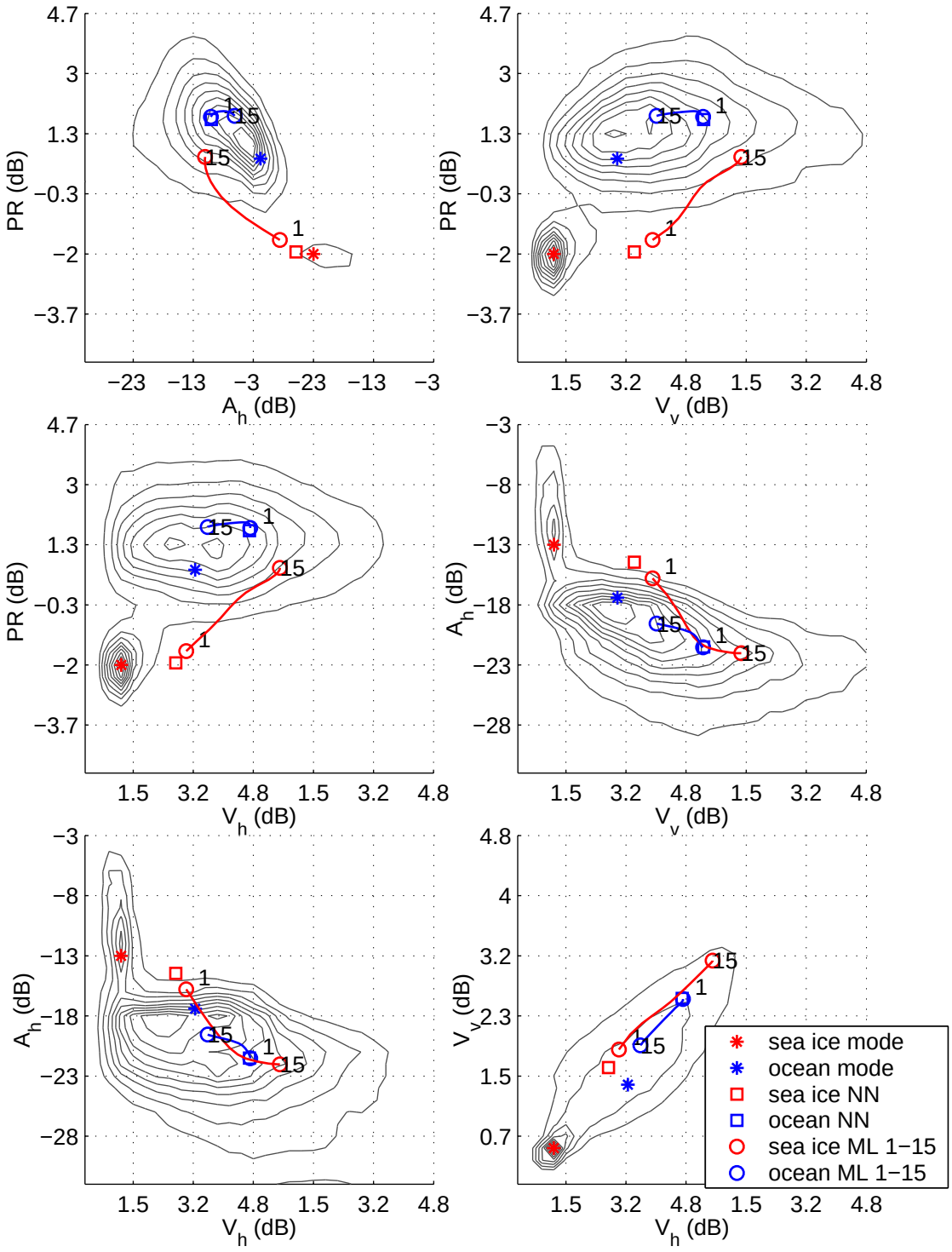

Figure 3.9: Centroid drift of sea ice and ocean means for JD 50 in the Antarctic region. Since it is difficult to illustrate centroid drift in 4-D space, the panels show a series of 2-D representations, namely (left to right, top to bottom) (1) PR vs. A_h, (2) PR vs. V_v, (3) PR vs. V_h, (4) A_h vs. V_v, (5) A_h vs. V_h, and (6), V_v vs. V_h.

back (or grown out) to the previous day's ice edge. This procedure is particularly useful in eliminating misclassification artifacts introduced by single satellite swaths which contain noise contamination, and in restoring ice edges which are misclassified as ocean due to surface melt events. This procedure is natural to implement, since the RL algorithm is typically used on a time series of data spaced a single day apart.

A shortcoming of the binary processing phase of the RL algorithm is in the assumption that the previous day's ice extent map is accurate. Growth/retreat constraints based on a faulty estimate of sea ice extent may cause artificial truncation of the true ice edge in the case of perceived sea ice growth, or dilation of the true ice edge to match the previous day's edge in the case of perceived sea ice retreat. Not only does this corrupt the ice map for the current day, but it also may propagate the faulty constraint to subsequent days in a sequence.

This motivates a second modification to the RL algorithm. The sea ice growth/retreat constraints are modified to allow for uncertainty in accuracy of the previous day's ice map. Rather than completely cropping (or fully growing out) sections of sea ice in violation of the constraint, the section of sea ice is cut (or dilated) to within a moderate distance of the previous day's ice edge. This allows the RL algorithm to recover (within a few days) from a poor ice edge constraint when applied to a sequential dataset.

A drawback to this modification is that illegitimate sections of ice protruding from the ice edge (dubbed "fingers" by Remund [3]), are not completely cropped as in the original algorithm. However, this error will be present only for a single day in the sequence (the occurrence of collocated ice tongues on consecutive days is extremely rare). This is more acceptable than allowing misclassification errors to propagate (see Figure 3.11).

3.4 Results

Although the algorithm modifications theoretically improve algorithm performance, it is important that this is verified qualitatively. It is difficult to substantiate qualitative performance in only a few examples. However, two examples are used

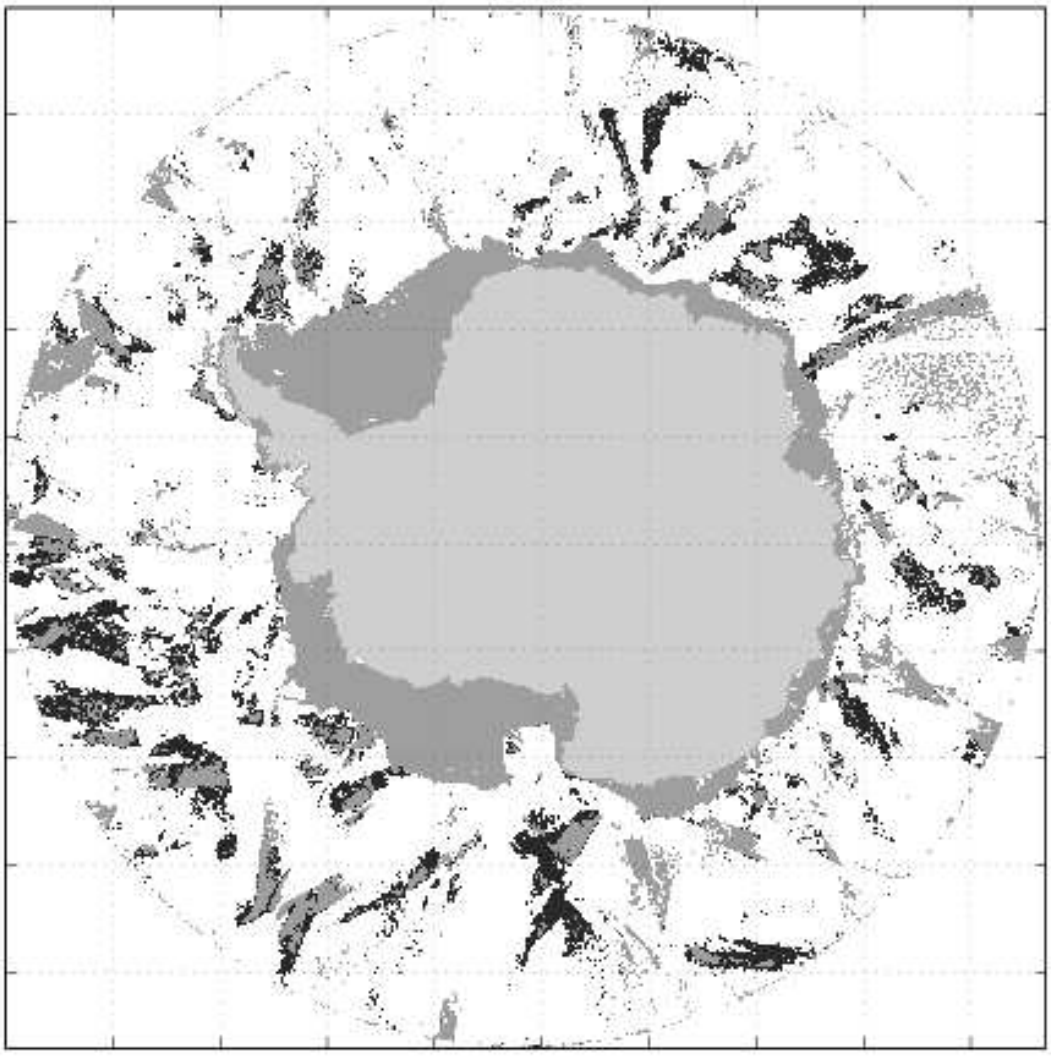

Figure 3.10: Classification map of RL algorithm using one and five iterations for the Antarctic, JD 50, 2000. Medium gray indicates the sea ice estimate at one iteration, and dark gray indicates additional misclassifications introduced by iterating five times.

to characterize the algorithm improvements. First, Figure 3.10 shows the difference in the classification results when one iteration is used as opposed to five iterations. Several large areas of misclassifications are introduced by iterating further. The most dangerous misclassifications are those which are attached to the true ice pack—these are more difficult to remove through binary processing.

Next, Figure 3.11 shows the recovery capability of the modified RL algorithm versus the original RL algorithm. The first classification image (JD 1, 2000) was generated from data with a missing satellite swath. For the original RL algorithm, subsequent ice maps in the sequence exhibit the propagated error as a result of the

Figure 3.11: Simulated recovery capability of modified versus original RL algorithm for a sequence in western Antarctic. Gray represents ice, white represents ocean, and black represents land. The left-most image (JD 1) was generated from data with a missing satellite swath. The top sequence shows JD 3-5 from the original RL algorithm, and the bottom sequence shows JD 3-5 from the modified algorithm. (JD 2 is skipped because of a complete lack of data).

assumption that the prior mask is valid. The modification allows the ice edge to recover from an invalid prior mask. In this case, complete recovery is achieved on the third day after the error.

3.5 Conclusions

Due to non-Gaussian characteristics of the RL discrimination parameters, PR, A_h, V_v, and V_h, the ML classifier in the RL algorithm does not perform optimally. In the Antarctic region, the RL algorithm diverges during the austral summer when the discrimination parameters drift significantly from Gaussian due to regional climate conditions.

In addition, the binary processing phase of the RL algorithm includes a sea ice growth/retreat constraint which assumes that a previous sea ice map in a sequence is correct. This assumption allows for propagating sea ice extent errors which are potentially unrecoverable if not checked.

The algorithm is modified to correct these two problems. First, divergence is curtailed by restricting the number of iterations of the ML classifier. Secondly, the sea ice growth/retreat constraint is modified such that the algorithm is able to recover from a previous day's poor ice extent map within a few days, without user intervention.

The modifications to the RL algorithm improve its performance in accuracy, autonomy, and robustness. These changes have been implemented at JPL for near real-time (NRT) wind retrieval, and at NOAA for sea ice studies. The modifications (and the preceding analysis) also provide insight about the RL algorithm's strengths and weaknesses, and prelude the development of a new algorithm in Chapter 4.

Chapter 4

Adaptive Sea Ice Mapping Algorithm for SeaWinds

4.1 Introduction

The previous chapter addresses the seasonal convergence characteristics of the Remund Long (RL) sea ice mapping algorithm for SeaWinds [2, 3]. The non-Gaussian characteristics of polar sea ice, as well as a desire to reduce the method's dependence on binary processing techniques, motivate the development of an improved sea ice mapping algorithm. In this chapter, a method is developed in which statistical and spatial *a priori* information are used to produce an estimate of polar sea ice extent. The new method is designed to adapt to temporal changes in the discrimination parameters—it incorporates a novel statistical modeling approach to account for the departure from Gaussian of the parameters. This work has been submitted to the journal *IEEE Transactions on Geoscience and Remote Sensing*.

As discussed in Chapter 2, the Remund-Long (RL) sea ice extent algorithm for SeaWinds (an adaptation of an earlier version for NSCAT [4]) is an iterative maximum likelihood (ML) discrimination approach based on four discrimination parameters: PR, A_h, V_v, and V_h. Statistics for four-dimensional data are initialized by segmenting sea ice and ocean using a nearest neighbor (NN) approach. ML discrimination is then applied iteratively to segment sea ice and ocean populations statistically. This results in an initial estimate which generally contains residual noise caused by wind-roughened ocean surfaces or other microwave signature anomalies. The RL algorithm filters this noise through a sequence of binary processing operations and through sea ice growth/retreat constraints using sea ice extent information from a previous day.

The RL sea ice extent algorithm for SeaWinds has been successfully applied to enhanced resolution science and near real-time (NRT) data. The algorithm applied to several years of enhanced-resolution SeaWinds data now available show that the binary processing stage of the RL algorithm corrects the majority of the residual errors in the initial classification.

This document presents a modified Bayes detection approach to segment polar sea ice and ocean using imagery derived from the SeaWinds instruments on QuikScat and ADEOS-II. The proposed algorithm has its roots in the RL sea ice extent algorithm for SeaWinds, using a multivariate statistical approach with discrimination parameters PR, A_h, V_v, and V_h. However the algorithm differs from the RL approach in several areas. First, statistical *a priori* estimates of sea ice and ocean are incorporated. Secondly, spatial *a priori* information is applied in the initial classification phase, as opposed to a post-processing phase (RL algorithm growth/retreat constraints). Next, the RL algorithm implicitly assumes that the discrimination parameters are jointly Gaussian, whereas the proposed algorithm incorporates a data-driven empirical model which is constrained by a set of previously observed distributions.

The algorithm is presented as follows. Section 4.2 presents the development of the new algorithm within the framework of Bayes detection. Results of the new method, as well as comparisons to the RL algorithm, NASA Team algorithm for SSM/I, and RadarSat ScanSAR imagery, are shown in Section 4.3. In conclusion, Section 4.4 offers a brief summary of the strengths of the new approach, and suggests other applications of the classification approach.

4.2 Algorithm Development

In this section, a new method for sea ice discrimination is developed. The development of an adaptive statistical model for polar sea ice and ocean is outlined in Section 4.2.1. A Bayes detection approach, which facilitates the inclusion of *a priori* information, is detailed in Section 4.2.2. Spatial *a priori* information is incorporated in Bayes loss functions, as discussed in Section 4.2.3. With this framework, the algorithm in its entirety is presented in 4.2.4.

4.2.1 Empirical Model Parameterization

As shown in the previous chapter, the selected discrimination parameters generally exhibit Gaussian distributions throughout most of the year. However, anomalous weather conditions and fluctuating sea ice properties during the melt season cause sea ice and ocean statistics to deviate from Gaussian, as evidenced in Chapter 3. These anomalies lead to misclassifications and in some cases, algorithm divergence.

The dynamic nature of the distributions of the RL discrimination parameters over sea ice—which are sometimes Gaussian, sometimes bimodal (Arctic A_h), and sometimes suggestive of Chi-squared distributions (V_v and V_h)—present a challenge in multivariate statistical modeling. More general statistical models, such as the generalized lambda family of distributions [23], can be computationally intensive, and mathematically awkward to implement, especially in the multivariate case for which only an approximation may be constructed from marginal distributions via contingency tables [24, 25].

The need for versatility elicits the use of an empirical model. Empirical models are potentially adaptive, but have several disadvantages: they are sensitive to noise, have less analytical value than a theoretical model, and have large memory requirements for finely binned data. For an n-dimensional histogram of b bins for each dimension, the storage requirement is b^n memory units.

As will be shown later, sea ice/ocean segmentation requires two individual 4-D histograms of the discrimination parameter imagery—one for sea ice and one for ocean. For each histogram, it is desirable to reduce the storage requirement and misclassification induced bin height error (noise). This is achieved by parameterizing each histogram by a basis set of expected histograms. The basis set is generated by treating the histograms as images, and extracting the principal components (PCs) from a time-series ensemble of sea ice or ocean histograms via singular value decomposition (SVD). The resulting set of PCs span the space of observed sea ice or ocean histograms. The PCs allow the approximation of any sea ice or ocean distribution from a similar time period using only a few parameters—the weights associated with mapping the distributions onto the truncated set of PCs. A review of the SVD for

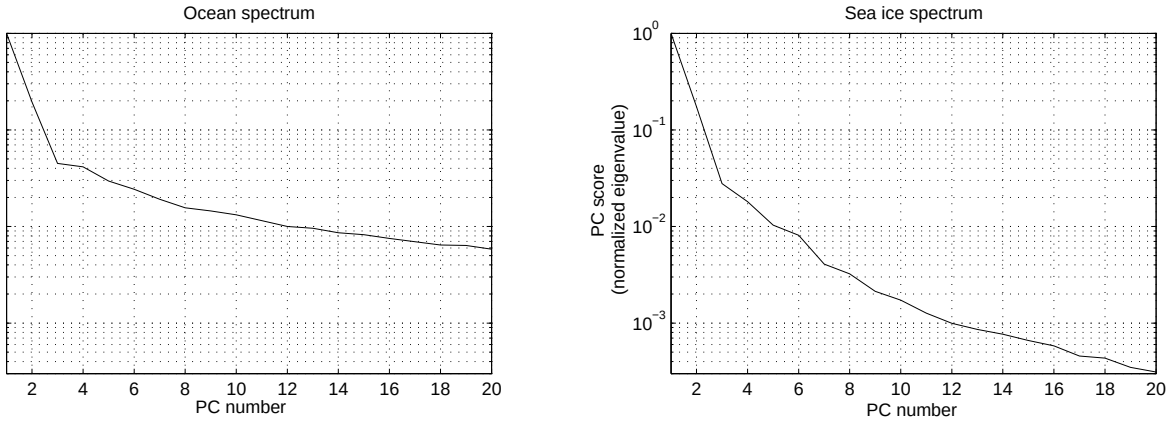

Figure 4.1: Spectrum of first 20 PC eigenvalues of (left) Arctic ocean histograms and (right) Arctic sea ice histograms. This shows energy compaction in the top few PCs.

extracting PCs and a method for efficiently computing the SVD of large datasets [26] is given in Appendix A.

Sea ice extent masks generated by the RL algorithm are used to separate sea ice and ocean populations in RL discrimination parameter (PR, A_h, V_v, and V_h) imagery. Four-dimensional histograms for sea ice and ocean are generated from this data for each day of the year 2001. The PCs of the time-series ensemble of histograms are found using the SVD, as mentioned above. The PC scores (the eigenvalues of the histogram ensemble's correlation matrix normalized by the largest eigenvalue) are shown for Arctic sea ice and ocean in Figure 4.1. The first PC for sea ice and ocean represents the "average" component in the time-series ensembles of histograms. For this reason, the first PC in both cases dominates the PC spectrum. It is also evident that the Arctic sea ice spectrum falls off more rapidly than the ocean spectrum. This is due to high variations in ocean histograms due to ocean storms.

The first three PCs for Arctic ocean and sea ice are shown in Figures 4.2 and 4.3, respectively. As expected, the first PC for ocean histograms (the "average" histogram) is Gaussian in shape, and the first PC for Arctic sea ice histograms is bimodal.

Operationally, histograms are generated for sea ice and ocean via sea ice extent masks that may contain misclassification errors. The resulting sea ice histograms contain ocean contamination, and the ocean histograms contain sea ice contamination.

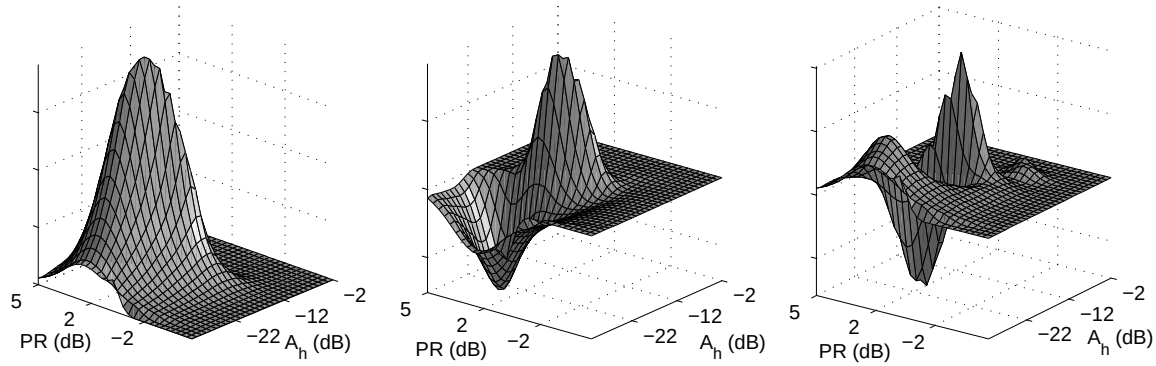

Figure 4.2: The first 3 PCs of Arctic ocean histograms for the year 2001. Two-dimensional representations (PR vs. A_h) are shown.

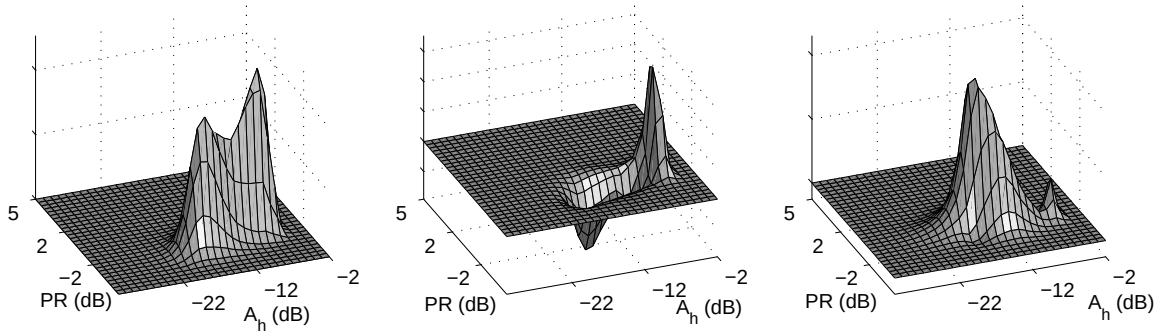

Figure 4.3: The first 3 PCs of Arctic sea ice histograms for the year 2001. Two-dimensional representations (PR vs. A_h) are shown.

These "noisy" histograms are parameterized using a truncated set of the sea ice/ocean histogram PCs. The histogram reconstructed from PCs conforms to the ensemble of sea ice and ocean histograms used to generate the basis set, i.e., the truncated PC basis set functions as a filter to eliminate unexpected components of the "noisy" histogram's shape. An example of this noise-reduction property is shown in Figure 4.4. On the other hand, histograms which already conform to the set of expected shapes do not experience significant distortion through the reconstruction process, as evidenced in Figure 4.5.

It is important to note that a parameterized histogram is only an estimate of the true histogram. The estimate may be improved by noting that bin heights for each bin must be greater than zero. Hence, negative bin heights are set equal to zero. Also,

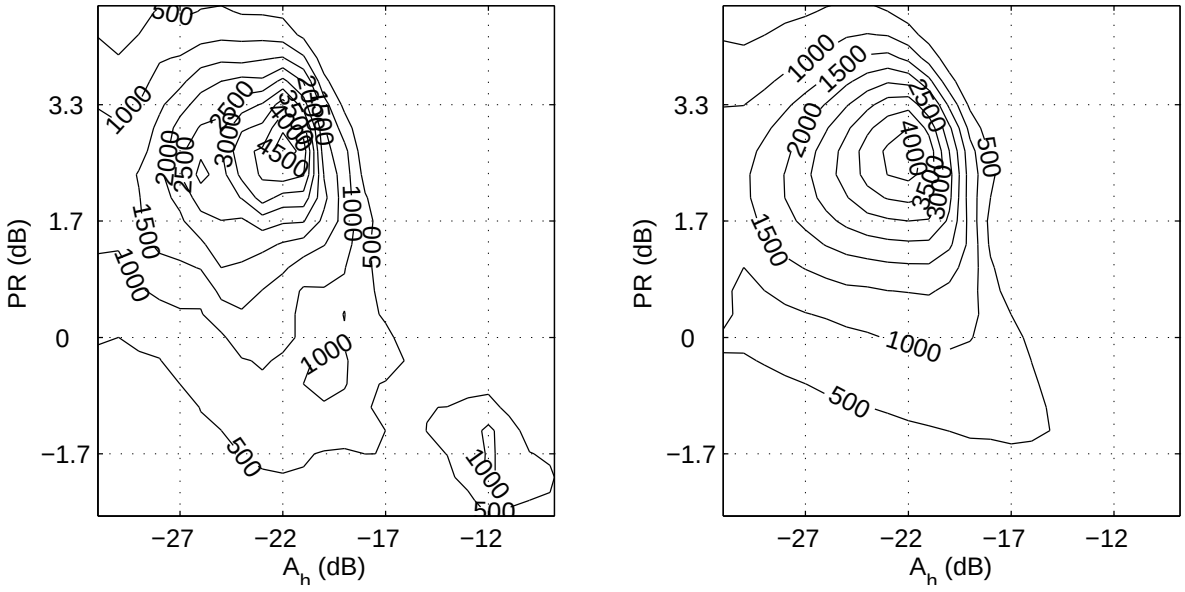

Figure 4.4: Histogram parameterization using Arctic ocean histogram PCs: (left) original (observed) histogram which includes a segment of sea ice contamination (lower right of sub-figure), and (right) parameterized histogram showing that the sea ice contamination has been filtered. Contour labels are pixel counts.

population size is generally not maintained in the parameterizing process. As will be shown later, the relative population sizes of sea ice and ocean are an important factor in Bayes detection. If the relative population sizes are known, the parameterized histograms may be normalized to reflect this knowledge. These modifications to the parameterized histograms have been implemented in Figures 4.4 and 4.5.

In summary, histograms are selected to model dynamic sea ice and ocean statistics. Since histograms are sensitive to contamination caused by misclassifications, the histograms are parameterized by the PCs of observed sea ice or ocean histograms. This parameterization, in effect, filters out contamination shape distortions in the histogram. Using this model for both the Arctic and the Antarctic (not shown in this section), the dynamic nature of polar sea ice and ocean distributions are captured in a way that rejects contamination, but maintains shape diversity.

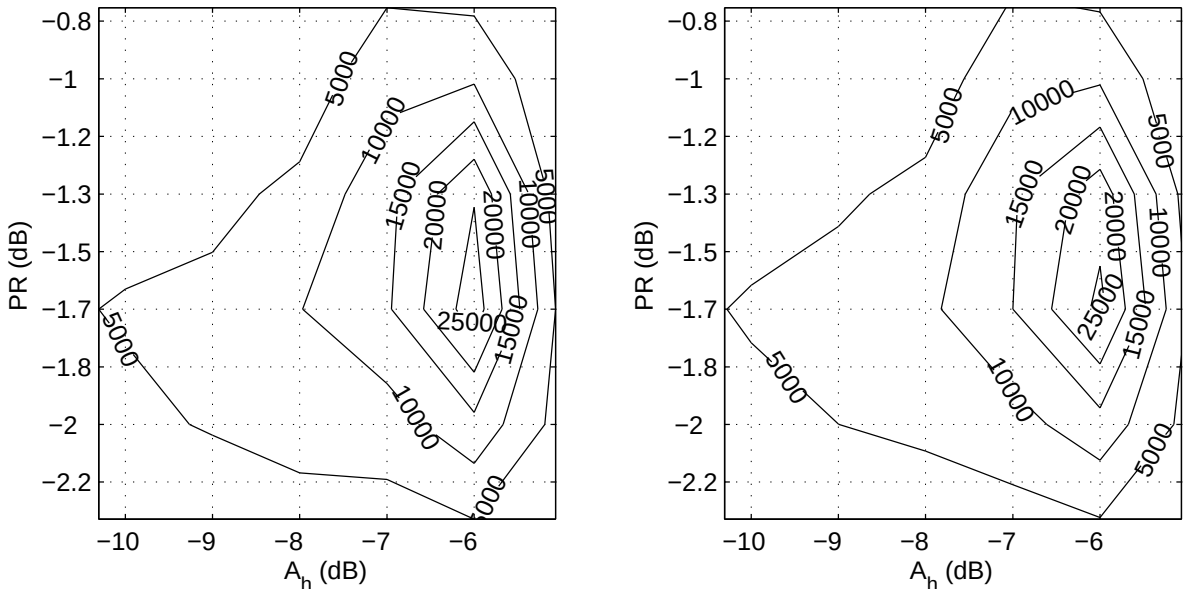

Figure 4.5: Histogram parameterization using Arctic sea ice histogram PCs: (left) original (observed) sea ice histogram, and (right) parameterized histogram revealing that no significant distortion occurred in the reconstruction process. Contour labels are pixel counts.

4.2.2 Binary Bayes Detection: Polar Sea Ice Discrimination

Four SIR image products—PR (derived), A_h, V_v, and V_h—are used in concert as discrimination parameters to detect sea ice. Since it is helpful to incorporate *a priori* information in an estimate of polar sea ice extent, the algorithm is developed within the framework of Bayes detection, where a decision rule $\phi(\mathbf{z})$ selects sea ice or ocean based on an observation $\mathbf{z}$, and depending on the Bayes risk $R(\cdot)$ associated with that decision,

$$\phi(\mathbf{z}) = \begin{cases} \text{sea ice}, & \text{if } R(\text{sea ice}|\mathbf{z}) < R(\text{ocean}|\mathbf{z}) \\ \text{ocean}, & \text{otherwise.} \end{cases} \tag{4.1}$$

The algorithm is designed for pixel-based classification, in which observations $\mathbf{z} = [\text{PR } A_h \; V_v \; V_h]$ for each pixel at position (x, y) and time t (in Julian days) are used to determine the Bayes risk. Bayes risk is related to the probability $P(\cdot)$ that a hypothesis $H_i^{x,y,t}$ (the pixel belongs to class i) is correct given the observation $\mathbf{z}$. The decision rule selects the hypothesis ($H_1^{x,y,t}$ for sea ice and $H_0^{x,y,t}$ for ocean) which

results in a minimum Bayes risk,

$$R(H_i^{x,y,t}|\mathbf{z}) = P(H_i^{x,y,t}|\mathbf{z})L_{ij}^{x,y,t}, \tag{4.2}$$

where $L_{ij}^{x,y,t}$ is an arbitrarily assigned loss for selecting $H_i^{x,y,t}$, given that $H_j^{x,y,t}$ is correct. In practice, it is difficult and sometimes impossible to calculate the probability in Equation (4.2) for every pixel. In image processing, a common practice is to treat the pixel statistics as ergodic, i.e., the pixel statistics are approximately equal to the ensemble statistics. With this simplification, but retaining the general form for the loss, Equation (4.2) reduces to

$$R(H_i^{x,y,t}|\mathbf{z}) = P(H_i^{t}|\mathbf{z})L_{ij}^{x,y,t}. \tag{4.3}$$

In this form, inaccuracy introduced by neglecting spatial dependence in the $P(H_i^t|\mathbf{z})$ may be accounted for by careful selection of $L_{ij}^{x,y,t}$.

Equation (4.3), written in terms of the *posteriori* probability, may expressed in terms of the *a priori* probability using Bayes theorem. To facilitate a binary decision (sea ice or ocean) using a likelihood ratio test, Bayes risk is expressed in terms of a conditional distribution [27]. This results in an effective decision rule $\phi(\mathbf{z})$ for an observation $\mathbf{z}$,

$$\phi(\mathbf{z}) = \begin{cases} 1, & \text{if } f(\mathbf{z}|H_1^t)P(H_1^t)L_{10}^{x,y,t} > f(\mathbf{z}|H_0^t)P(H_0^t)L_{01}^{x,y,t} \\ 0, & \text{otherwise.} \end{cases} \tag{4.4}$$

In this formulation, $\phi(\mathbf{z})$ selects 1 if for sea ice is more likely, and 0 otherwise. The decision threshold is adjusted by the priors and the costs associated with the decision. Rather than selecting a functional form for $f(\mathbf{z}|H_i^t)$, the conditional distributions are approximated using histograms (not normalized) to allow for temporal variations of sea ice and ocean. Equation (4.4) becomes

$$\phi(\mathbf{z}) = \begin{cases} 1, & \text{if } h(\mathbf{z}|H_1^t)L_{10}^{x,y,t} > h(\mathbf{z}|H_0^t)L_{01}^{x,y,t} \\ 0, & \text{otherwise.} \end{cases} \tag{4.5}$$

Note that the prior probabilities are reflected in the relative heights of the histograms.

The Bayes detection formulation in Equation (4.5) allows for a simple pixel-based test of ensemble sea ice and ocean histograms (4-dimensional), where the loss

terms essentially shift the threshold of the decision. The choice to assume ergodicity for the probability in Equation (4.2), but not for the loss terms, is somewhat cavalier but will be justified in the following section.

4.2.3 Loss Maps

The value assigned to $L_{ij}^{x,y,t}$ can be arbitrarily chosen and, in practice, is used to reflect the *a priori* belief that the hypothesis $H_i^{x,y,t}$ is correct. The relative values of the loss terms in the decision rule of Equation (4.5) shift the decision threshold by scaling the histograms. Using $L_{ij}^{x,y,t}$ as a measure of prior belief, we may relate it to the probability that the observed pixel belongs to class i, given that it belonged to class j yesterday; in effect,

$$L_{ij}^{x,y,t} \sim P(H_i^{x,y,t} | H_j^{x,y,t-1}). \tag{4.6}$$

We implement $L_{ij}^{x,y,t}$ as a look-up table that retrieves a loss value for pixel location (x, y). (For convenience, the values are restricted to the range $[0, 1]$.) For sea ice mapping, we set $L_{ij}^{x,y,t}$ based on sea ice extent maps from the previous day. Since the ice edge may move several kilometers in a single day, and the sea ice extent map from the previous day may over- or under-represent the true sea ice edge, we allow for sea ice growth and imperfect sea ice maps. Thus, $L_{01}^{x,y,t}$ is generated using a dilated version of the previous day's sea ice extent map. Likewise, $L_{10}^{x,y,t}$ is generated using a dilated version of its complement (an ocean extent map). The sea ice loss look-up table is filled with high values (near unity) where yesterday's dilated ocean mask predicts ocean, and low values (near zero) where yesterday's dilated ocean mask predicts sea ice. Conversely, the ocean loss look-up table is filled with high values where yesterday's dilated ice mask predicts sea ice, and low values where yesterday's dilated ice mask predicts ocean.

The ratio of the loss maps $L_{01}^{x,y,t}/L_{10}^{x,y,t}$ adjusts the threshold for the decision rule in Equation (4.5). This ratio determines the classification result if the bin heights of $h(\mathbf{z}|H_1^t)$ and $h(\mathbf{z}|H_0^t)$ for an observed $\mathbf{z}$ are equal. The dilation procedures used in forming the loss maps create a region where equal loss is assigned to both sea

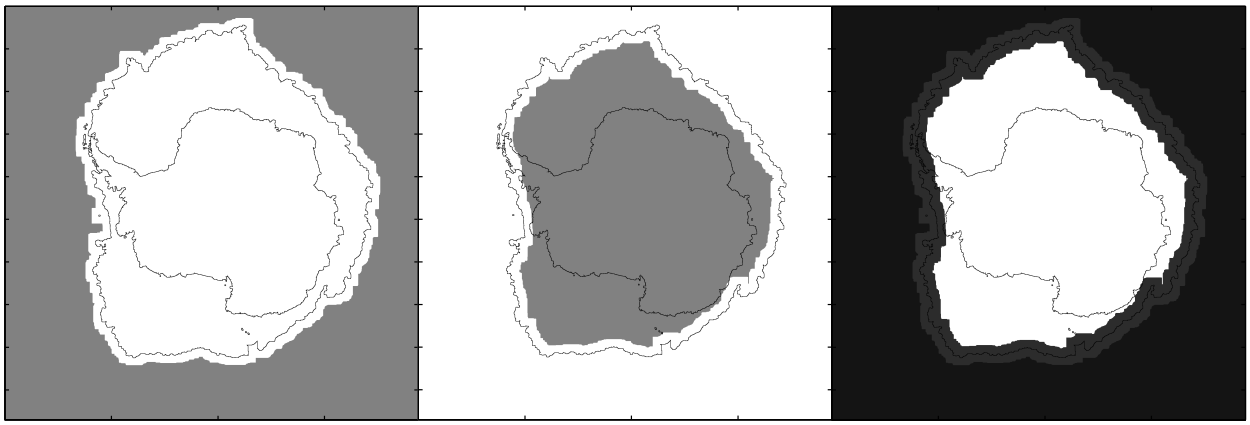

Figure 4.6: (left) ocean loss map, (middle) ice loss map, (right) default decision rule showing the region of ignorance around the ice edge. In each case dark shades represent low values, while light shades represent high values. Although the algorithm may be applied to both the Arctic and Antarctic regions, the Antarctic region is shown for clarity.

ice and ocean. In this region of ignorance where $L_{01}^{x,y,t} = L_{10}^{x,y,t}$ (where spatial *a priori* information is inconclusive), the unweighted ratio of the sea ice and ocean histograms determines the classification. Sample loss maps and the corresponding default decision rule is shown in Figure 4.6.

4.2.4 Iterative Bayes Detection Algorithm

The Bayes detection approach is used iteratively to produce polar sea ice extent maps from SeaWinds data. First, an initial estimate of sea ice extent is produced using histograms for sea ice and ocean from the previous day. Loss maps $L_{01}^{x,y,t}$ and $L_{10}^{x,y,t}$ are generated from ice extent maps from the previous day. Here, it is assumed that the statistics and spatial distribution for sea ice and ocean do not change significantly in a single day, except for sea ice growth in the region of ignorance.

Since sea ice and ocean statistics and spatial distributions do, however, exhibit diurnal variations, this initial estimate generally contains classification errors. To reduce the number of misclassified pixels, the initial classification is used to generate statistical and spatial information for another iteration of the classifier. This process is repeated until convergence is reached.

A simple method is implemented in the iteration process which promotes spatial homogeneity of the sea ice classification. A logical assumption is that if the observation $\mathbf{z}$ has been flagged as sea ice, then the neighbors of $\mathbf{z}$ are likely to also be sea ice. Hence, pixels in the neighborhood of $\mathbf{z}$ are considered candidates for classification as sea ice by adding their observations $\mathbf{z}$ to the sea ice histogram. This step is implemented prior to each iteration by dilating the classification map used to generate statistical information.

This spatial inclusion step aids in the method's ability to recover from poor statistical *a priori* information. In the case where initial sea ice statistics are "too narrow" to include all of the true ice pixels, spatial inclusion helps to "broaden" the sea ice distribution in subsequent iterations. In the case where initial sea ice statistics are "too broad", spatial inclusion potentially leads to even larger misclassified regions. Fortunately, spatial inclusion can be checked by proper selection of the loss maps $L_{01}^{x,y,t}$ and $L_{10}^{x,y,t}$.

Since initial loss maps $L_{01}^{x,y,t}$ and $L_{10}^{x,y,t}$ are constructed to allow for sea ice growth/retreat, the region of ignorance around the sea ice edge may be large. As noted previously, the loss maps do not influence the decision rule within this region. This can result in misclassifications if the discrimination parameters exhibit microwave signature anomalies within the region. To increase the efficacy of the loss maps as the algorithm nears convergence, the loss maps are updated at each iteration to reflect the new sea ice location from the most recent classification. Also, the loss maps are updated at each iteration so that the region of ignorance contracts. This is accomplished through a simple simulated annealing update step,

$$\hat{L}_{01}^{x,y,t} \leftarrow (1-\alpha)\,\hat{L}_{01}^{x,y,t} + \alpha L_{ij}^{x,y,t} \qquad (4.7)$$
$$\alpha \in [0,1]$$

where α is a forgetting factor, $\hat{L}_{01}^{x,y,t}$ is the adaptive position-conformal loss map, and $L_{ij}^{x,y,t}$ is a loss map created from the classification results of each iteration. To force the region of ignorance to contract, each new loss map $L_{ij}^{x,y,t}$ in the iteration sequence is created using fewer dilations of the sea ice classification map than the loss map

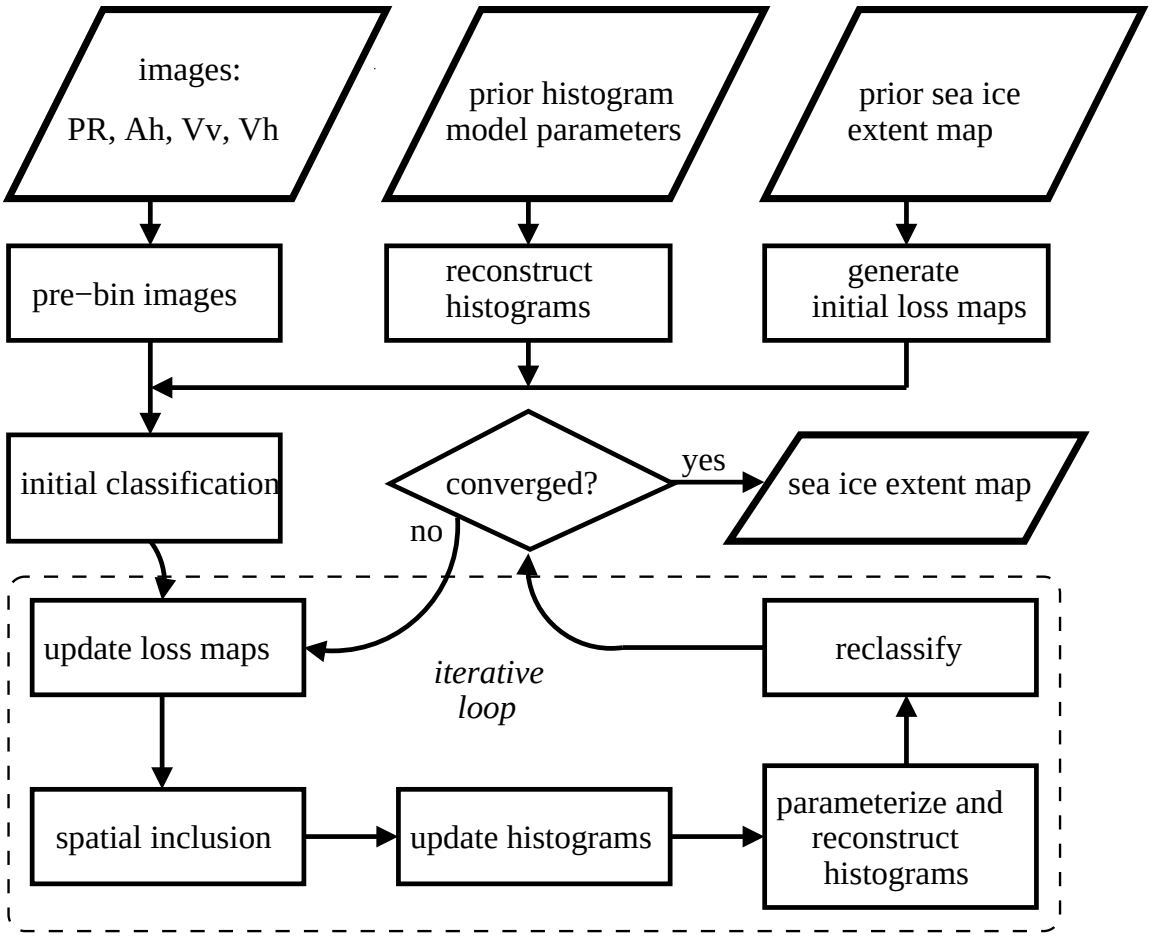

Figure 4.7: Flowchart of sea ice mapping algorithm when used with a time series of data.

of the previous iteration. The initial loss map is created from an estimate of sea ice extent from a previous day, as described previously, using the most number of dilations.

A diagram detailing the flow of the algorithm is shown in Figure 4.7. Implicit in the flow of the algorithm is the existence of the PCs for sea ice and ocean histograms, as described in Section 4.2.1. A sample sea ice extent map for the Arctic region is shown in Figure 4.8.

4.2.5 Tuning Parameters

The algorithm flowchart presented in Figure 4.7 provides a high-level view of sea ice mapping process. However, unlike the RL algorithm, the new method provides

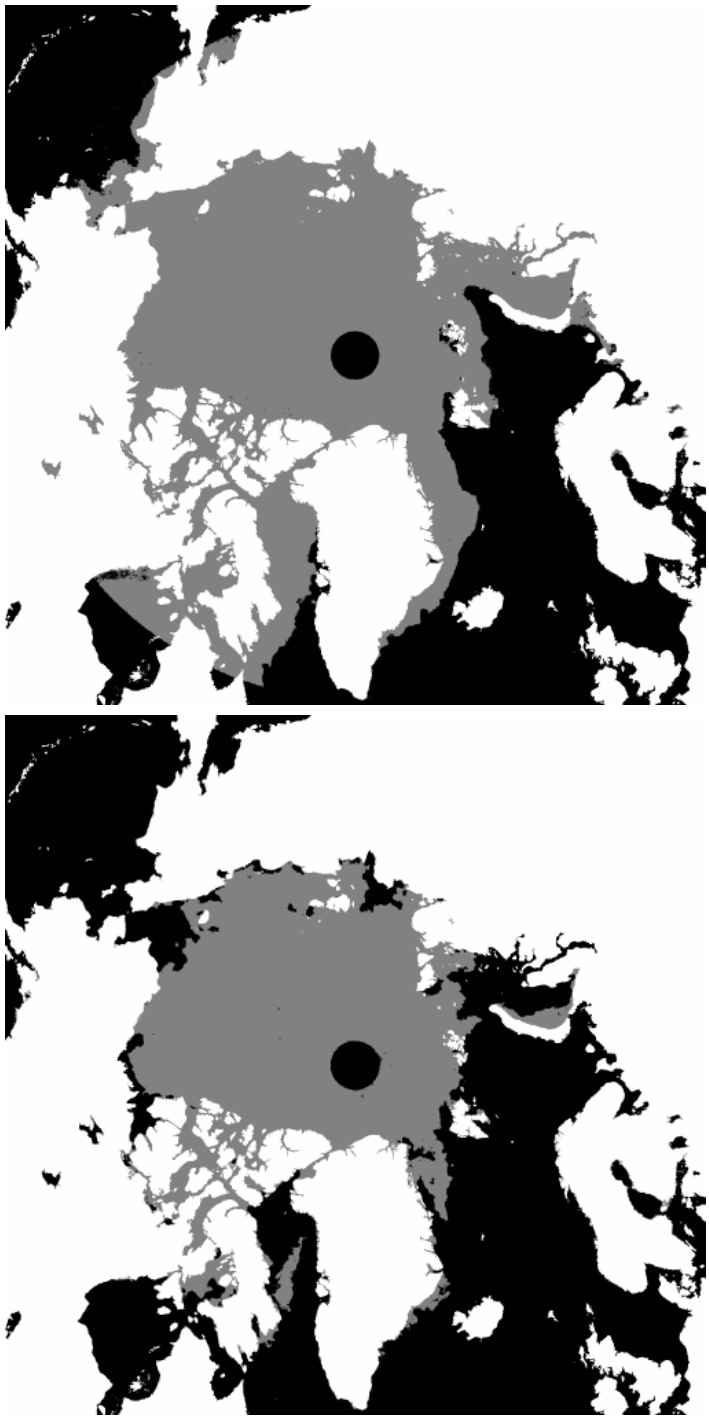

Figure 4.8: Sample output of the modified Bayes algorithm. Prior information was obtained via an ice extent map produced by the RL algorithm. Shown are the ice maps for JD 6, 2001 (top) and JD 206, 2001 (bottom).

Table 4.1: Tuning parameters used in this study

Tuning parameter	**Value**
USEVECS	40
number of iterations	3
MAXGROW	20
MINGROW	1
LM_ERODE	5
LOSSCEIL	1.0
LOSSFLOOR	0.05
α	0.2
SI_ERODE	1
SI_DILATE	3

several tuning parameters which may be set to provide "optimal" performance of the algorithm on a particular dataset. These tuning parameters are briefly discussed here. The specific values for the tuning parameters used for producing the Arctic egg sea ice maps validated in Section are shown in Table 4.1. The performance of the algorithm is not particularly sensitive to the exact values of these parameters.

Principle Components

The performance of the algorithm may be "trained" for performance similar to another algorithm by proper computation of the PCs of sea ice and ocean histograms. In this study, histograms used to calculate the PCs are generated using fifty interspersed sea ice extent maps for 2001 produced by the RL algorithm. These sea ice extent maps—which are subjectively validated—are overlayed on PR, A_h, V_v, and V_h imagery to generate separate histograms for sea ice and ocean. From the resulting histograms, an orthogonal basis is extracted: the principal components. The principal components are ordered by the magnitude of the eigenvalue associated with the PC. While the full basis may be computed, the ordered basis set is truncated to a length which spans most of the space of the histograms.

Reconstruction Coefficients, USEVECS

The accuracy of reconstructing histograms from principal component vectors may be adjusted by restricting the number of vectors, USEVECS, used in reconstruction. For large USEVECS, reconstructed histograms contain more detail, and allow more bin-height errors to pass through the filtering process. However, for too small USEVECS, accurate reconstruction of the histograms is not possible. Thus, a tradeoff is required. For the Arctic region, it was found that 40 PCs allowed for accurate reconstruction of sea ice and ocean histograms. The algorithm performance, however, was found to be insensitive to the exact value of USEVECS, as long as a sufficient number (e.g., thirty to fifty) of PCs are used to allow for accurate representation of the histograms.

Number of Iterations

When good prior data is available, the number of iterations does not affect the algorithm performance significantly. In this case, convergence is typically reached after only three iterations. However, if poor prior data are supplied to the algorithm, more iterations are required for the algorithm to recover. The recovering capability of the algorithm is also a function of the values used to create the adaptive loss maps $\hat{L}_{ij}^{x,y,t}$, α, and the extent of spatial inclusion. The effects of the latter tuning parameters are a function of the total number of iterations. Limiting the number of iterations to three is generally adequate.

Loss Map Dilation, MAXGROW and MINGROW

The extent of dilation used when creating loss maps $L_{ij}^{x,y,t}$ limits how far we believe the sea ice edge can move in a single day (for $n = 0$), or how much we "trust" the classification map of the nth iteration (for $n > 0$). Typically, loss maps are created initially using many dilations, MAXGROW, and the region of ignorance is forced to contract by using successively fewer iterations, until the final iteration, where MINGROW iterations are used. For this study, the intermediate iterations use the number dilations linearly between MAXGROW and MINGROW. Values of MAXGROW between

ten and forty are sufficient for most cases, while a value of zero to five for MINGROW yield good performance.

Loss Map Erosion, LM_ERODE

If classification maps at the nth iteration contain misclassification errors (speckle noise), then the loss maps may contain corrupted loss values over a potentially large area, depending on the extent of dilation. To ameliorate this, the loss maps are eroded prior to dilation (an unbalanced binary "opening" operation) by a factor of LM_ERODE. LM_ERODE is chosen based on the general observed maximum size of misclassified regions.

Maximum and Minimum Loss Values, LOSSFLOOR and LOSSCEIL

As discussed previously, the relative values of sea ice and ocean loss maps convey how much the classification map of the previous day (or previous iteration) is trusted. For convenience, loss values are restricted to $[0, 1]$. When creating loss maps, areas of high loss are assigned to the value LOSSCEIL, and areas of low loss are assigned to the value LOSSFLOOR.

Loss Map Forgetting Factor, α

The adaptive loss map forgetting factor, α, is also related to how much we trust classification maps of past iterations. For small values of α, the algorithm is driven mostly by the current classification map.

Spatial Inclusion Dilation and Erosion, SI_ERODE and SI_DILATE

As discussed previously, spatial inclusion is implemented to promote spatial homogeneity and help the algorithm to recover from potentially poor prior data. This is implemented via an unbalanced binary opening operation (a small erosion followed by a larger dilation). The extent of erosion and dilation in the spatial inclusion step are defined by SI_ERODE and SI_DILATE. The extent of dilation is related to much we

"trust" (or do not trust, rather) the prior data. Large values of `SI_DILATE` result in faster recovery from poor prior data, but may lead to noise amplification.

4.3 Results

The technique described above is used to generate polar sea ice extent maps for the Arctic region for each day of 2001 from SIR egg data. A three-sample temporal (non-causal) median filter is used on the sequence to reduce speckle noise. The median filter preserves spatial and temporal resolution. The resulting ice extent maps are suitable for a variety of applications including wind retrieval, sea ice extent estimation, and sea ice motion studies. In this section, the ice extent maps are compared to those produced by the RL algorithm, the SSM/I NASA Team algorithm, and RadarSat ScanSAR imagery.

4.3.1 Comparison with the RL Algorithm

Generally, the ice edge determined from the sea ice maps produced by the new method are highly correlated to the sea ice edge inferred from the RL algorithm for SeaWinds. The RL algorithm reports, on average, 1.6% more total area covered by sea ice than the modified Bayes approach described here—0.5% more in the boreal winter and 2.9% more in the boreal summer. Figure 4.9 shows the total sea ice area reported by both algorithms as a function of Julian day. The overall discrepancy may be primarily ascribed to the fact that the new technique does not perform binary processing techniques to remove polynias in the ice sheet, as does the RL algorithm. The large difference in the boreal summer (JD 200–300) is due to the affect of surface melt events which are classified as ocean, but corrected in the binary processing phase of the RL algorithm. Here, the reported sea ice area is somewhat ambiguous for both algorithms, due to the effects of sea ice motion and surface melting on V_h and V_v. The discrepancy in the early spring (JD 125-155) is due to sensor outage and misclassifications in the RL algorithm due to large-scale surface melting in the Hudson Bay area.

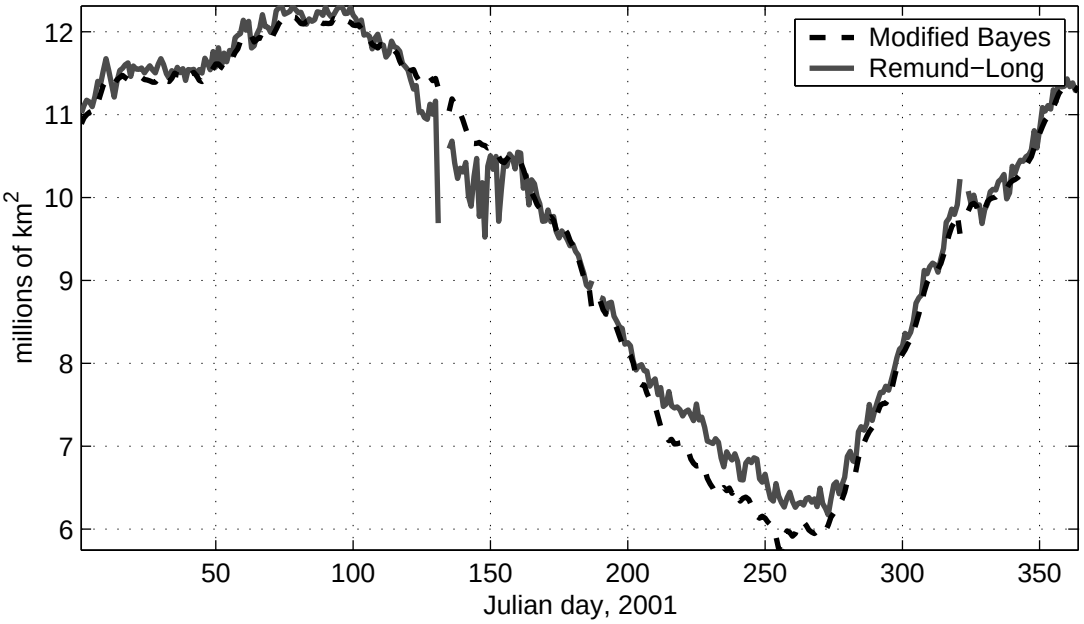

Figure 4.9: Total Arctic sea ice area for 2001 reported by the modified Bayes algorithm (black dashed) and the RL algorithm for SeaWinds (gray solid).

A qualitative comparison of the performance of the two algorithms is difficult to assess. However, four cases are presented here which represent observed general performance. Figure 4.10 shows a case in the boreal winter in which the performance of both algorithms is satisfactory. This case is representative of the majority of results in the boreal winter. Figure 4.11 shows a case, also in the winter, in which ocean storms adjacent to the ice edge induce misclassification errors in the RL algorithm, but do not significantly affect the results of the modified Bayes algorithm. This is a typical occurrence in the boreal winter at times when ocean storms are prevalent. The Figure 4.12 is representative of cases in which surface melting causes misclassification errors in both algorithms. However, these errors are corrected in the binary processing phase of the RL algorithm. Finally, Figure 4.13 is representative of cases where surface melting and sea ice motion creates ambiguity in V_v and V_h imagery and causes misclassification errors in both algorithms. This last two cases are most common in the boreal summer (JD 200-300 in Figure 4.9).

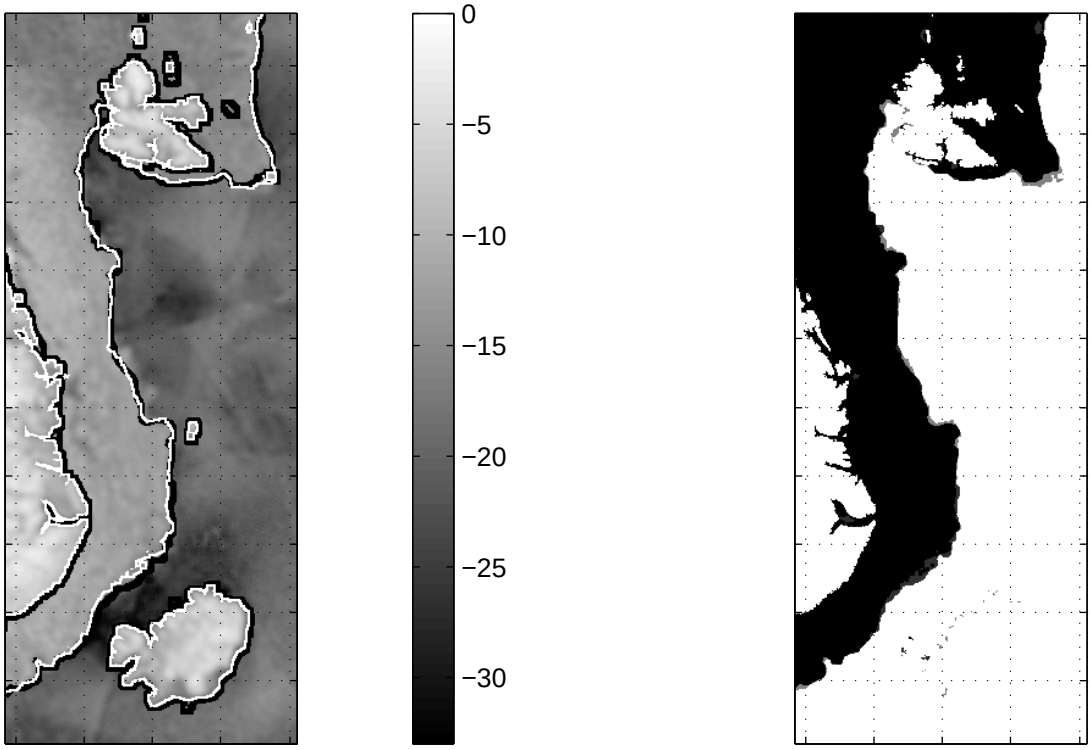

Figure 4.10: Ice edge comparison of modified Bayes (white) and RL (black) algorithms overlayed on A_h imagery (left). The color scale is in dB. The mask comparison (right) shows pixels which are common between the two algorithms (black), pixels unique to the modified Bayes algorithm (light gray), and pixels unique to the RL algorithm (dark gray). Here, the algorithms perform very similarly. Shown is JD 88, 2001. The center pixel is at 73.1° N, 8.75° W. Grid spacing is 250 km.

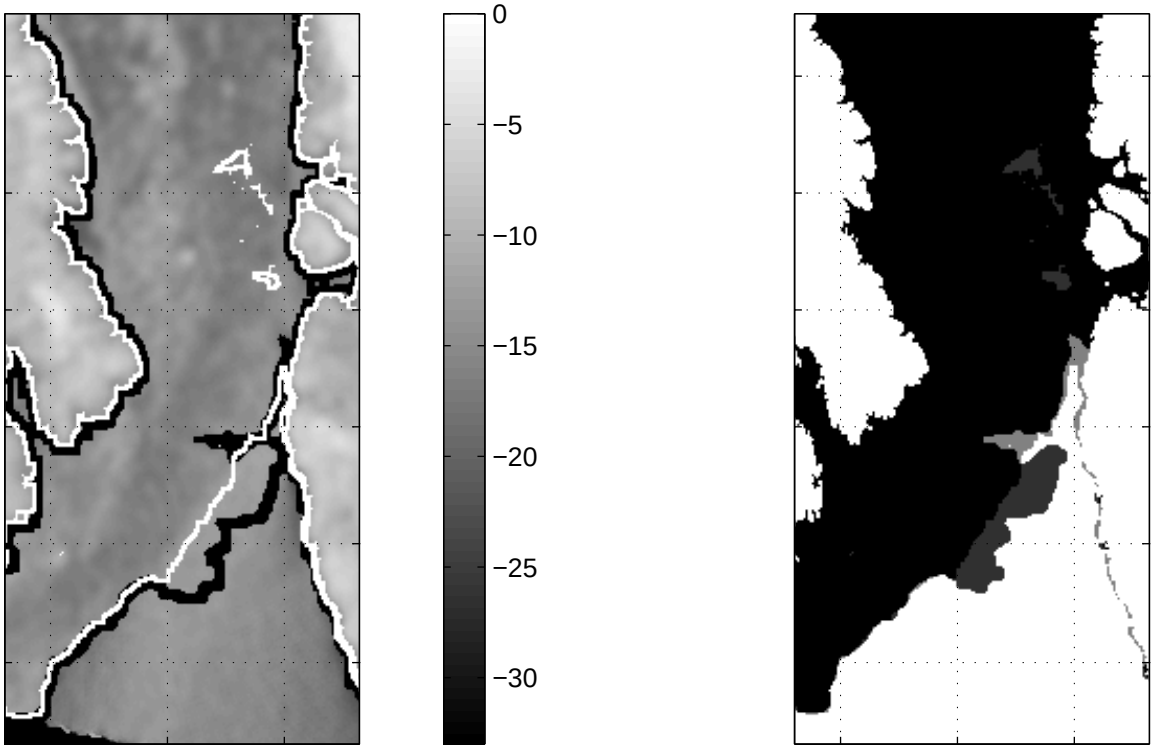

Figure 4.11: Ice edge comparison of modified Bayes (white) and RL (black) algorithms overlayed on A_h imagery (left). The color scale is in dB. The mask comparison (right) shows pixels which are common between the two algorithms (black), pixels unique to the modified Bayes algorithm (light gray), and pixels unique to the RL algorithm (dark gray). Here, the RL sea ice map contains a wind-induced misclassification error. Shown is JD 88, 2001. The center pixel is at 66.6° N, 59.1° W. Grid spacing is 250 km.

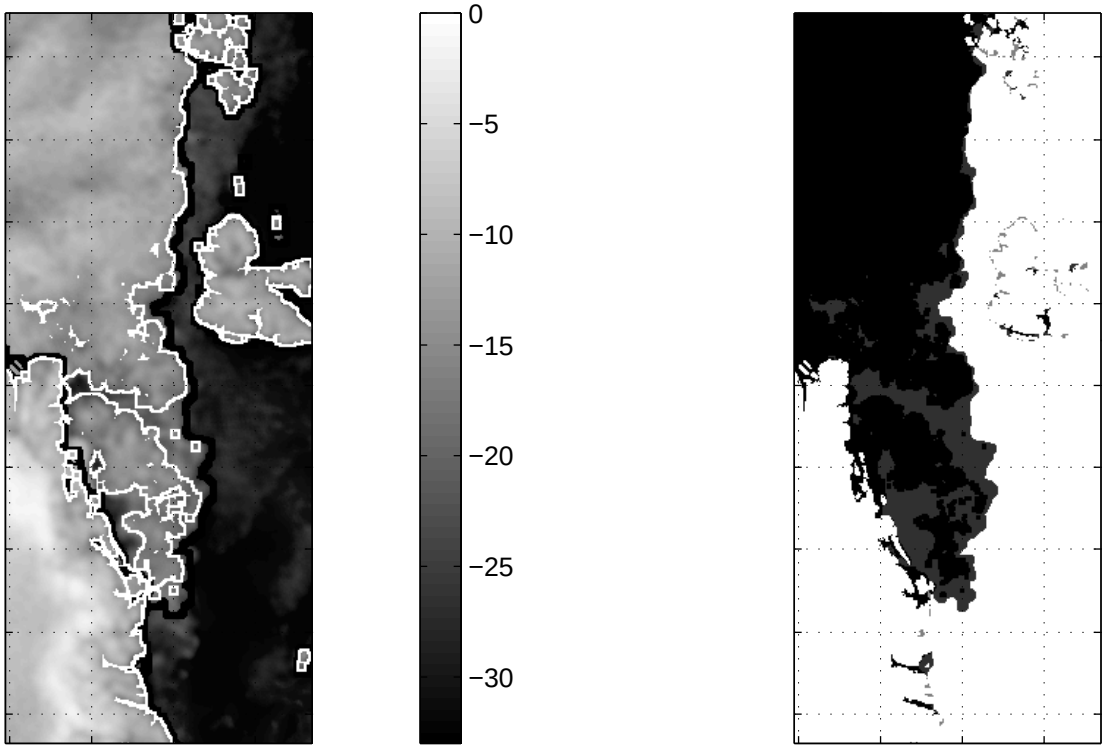

Figure 4.12: Ice edge comparison of modified Bayes (white) and RL (black) algorithms overlayed on A_h imagery (left). The color scale is in dB. The mask comparison (right) shows pixels which are common between the two algorithms (black), pixels unique to the modified Bayes algorithm (light gray), and pixels unique to the RL algorithm (dark gray). Here, surface melting has induced misclassification errors in both algorithms; however, the binary processing phase of the RL algorithm has corrected this misclassification. Shown is JD 88, 2001. The center pixel is at 79.5° N, 0.6° W. Grid spacing is 250 km.

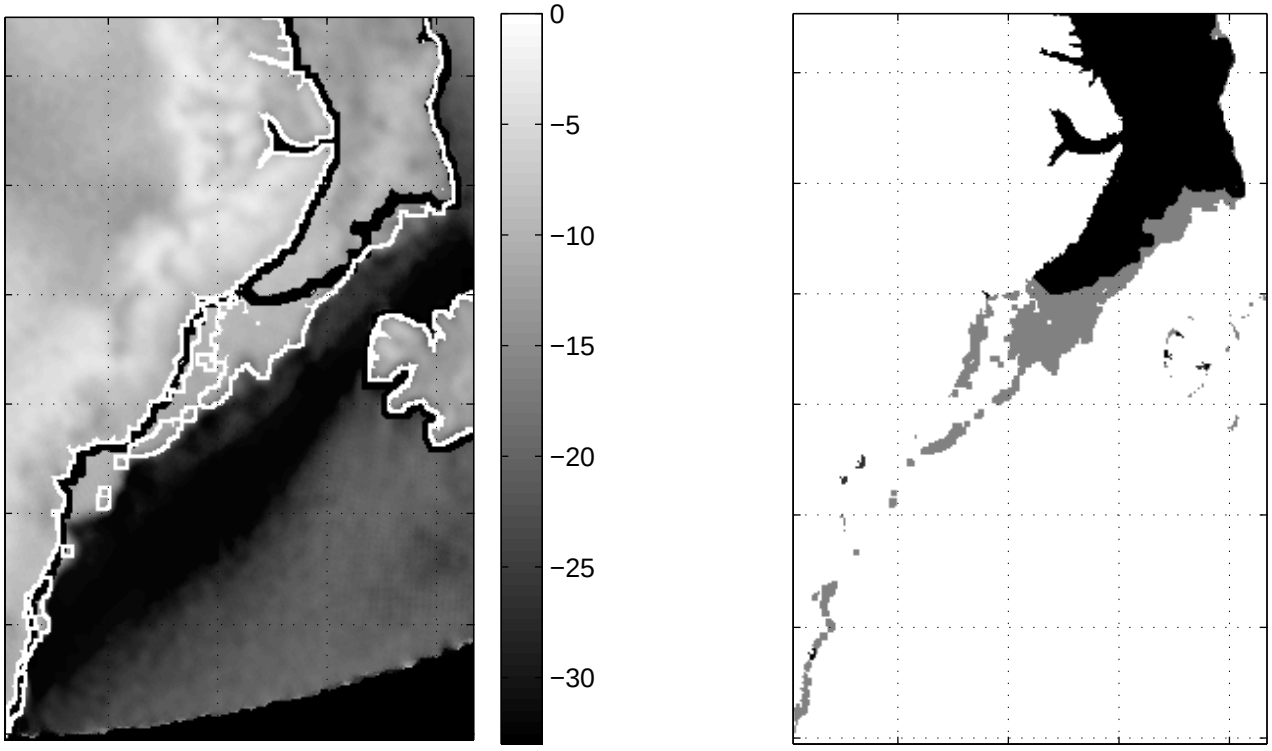

Figure 4.13: Ice edge comparison of modified Bayes (white) and RL (black) algorithms overlayed on A_h imagery (left). The color scale is in dB. The mask comparison (right) shows pixels which are common between the two algorithms (black), pixels unique to the modified Bayes algorithm (light gray), and pixels unique to the RL algorithm (dark gray). Here, the effects of surface melting and sea ice motion in V_v and V_h imagery have induced misclassification errors in both algorithms. Shown is JD 142, 2001. The center pixel is at 66.2° N, 30.7° W. Grid spacing is 250 km.

The new algorithm presents several improvements over the RL algorithm:

1. There is a reduced dependence on post processing steps designed to eliminate spurious classification but also suppress edge features and disjoint ice bodies. The new method provides an unfiltered version of the SeaWinds ice edge, allows for the detection of polynias, and allows the algorithm to track floes, icebergs, and large sections of sea ice which have been separated from the primary ice sheet.

2. The inclusion of spatial and statistical *a priori* information results in more consistent estimates of sea ice extent from day to day.

3. The adaptive statistical model allows for changes in sea ice and ocean properties without severely degrading the algorithm's performance.

These improvements come at a cost. First, unlike the RL algorithm, it is not possible to generate a sea ice extent map without *a priori* information. Thus, a different method must be used to "start" a sequence. Furthermore, the PCs must be calculated (an algorithm training phase) before the algorithm can operate. Secondly, binary processing in the RL algorithm corrects misclassification errors caused by the effects of surface melting on V_h and V_v. This is not corrected, in general, by the new approach, unless the tuning parameters are set in such a way that the effects of V_h and V_v are overcome. This may come at the cost of losing information about polyias. Thirdly, the new method may be adversely affected by poor *a priori* information. This may be ameliorated, however, by adjusting the tuning parameters in the new method, as discussed previously. The ability of the algorithm to recover from poor *a priori* information may be adjusted, but comes with the tradeoff of degraded performance, namely, more spurious misclassification errors, and less consistency between consecutive ice maps in a sequence. The ability to tune the algorithm may be viewed as both a strength and a weakness. Unlike the RL algorithm which is not tunable, but very robust, the new algorithm may be adjusted for desired performance, but may not be as robust for a particular set of tuning parameters.

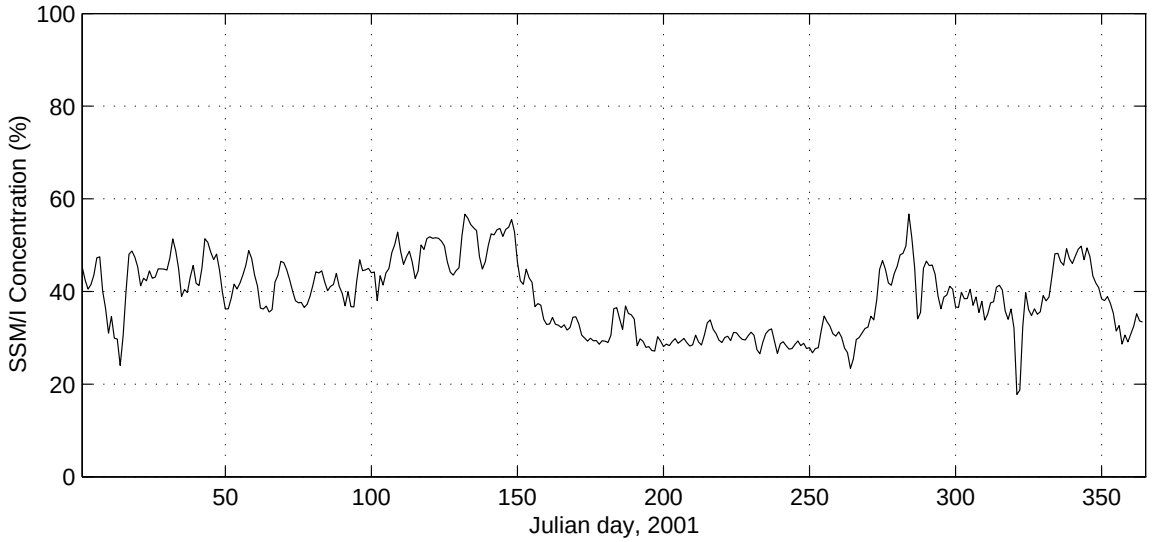

Figure 4.14: Average SSM/I sea ice concentration corresponding to ice edge derived from new SeaWinds ice mapping approach.

4.3.2 Validation: SSM/I NASA Team Sea Ice Concentration

Results from the algorithm are compared to sea ice concentration estimates generated by the SSM/I NASA Team algorithm [17]. The latter are gridded on a polar stereographic projection at 25-km pixel spacing. In order to compare datasets, the SSM/I concentration maps are interpolated onto the 4.45-km spacing of the SIR polar stereographic projection using a nearest neighbor approach. Figure 4.15 shows the SeaWinds ice edge overlayed on SSM/I concentration imagery for both a winter and a summer case.

The average SSM/I sea ice concentration corresponding to the "edge" of the SeaWinds-derived ice extent map is extracted for each day of 2001 for the Arctic region. Ice edge concentration as a function of Julian day is shown in Figure 4.14. The comparison reveals seasonal dependence of the correlation between SSM/I sea ice concentration and the new SeaWinds ice edge, ranging from 30% in the summer to 50% in the winter. The peculiar sinusoidal behavior in the ice edge concentration during the first 150 days of 2001 is possibly due to sea ice growth, differences in sensor imaging times and intervals, and/or resolution and gridding differences in the imagery.

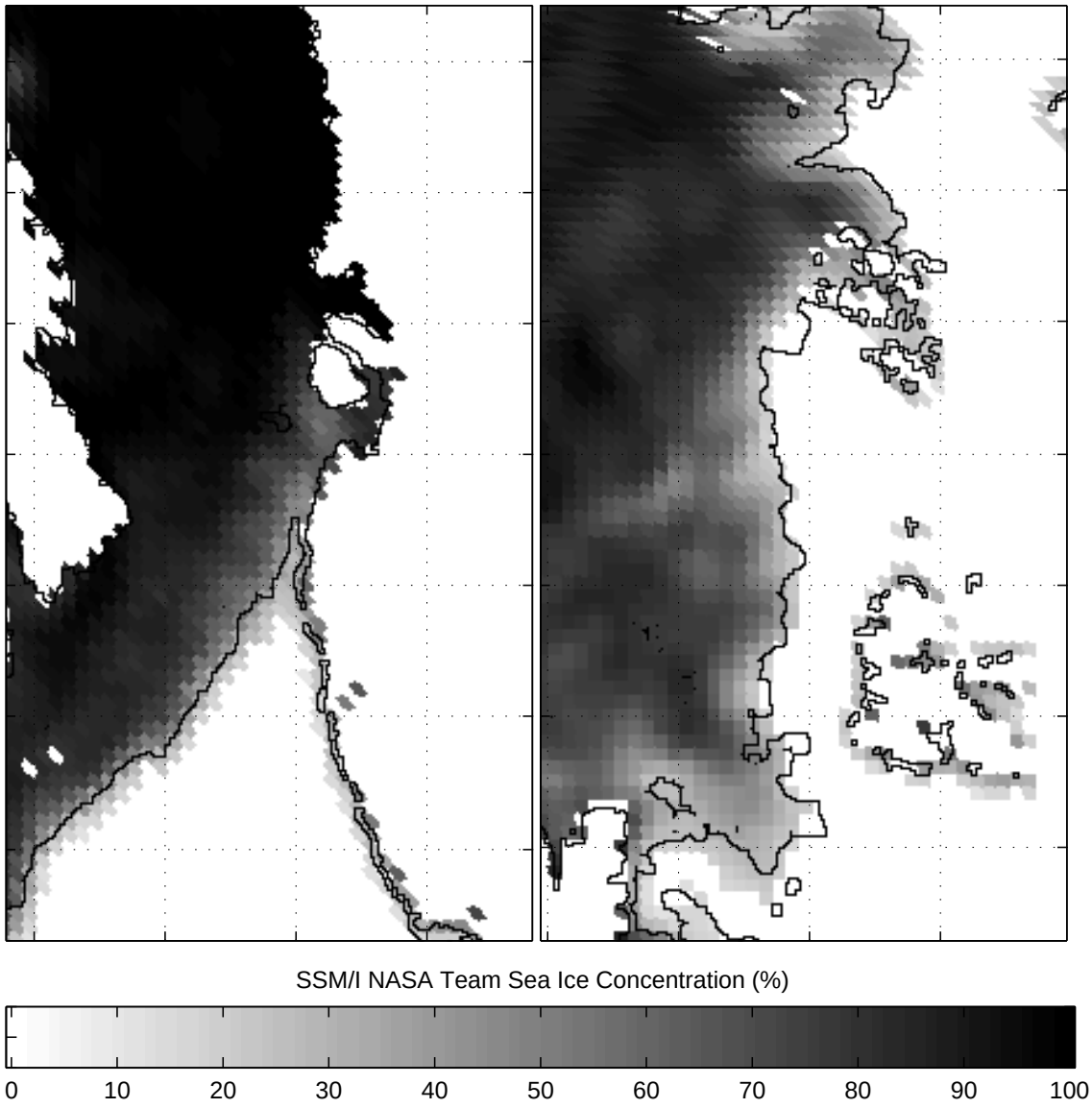

Figure 4.15: Comparison of SeaWinds ice edge (black line) and SSM/I sea ice concentration for the Arctic (left) winter (JD 88) and (right) summer (JD 250). SSM/I concentration contours show consistency with the SeaWinds ice edge. The 0–100% sea ice concentration boundary may be fairly sharp in the winter case, but is blurred by ice/ocean spill-over in the SSM/I footprint pattern. The left image is centered at 67.9° N, 55.8° W; the right image at 82.2° N, 36.2° E. Grid spacing is 250 km.

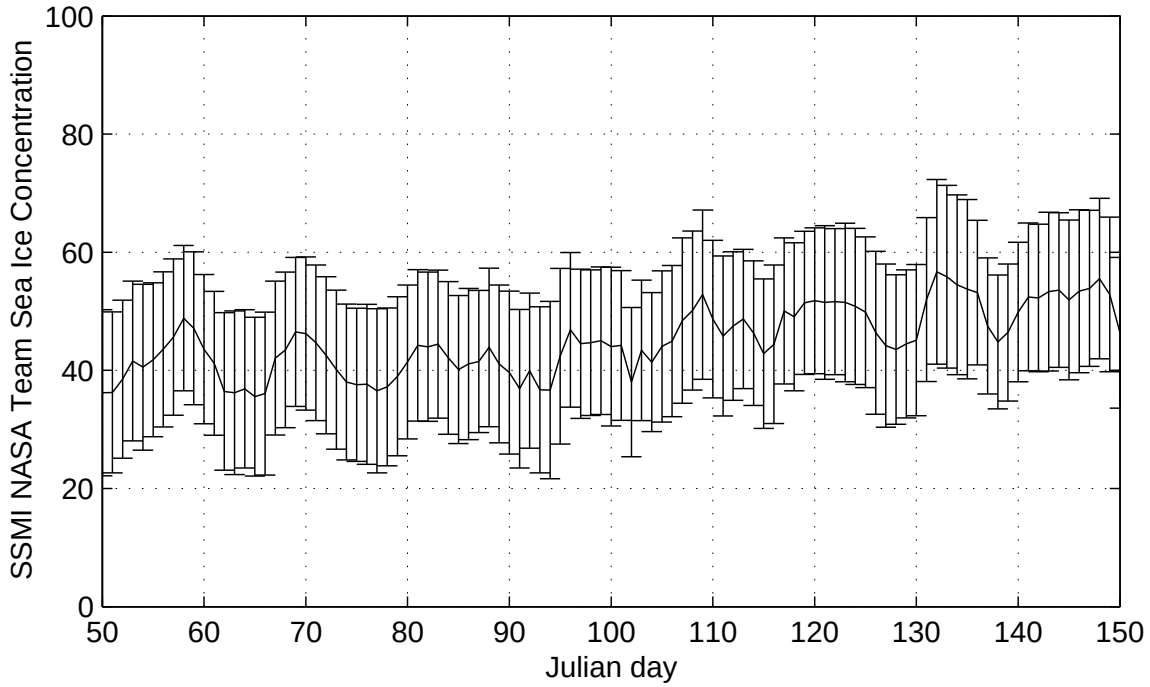

Figure 4.16: Average SSM/I sea ice concentration corresponding to SeaWinds-derived ice edge for JD 50-150, 2001 (winter). Error bar heights are one standard deviation in ice concentration data.

For clarity, two separate segments of the resulting ice edge concentrations are shown in Figure 4.16 for the winter, and Figure 4.17 for the melt season. Figure 4.16 reveals that the winter SeaWinds sea ice edge corresponds to 40–50% sea ice concentration with large variability over the season. However, the variance of the SSM/I concentration at the ice edge for a given day is consistent throughout the season. This suggests that the SeaWinds-reported sea ice edge is consistent, and that the sinusoidal variations are either geophysical, or can be ascribed to the inaccuracy of SSM/I ice concentration readings at crisp ice/ocean edges. In the winter, the ice edge is fairly abrupt, i.e., there may be a sudden change from a high concentration to zero concentration. The SSM/I instrument is sensitive to sea ice which may only partially fill the antenna footprint. This causes the transition between sea ice and ocean to appear more gradual than the true ice edge and the ice edge reported by the higher resolution SeaWinds imagery.

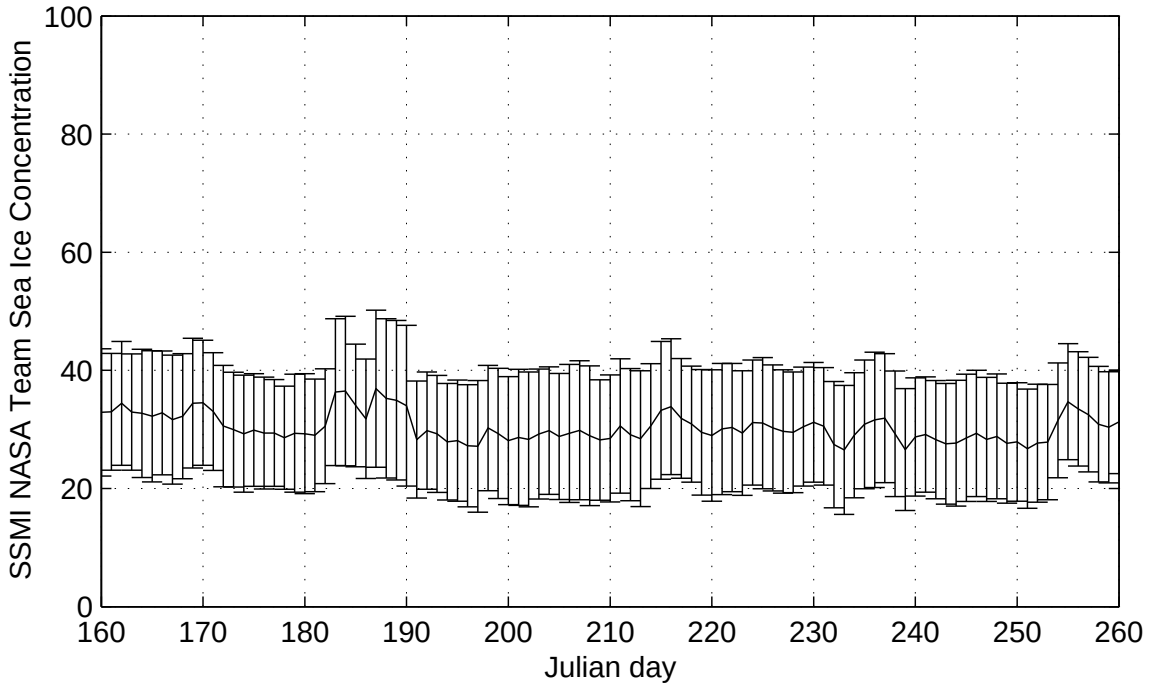

Figure 4.17: Average SSM/I sea ice concentration corresponding to SeaWinds-derived ice edge for JD 160-260, 2001 (summer). Error bar heights are one standard deviation in ice concentration data.

Figure 4.17 reveals that the SeaWinds-reported summer ice edge corresponds to the 30% SSM/I sea ice concentration contour. The consistency and low variation may be ascribed to the more diffuse summer sea ice edge. During the summer, the SSM/I reported sea ice concentration may be more accurate, and thus more valid for a quantitative comparison.

To demonstrate the flexibility of the algorithm, the tuning parameters are adjusted in an effort to produce an ice map that corresponds to a lower SSM/I concentration contour. The number of iterations is increased to 5, `USEVECS` is increased to 49, `LM_ERODE` is reduced to 3, `LOSSFLOOR` is increased to 0.1, α is set to 0.6, and `SI_DILATE` is increased from 3 to 4. The algorithm is not particularly sensitive to the exact values of these parameters, which are somewhat arbitrary. However, `MAXGROW` is given a value of 10 for the ocean loss map, but a value of –5 (erosion rather than dilation of the ocean mask) for the ice loss map. In effect, this creates a region of ignorance 5 pixels (22.25 km) wide that is offset by 5 pixels from the original ice edge.

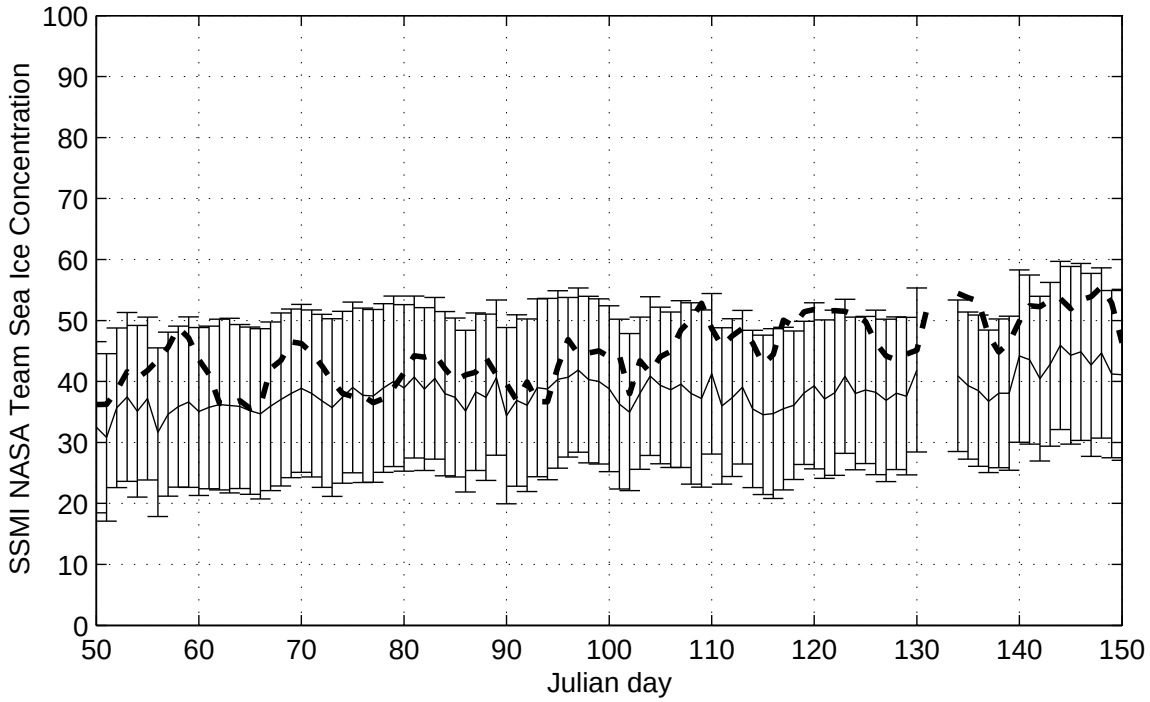

Figure 4.18: Average SSM/I sea ice concentration corresponding to SeaWinds-derived ice edge (tuned version) for JD 50-150, 2001 (winter). Error bar heights are one standard deviation in ice concentration data. The previously computed concentration is plotted (dashed line) for reference.

This influences the algorithm to create ice maps which are overestimates of the nominal output. The choice of 5 pixels is somewhat arbitrary—it is based on expected ice growth, and chosen to offset to affects of sea ice motion on V_v and V_h—and does not guarantee that the output will merely be the original output dilated by 5 pixels. Rather, it produces a region of influence 5 pixels wide around the original ice edge in which sea ice is more likely to be chosen by the classifier than ocean. (This is akin to the reclassification approach outlined in Appendix C.)

Figure 4.18 shows the newly computed average SSM/I sea ice concentration for the winter period. The new ice edge concentration is less sporadic than the previously computed ice edge, and exhibits values which correspond more closely to 30–40% concentration rather than 40–50% concentration. The concentration for the summer shown in Figure 4.19, however, is slightly more sporadic, but still correlates well with the 30% sea ice edge. This is a result of surface melting events, to which the

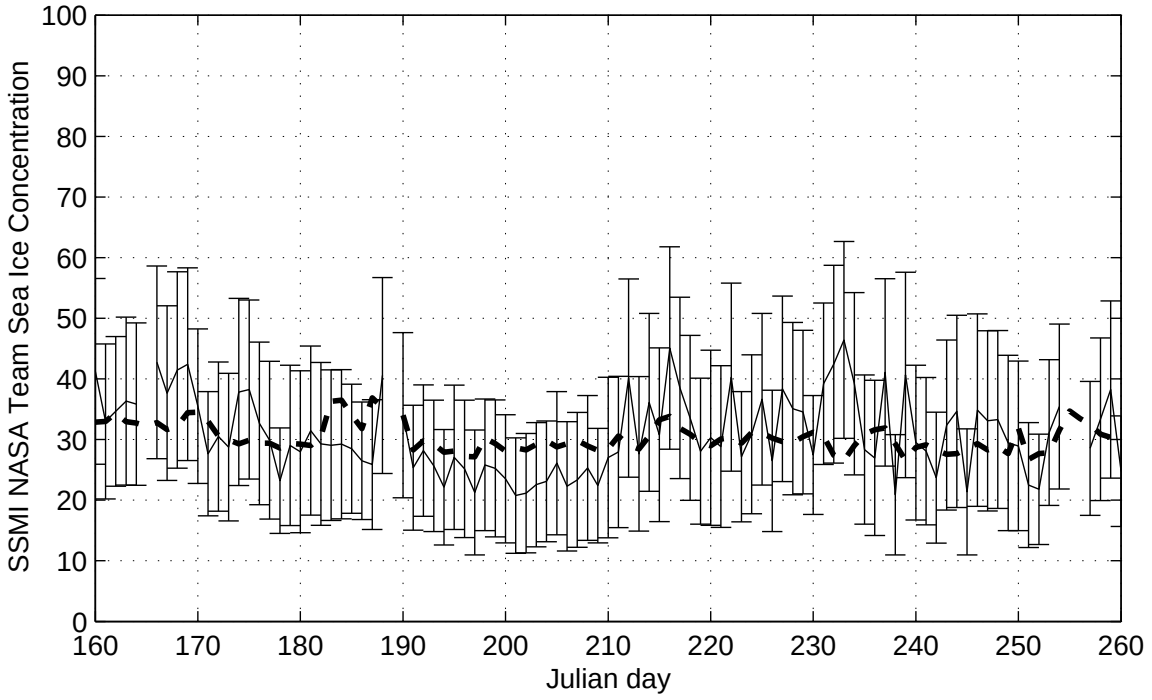

Figure 4.19: Average SSM/I sea ice concentration corresponding to SeaWinds-derived ice edge (tuned version) for JD 160-260, 2001 (summer). Error bar heights are one standard deviation in ice concentration data. The previously computed concentration is plotted (dashed line) for reference.

radiometer is insensitive relative to the scatterometer. The tuning parameters may be modified to some extent to match lower ice edge concentration values, but ultimately, the characteristics of the discrimination parameters govern how the algorithm performs—the algorithm is robust.

4.3.3 Validation: RadarSat ScanSAR

Results from the algorithm are compared to RadarSat ScanSAR imagery for qualitative visual comparison. Comparison with the high-resolution data is difficult for two reasons. First, because of the low-coverage nature of SAR, usable RadarSat images at the ice edge are difficult to obtain. Furthermore, the images are difficult to compare. RadarSat imagery is a "snap-shot" of the ice edge at a particular time of day, while SeaWinds imagery is obtained over a 24-hour period. Especially during rapid ice growth or retreat, the perceived ice edge may appear to be inconsistent

with reported data. Instruments, such as SeaWinds, which enjoy greater coverage also suffer from blurring caused by sea ice motion during several satellite passes—hence, the reported sea ice edge is the "average" sea ice edge during the imaging interval. Nonetheless, RadarSat imagery is as close to high-detail *in situ* data as one can expect. This comparison provides a qualitative check that the reported sea ice edge is consistent with the shape and features of the "true" ice edge (as represented by the RadarSat ScanSAR snapshot).

Figure 4.20 shows a RadarSat ScanSAR mosaic for JD 12, 2001. During the winter, ice growth is expected, and is especially evident at the bottom of the image, where small fingers of sea ice are forming along the peninsula. Motion stress on the ice pack are apparent by the small cracks and fissures within the ice sheet. The ice edge derived from the new ice mapping approach is shown, as well as the RL-derived ice edge, the SSM/I NASA Team 30% contour, and the SSM/I NASA Team 10% contour. Here, the spill-over effects of the ice edge into the SSM/I antenna footprint over ocean is evidenced by the displaced 10% contour. The new SeaWinds ice edge and the RL-derived ice edge appear to underestimate the true ice edge—perhaps an effect of sea ice growth. The SSM/I 30% provides a fairly consistent estimate of the RadarSat ice edge, albeit at a coarse resolution.

Figure 4.21 shows a similar RadarSat mosaic with overlayed sea ice edge estimates. The mosaic was imaged during the melt season, as evidenced by the separated floes within the ice pack and the diffuse edge at the bottom of the image. However, the ice edge appears fairly abrupt at the top of the image. The new SeaWinds edge and the RL-derived edge show excellent correlation with the RadarSat ice edge. The 30% SSM/I contour also shows good correlation.

Figure 4.22 shows a RadarSat mosaic of a large polynia located off the northwest coast of Greenland. At the bottom-right of the image, the sea ice edge is somewhat diffuse. The SSM/I contours appears to be valid representations of the diffuse edge. The RL-derived ice edge shows excellent tracking of the diffuse edge, while the new SeaWinds edge follows the SSM/I 30% contour in the diffuse area. Both SeaWinds edges are good representations of the crisp RadarSat ice edge at the top

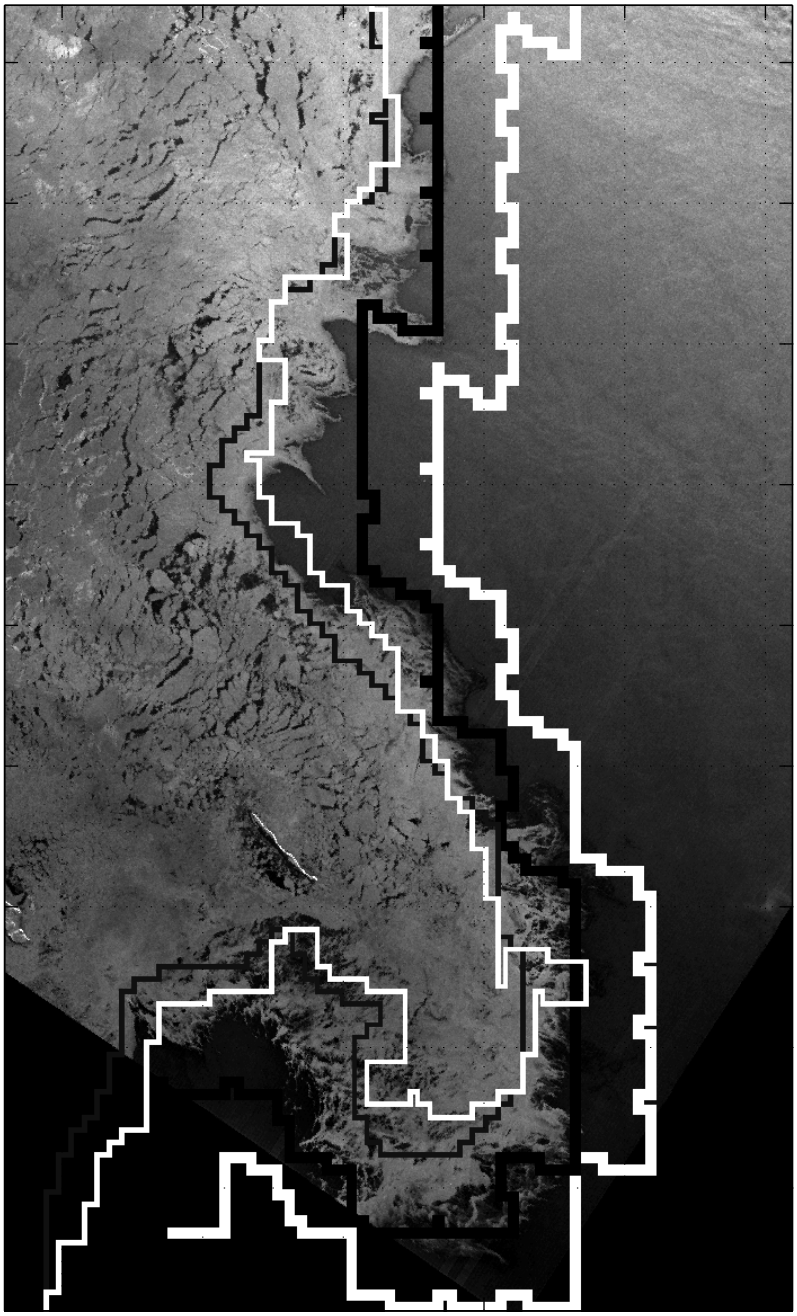

Figure 4.20: RadarSat ScanSAR (uncalibrated) mosaic for JD 12, 2001 east of Svalbard. The SSM/I 30% contour (thick black) is fairly consistent with the true edge, albeit at a coarse resolution. The SSM/I 10% contour (thick white) is shown for comparison. The modified Bayes (thin white) and RL (thin gray) ice edges appear to be underestimates of the true ice extent. This may be partially due to sea ice growth and the difference in imaging times between SeaWinds and RadarSat. The center pixel is at 76.9° N, 29.2° E; grid spacing is 50 km. (RadarSat data ©2001, Canadian Space Agency.)

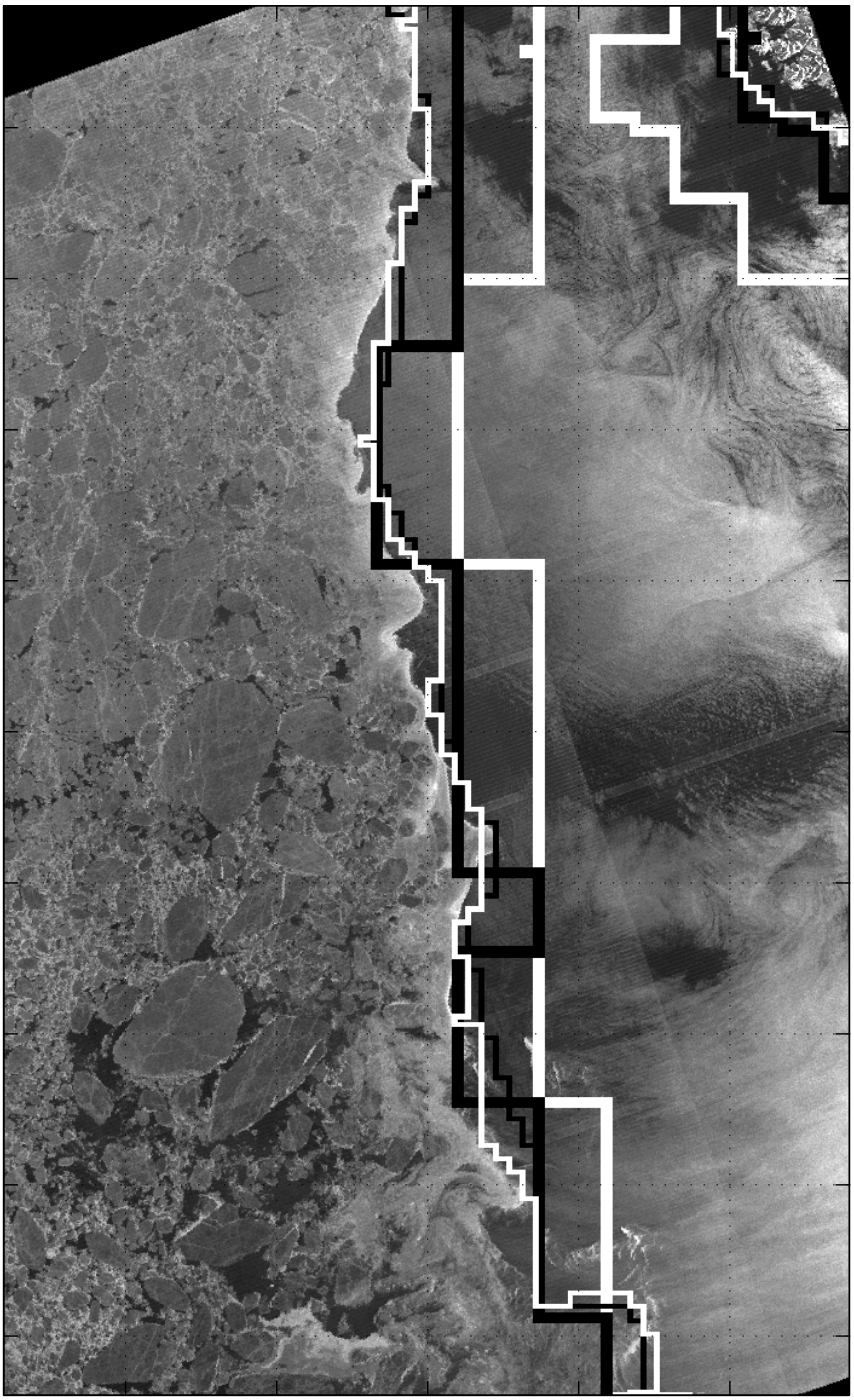

Figure 4.21: RadarSat ScanSAR (uncalibrated) mosaic for JD 168, 2001, NE of Greenland. The SSM/I 30% contour (thick black), modified Bayes (thin white), and the RL-derived (thin black) ice edges are consistent with the observed RadarSat ice edge. The SSM/I 10% contour (thick white) is shown for comparison. The center pixel is at 79.2° N, 4.8° W; grid spacing is 50 km. (RadarSat data ©2001, Canadian Space Agency.)

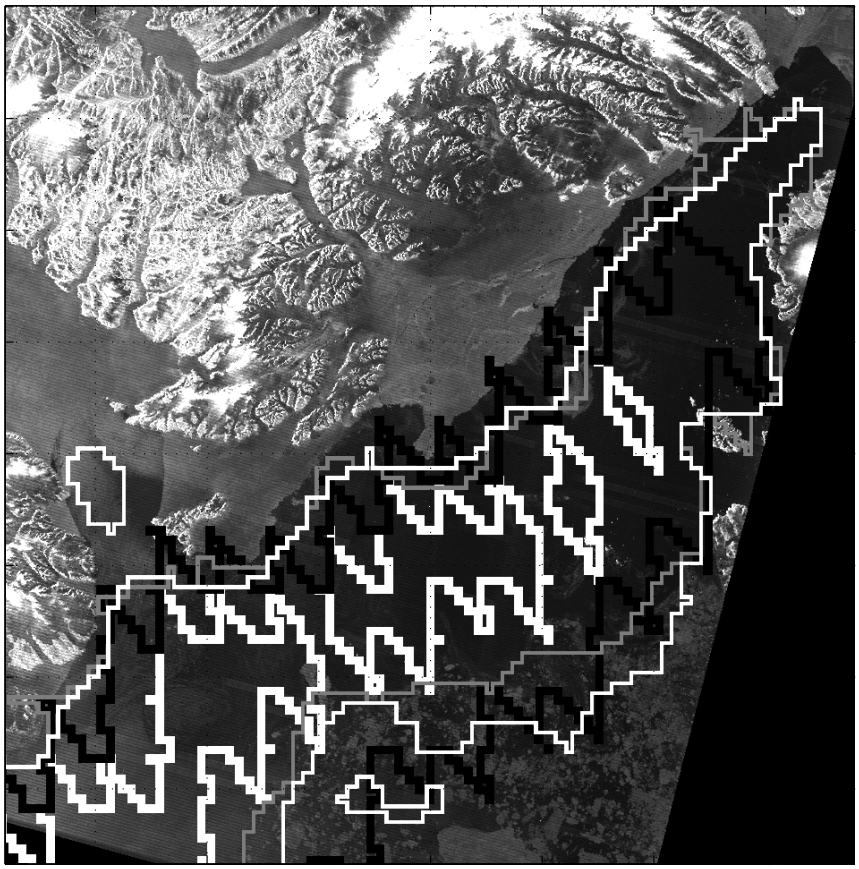

Figure 4.22: RadarSat ScanSAR (uncalibrated) mosaic for JD 169, 2001 showing a polynia just off the NW coast of Greenland. The SSM/I 30% contour (thick black) provides coarse detail of the polynia; the RL algorithm (thin gray) higher detail; the new method (thin white) identifies smaller polynias (not geolocated) to the NW and SE. Each provides different variations of the diffuse ice edge at the bottom-right of the image. The SSM/I 10% contour (thick white) is shown for comparison. The center pixel is at 77.1° N, 73.2° W; grid spacing is 50 km. (RadarSat data ©2001, Canadian Space Agency.)

of the image. The new method detects smaller sections of open water—although not geolocated in this image—which are disjoint from the large polynia.

Generally, sea ice maps derived from the new method correlate well with RL sea ice maps, the SSM/I NASA Team 30% contour, and subjectively to RadarSat data. (For SSM/I sea ice concentration data, the 30% contour shows the best correlation with the observed RadarSat ice edges in the previous examples.) The new SeaWinds edge shows detail limited only by the resolution of the SeaWinds egg imagery, including small polynias within the ice sheet.

4.4 Conclusions

The RL algorithm for SeaWinds is another manifestation of the utility of Ku-band scatterometer data in polar sea ice detection. In an effort to reduce the dependence on binary processing routines, improve statistical modeling, and incorporate spatial and statistical *a priori* information, a new sea ice mapping algorithm for SeaWinds has been developed. A sample image of the algorithm applied to SIR egg imagery is shown in Figure 4.23.

The new technique shows high correlation with the RL algorithm, but exhibits several improvements. First, the algorithm produces ice maps at the effective resolution of the SIR imagery, but has few misclassification errors. This reduces the need for a binary processing phase. The independence from binary processing routines allows the algorithm to track sea ice bodies that are disjoint from the primary ice sheet. Secondly, the inclusion of spatial and statistical *a priori* information provides for more consistent sea ice extent maps from day to day. Also, the more sophisticated statistical modeling approach facilitates the dynamic nature of polar sea ice and ocean microwave signatures.

The resulting sea ice maps show high correlation with estimates from other sensors. In particular, the new SeaWinds ice edge corresponds to the 30% SSM/I NASA Team sea ice concentration contour. RadarSat ScanSAR imagery verifies the accuracy of the algorithm.

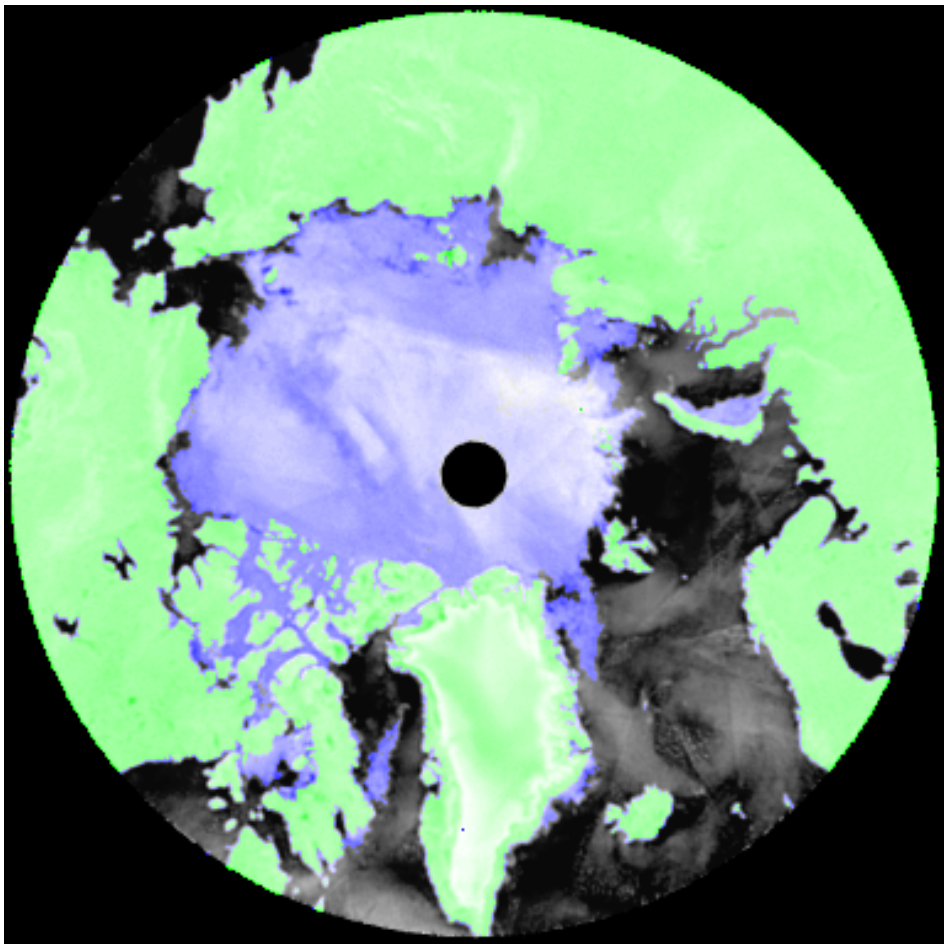

Figure 4.23: Sea ice extent (blue) highlighted in SIR egg imagery. Land is shown in green. The image mosaic is created from data collected JD 206, 2001.

Although the algorithm presented in this chapter is designed for the SeaWinds scatterometer, it may be adapted for other instruments. This can be accomplished by changing the discrimination parameters and/or *a priori* information. For example, the algorithm could be "trained" with the SSM/I NASA Team 15% contour ice edge, so that the SeaWinds ice edge corresponded more closely to 15% sea ice concentration. Or, the discrimination parameters could be changed to allow for multi-sensor classification, such as to provide joint radiometer and scatterometer sea ice maps, benefiting from the advantages of both types of microwave sensors. The binary classification approach may also be extended to M-ary classification, such as ice type classification. These topics are left for future research.

Chapter 5

Conclusion

Polar sea ice extent is a sensitive indicator of long- and short-term climate change. As discussed in Chapter 1, microwave remote sensing provides a good method for polar sea ice remote sensing. The SeaWinds instrument in particular, provides data which exhibit a good trade-off between spatial coverage (temporal resolution) and spatial resolution. Chapter 2 contains valuable background information about the SeaWinds instrument and its utility in sea ice mapping by the RL algorithm, as well as a broad introduction to active and passive microwave remote sensing in general. Chapter 2 chapter also includes a detailed explanation of the RL algorithm for SeaWinds.

In Chapter 3, and analysis of the RL algorithm was performed. It was found that seasonal non-Gaussian characteristics of polar sea ice caused misclassification errors and in some cases, led to algorithm divergence. In particular, marginal distributions of V_v and V_h for Antarctic sea ice during the melt season exhibited non-Gaussian shapes, suggestive of Chi-square distributions. For the Antarctic, marginal distributions of each of the discrimination parameters for polar sea ice were leptokurtic. The RL algorithm did not diverge for the Arctic region. However, the Gaussian model is a sub-optimal fit for the bimodal nature of Arctic sea ice during the boreal winter. Several modifications were made to the RL algorithm to prevent divergence and to improve binary processing techniques.

Chapter 4 contains the development of an improved algorithm based on Bayes detection. Sea ice maps produced by the algorithm correspond well to the RL algorithm, to SSM/I NASA Team algorithm 30% ice concentration contours, and are

consistent with RadarSat imagery. Sea ice maps produced by the new algorithm are suitable for use in sea ice studies and wind retrieval.

5.1 Contributions

This thesis presents several contributions to the remote sensing community. These contributions are briefly summarized here.

5.1.1 Modifications to the RL Algorithm

First, several contributions were made to the RL algorithm for SeaWinds, as outlined in Chapter 3. Specifically,

1. This study provides the first in-depth analysis of the RL algorithm for SeaWinds. First, it was found the algorithm diverges under certain conditions. The study showed that seasonal non-Gaussian characteristics of polar sea ice are a principal cause of misclassification errors and algorithm divergence. This study also includes a modeling analysis, in which it was found that Gaussian assumption of the RL algorithm is severely violated for the austral summer, and a sub-optimal fit for bimodal Arctic sea ice distributions.

2. The number of iterations used by the RL algorithm was modified to avoid algorithm divergence. The number of iterations selected is a function of the Julian day (season).

3. The sea ice growth/constraint feature in the binary processing phase of the RL algorithm was modified to allow for uncertainty in the accuracy of the previous day's ice map. The modification allows the algorithm to recover from poor constraint information. This reduces the need for user intervention in producing accurate sea ice extent maps.

The modifications to the RL algorithm improve the performance of the algorithm. These modifications have been implemented in operational code used by NASA's JPL for near real-time wind retrieval, and at NOAA for near real-time polar sea ice studies.

5.1.2 Improved Sea Ice Mapping Algorithm

The second primary topic addressed in this thesis is the development of the new Bayes detection algorithm in Chapter 4. This work has been submitted to the journal *IEEE Transactions on Geoscience and Remote Sensing*. The new method presents several contributions to the remote sensing community.

1. An iterative algorithm based on Bayes decision theory is developed, in which statistical *a priori* information is incorporated in the statistical model, and spatial *a priori* information is incorporated through a novel use of Bayes loss.

2. A new approach for statistical modeling is introduced, in which the principal components of an ensemble of empirical distributions (histograms) are used to parameterize sea ice and ocean distributions. Newly computed histograms that are parameterized by the truncated PC basis conform to the shape of expected distributions, i.e., the PCs function as a filter on new histograms. Reconstructed histograms are used for binary Bayes detection.

3. The notion of loss maps is developed, in which the Bayes loss is a function of position. Loss maps are related to the ice extent map from a previous day. Loss maps for sea ice and ocean are generated and updated with new classification data from each iteration. The concepts "default decision rule" and "region of ignorance" are also introduced in connection with position-conformal loss maps. A spatial inclusion step is also introduced, which aids in the algorithm's ability to recover from poor *a priori* information, and promotes spatial homogeneity of the sea ice classification.

4. The algorithm's independence from binary processing routines allow for sea ice maps which show detail at the same level of resolution as the enhanced SIR imagery. This independence also allows the algorithm to detect polynias, and track icebergs and floes which are disjoint from the primary ice sheet.

5.2 Future Research

Several lines of research may be pursued in conjunction with this work. Some of these topics have been pursued by the author to a limited degree, but are beyond the scope of this thesis. Several areas of possible future research are discussed in the following sections.

5.2.1 High-Resolution and Near Real-Time Sea Ice Maps

The next logical step for continued research is to apply the new Bayes algorithm to the higher resolution "slice" imagery for the Arctic and Antarctic regions. This would consist of (1) calculating a truncated PC basis set for sea ice and ocean histograms, (2) adjusting the algorithm's tuning parameters for optimal performance, and (3) implementing mild binary processing routines to filter sea ice maps generated from the inherently more noisy data. A suggested binary processing phase would include temporal and/or spatial non-causal median filtering (to preserve edges), and a region growing routine to eliminate non-speckle noise. (An interesting idea for region growing is to implement a segmenting scheme which not only accounts for spatial homogeneity, but also temporal consistency). Success in this study would result in high-resolution sea ice maps which maintain the fine edge detail lost in the RL algorithm's binary processing phase for slice data.

Once the algorithm has been tuned for slice data, it may be further tuned for NRT data, and eventually replace the operational code at JPL and NOAA.

5.2.2 Joint SeaWinds-QuikScat Sea Ice Detection

The SeaWinds instrument aboard ADEOS-II was launched in December of 2002, but at the time of printing of this thesis, only sample images were available. The SeaWinds scatterometer will soon be calibrated to the SeaWinds scatterometer aboard QSCAT and daily provide full coverage of the polar regions.

The orbits of the ADEOS-II and QuikScat platforms are such that it is possible to retrieve images of the polar regions over a six-hour imaging interval rather than the 24 hours currently required. This provides several advantages. First, sea ice

motion during the six-hour interval is significantly less than the 24-hour interval. Sea ice motion constraints may be applied for sea ice detection. The use of *a priori* information is more applicable. Modified versions of the RL algorithm or the new Bayes detection algorithm using six-hour imagery would benefit from the fact that variance parameters, V_h and V_v, would have smaller values at the ice edge due to sea ice motion, allowing for more accurate classification of the ice edge.

5.2.3 Sea Ice Motion

The Bayes detection algorithm in this thesis provides finer edge detail than the RL algorithm, and also makes possible the tracking of polynias and sea ice bodies that are disjoint from the primary ice sheet. These features are smoothed or excluded in the RL algorithm. This study would be particularly useful with joint-SeaWinds classification maps, which would have fine temporal resolution. Sea ice motion may be particularly interesting if studied in conjunction with near-surface winds adjacent to the ice sheet. Knowledge of sea ice motion is important as an indirect indicator of ocean currents.

5.2.4 Ice Type Classification

A knowledge of sea ice extent also allows for ice type classification. A modified Bayes detection algorithm may be suitable to classify multiple sea ice types within the ice pack. Multi-year ice, rough and smooth first-year ice, fast ice, gray ice, icebergs, etc. exhibit differences in their respective microwave signatures. Their statistical distributions may be captured empirically and incorporated in the algorithm presented in this thesis. A similar classification could be implemented to detect surface melt events, which are good indicators of short-term climate change.

In addition to ice type classification, the ice mask could be used to detect polynias and leads, which are crucial in heat exchange, and to correct misclassifications. This may be best accomplished by segmenting the ice mask into subsections, and reclassifying on a local level so that region-specific statistics are not drowned by ensemble statistics. A simple local-reclassification method to correct misclassification

errors induced by anomalies in the V_h and V_v parameters (surface melt and persistent ocean storms) is discussed in Appendix C.

5.2.5 Sea Ice Depth and Concentration

While sea ice depth and concentration may be difficult to measure directly from scatterometer data, it may be inferred from other means. The age of sea is can be inferred from scatterometer data due to volume and surface scattering differences between old and new sea ice—a function of snow build-up, salt content, texture, concentration, etc. Sea ice age may be used to infer depth or concentration indirectly. Although comparisons between the SeaWinds sea ice edge and SSM/I NASA Team sea ice concentration data affirmed that there is correlation between the 30% ice concentration contour and the SeaWinds edge, other concentrations sea ice concentrations may be retrievable. Indeed, a study has shown correlation between sea ice concentration and PR, as mentioned in Appendix C.

5.2.6 Multi-Sensor Classification

The algorithm in this thesis could easily be modified for multi-sensor classification. A multi-sensor sea ice classification scheme was developed by Remund, et al., for NSCAT, ERS-2, and SSM/I data [15]. The new algorithm may be modified for M-ary detection, and easily facilitates training from different sensors. The fusion of data from passive and active microwave remote sensing instruments may allow for more accurate detection of various sea ice types, leads, and polynias. Passive microwave instruments are more sensitive to leads and polynias than active instruments, while active instruments are more sensitive to surface features.

Appendix A

Principal Components

This appendix is intended to be a review of principal components and a supplement to help in implementing principal component methods. Included is a review of the Karhunen-Loeve expansion (highlighting low-rank approximation), principal component methods, and a method for updating basis vectors "on-the-fly", as proposed by Levy and Lindenbaum [26].

A.1 Karhunen-Loeve Expansion and Low-Rank Approximation

The Karhunen-Loeve (KL) expansion of a zero-mean $m \times 1$ random vector, $\mathbf{x}$, may be computed by diagonalizing the matrix $R = E[\mathbf{x}\mathbf{x}^H]$, which is $m \times m$ and sparse. The square covariance matrix R is diagonalizable via eigen-decomposition,

$$R = U\Lambda U^H \tag{A.1}$$

If the vector $\mathbf{x}$ is is projected onto the orthonormal columns of U, $\mathbf{y} = U^H\mathbf{x}$, then $\mathbf{y}$ becomes a zero-mean random vector with uncorrelated components:

$$E[\mathbf{y}\mathbf{y}^H] = \Lambda. \tag{A.2}$$

For this reason, U is often referred to as a "whitening filter" [27].

Note that $\mathbf{x}$ may be expressed in terms of $\mathbf{y}$ as

$$\mathbf{x} = UU^H\mathbf{x} = U\mathbf{y} = \sum_{i=1}^{m} \mathbf{u}_i y_i, \tag{A.3}$$

where $\mathbf{u}_i$ are columns of U. This representation of $\mathbf{x}$ is the KL expansion of $\mathbf{x}$. The transform $\mathbf{y} = U^H\mathbf{x}$ represents an axial rotation of $\mathbf{x}$ onto U, the eigenvectors of R.

This rotation provides a representation for the data which in which it is aligned with the axes covariance. This also allows for a low-rank approximation of the vector $\mathbf{x}$. If U and Λ are ordered in such a way that Λ contains eigenvalues which decrease in magnitude with increasing column number, a low rank approximation of $\mathbf{x}$ may be written as

$$\hat{\mathbf{x}} = \sum_{i=1}^{k} \mathbf{u}_i y_i = K\mathbf{x} \tag{A.4}$$

where $k < m$, and K is an $m \times m$ matrix of rank $k < m$. The vector $\hat{\mathbf{x}}$ represents the best low-rank approximation of $\mathbf{x}$ by a low-rank matrix in a minimum mean-squared error sense.

A.2 Principal Components

Principal component (PC) methods are a way to extracting components of a data ensemble which account for the largest portion of the variance in the data. Let X be an $m \times n$ matrix, $m > n$, which contains n data sequences which are of length m, and are usually similar in content, e.g., images of faces, speech segments, etc. The ith principal component of the data is a linear combination of the columns of X and accounts for the ith largest portion of the variance between the data sequences. In other words, the first PC accounts for most of the variance in the ensemble of data sequences, the second PC accounts for the majority of the variance not accounted for by the 1st PC, and so on.

The PCs of an ensemble of data sequences may be computed by diagonalizing the sample covariance inner product $R = X^H X$ (note the distinction between this approach and KL expansion), or equivalently by singular value decomposition (SVD), $X = U\Sigma V^H$, which is usually computed for only the first n vectors of U, which are the PCs of X.

As with the KL expansion, the PCs of a data sequence ensemble provide the "best" decomposition of the data sequence for compaction, and hence reconstruction. It provides the optimal subspace, spanned by the PC basis, which minimizes the mean square error between the given set of vectors and their approximation by a lower-dimensional subspace.

A.3 Sequential KL Transform

KL expansion or PC methods may be inappropriate for a particular application for several reason. First, many important applications exist where the data matrix X is updated from time to time, and a new PC basis set must be recomputed with the updated ensemble. Or, the dataset may be too large to efficiently compute the SVD. Both of these cases have been met in this thesis work, where both computational complexity and memory requirements for extracting the PC basis from a large ensemble of histograms is prohibitive using standard batch, SVD or eigendecomposition based, KL algorithms. (In the case of ice and ocean histograms, the PCs of an ensemble of $N = 355$ histograms of length $M = 30^4 = 810000$—for four dimensions—are extracted. Calculating the KL basis for N histograms of size M requires roughly $O(MN^2)$ operations, and requires $O(MN)$ memory units.)

Algorithms such as that presented by Rosebourough and Murase [28] achieve greater storage and computational efficiency by effectively low-pass filtering image data. This is not desirable in our application. Levy and Lindenbaum [26], however, presented a *Sequential Karhunen-Loeve algorithm* (SKL) which updates the PC basis on the fly. It is not required to store the entire set of input images before proceeding to calculate the PC basis. Rather, it updates an internal representation of the PC basis by taking images one at a time (or in small groups). In this way, both computational and storage requirements are reduced significantly for $M \gg N$, in contrast to ensemble (batch) methods. The proposed memory requirement for storing K significant vectors is $O(MK)$ memory units at a computational cost of $O(MNK)$.

In this section, the SKL algorithm is summarized.

A.3.1 R-SVD

The discrete PC low dimension approximation problem is generally solved using one of two broad methods. A data set of N vectors or images of length M are used to compose an ensemble matrix A ($M \times N$), whose columns contain the input images. The PC basis may be calculated by finding the eigenvalues and eigenvectors of the correlation matrix $R = A^T A$ (or indirectly by converting the eigenvectors of

$\bar{R} = AA^T$ to the eigenvectors of R, as shown in [28]), or by using singular value decomposition (SVD).

A variation of the SVD algorithm, denoted R-SVD [29] is efficient when $M \gg N$, as in our application. It can be computed as follows.

1. Compute the QR decomposition of $A = QR$ where Q is a column-orthonormal $M \times N$ matrix and R is $N \times N$ upper triangular matrix. This can be efficiently computed using the Gram-Schmidt process.
2. Compute the SVD of R, $R = U'\Sigma V^T$.
3. Calculate $U = QU'$.

These matrices correspond to $A = U\Sigma V^T$, the SVD of A. The total computational complexity of the R-SVD algorithm is $6MN^2 + O(N^3)$ [26].

A.3.2 SVD Partitioning and Updating

The SKL is based on partitioning the SVD of a large matrix. Let $B = U\Sigma V^T$ be the SVD of a matrix B. Calculating the SVD of a larger matrix $B^* = (B|E)$, where E is an $M \times P$ matrix containing of P additional column-scanned images, can be done as follows.

1. Orthonormalize the matrix $(U \mid E)$ (Gram-Schmidt process) to yield the matrix with orthonormal columns, $U' = (U \mid \tilde{E})$.
2. Let $V' = \left(\begin{array}{c|c} V & 0 \\ \hline 0 & I_P \end{array}\right)$, where I_P is the P dimensional identity matrix.
3. Let $\Sigma' = U'^T B^* V'$.
4. Calculate the SVD of $\Sigma' = \tilde{U}\tilde{\Sigma}\tilde{V}^T$.
5. Now, the SVD of the larger matrix B^* can be written as

$$B^* = U'\left(\tilde{U}\tilde{\Sigma}\tilde{V}^T\right)V'^T = \left(U'\tilde{U}\right)\tilde{\Sigma}\left(\tilde{V}^T V'^T\right) \tag{A.5}$$

In calculating the SVD of the larger matrix B^*, it is required only to calculate U', V', and D' and the SVD of the small matrix D'.

A.3.3 SKL Algorithm

The heart of the SKL algorithm is based on updating the SVD of a large data matrix by appending blocks of column vectors (images) to the orthonormal basis. The algorithm is initialized by calculating the SVD of the first block. For every new block, column vectors are appended and the SVD is updated using the partitioning R-SVD method described in Section A.3.2. Since we are only interested in the most significant vectors of the SVD for the PC basis, the algorithm deletes basis vectors corresponding to insignificant singular values. In this way, the number of basis vectors that are stored may be limited.

The SKL also provides a way in which the basis set can be continually updated by new histograms. Levy and Lindenbaum introduced a "forgetting factor" coefficient, which can reduce the contribution of previous blocks. This allows us to approximate recent images more accurately. The forgetting factor, however, is not explored in this work, but is suggested as a topic for future research.

Levy and Lindenbaum [26] reported that the SKL algorithm captures more than 99%, and in most cases close to 99.99%, of the energy content of the standard KL approximation. It is with this motivation that the SKL is used for parameterizing empirical distributions from a basis set created by past "trusted" histograms of ocean and polar sea ice.

Appendix B

Binary Processing Methods

The Remund-Long (RL) algorithm relies on a binary processing phase to filter residual misclassification errors. This appendix reviews RL binary processing routines and suggests alternative methods for greater efficiency. Some of the alternative methods have either been implemented as a change in the RL algorithm as discussed in Chapter 3, or are incorporated into the new algorithm (dilation and erosion) outlined in Chapter 4. This appendix was originally an internal report for the Brigham Young University (BYU) Microwave Earth Remote Sensing (MERS) Laboratory.

B.1 Introduction

The Remund-Long (RL) ice extent algorithm for QuikSCAT employs a set of binary processing techniques to extract, smooth, and constrain the perceived ice extent from an initial classification image [3]. The set of binary processing commands include erosion, dilation, and region growing. These binary processing methods have proven to be effective in filtering out residual noise in classification images. However, the current methods are computationally taxing, and have difficulty in anomalous conditions. This appendix reviews alternatives to the methods used in the RL algorithm.

B.2 Erosion and Dilation

B.2.1 Traditional Definition

Erosion and dilation are traditionally defined in terms of an object $\mathbf{X}$ and a structuring element $\mathbf{B}$ [30]. Let $\mathbf{B}_x$ denote the translation of $\mathbf{X}$ so that its origin is located at x. Then the erosion of $\mathbf{X}$ by $\mathbf{B}$ is defined as the set of all points x such that $\mathbf{B}_x$ is included in $\mathbf{X}$, that is,

$$\mathbf{X} \ominus \mathbf{B} \triangleq \{x : \mathbf{B}_x \subset \mathbf{X}\}. \tag{B.1}$$

Stated simply, for every pixel in the image, the structuring element (or kernel) $\mathbf{B}$ is superimposed over the input image $\mathbf{X}$ such that the origin of $\mathbf{B}$ coincides to the input pixel x. If for *every* pixel in $\mathbf{B}$, the corresponding pixel in $\mathbf{X}$ is set, then the input pixel is remains set. If *at least one* of the pixels in the intersection are not set, however, the input pixel is cleared.

Similarly, the dilation of $\mathbf{X}$ by $\mathbf{B}$ is defined as the set of all points x such that $\mathbf{B}_x$ has a non-empty intersection with $\mathbf{X}$, i.e.,

$$\mathbf{X} \oplus \mathbf{B} \triangleq \{x : \mathbf{B}_x \cap \mathbf{X} \neq \phi\}. \tag{B.2}$$

In other words, for every input pixel x in the image X, $\mathbf{B}$ is superimposed over $\mathbf{X}$ at x. If *at least one* pixel in the structuring element coincides with a set pixel in the input image, then the input pixel x is also set. If all the corresponding pixels in the image are not set, however, the input pixel remains cleared.

B.2.2 Erosion and Dilation for RL algorithm

The RL algorithm uses a generalization of tradition erosion and dilation for a 3×3 structuring element. For RL erosion and dilation, an 8-connectivity[1] structuring element is used. Using the logical operator $\mathcal{I}$, we define $\mathcal{I}\left(\mathbf{B}_x[i] \cap \mathbf{X}\right) = 1$ if there is an intersection of $\mathbf{B}_x$ and $\mathbf{X}$ at the ith neighbor of x, and equal to zero otherwise.

[1] 8-connectivity refers to the a neighborhood of pixels directly up, down, left, right, and at each diagonal of the input pixel

The RL erosion routine can be expressed as

$$\mathbf{X} \overset{RL}{\ominus} \mathbf{B} = \{x : \sum_{i=1}^{8} \mathcal{I}\left([\mathbf{B}_x[i] \cap \mathbf{X}]^c\right) > n\}, \quad n \in \{0, \ldots, 8\}. \tag{B.3}$$

The coefficient n determines the extent of erosion. For $n = 0$, the image is eroded everywhere that pixel x has *at least one cleared neighbor*. This is equivalent to traditional erosion. By increasing n, erosion is restricted to areas where fewer neighbors are set. For $n = 8$, no erosion takes place.

Similarly, RL dilation can be written as

$$\mathbf{X} \overset{RL}{\oplus} \mathbf{B} = \{x : \sum_{i=1}^{8} \mathcal{I}\left(\mathbf{B}_x[i] \cap \mathbf{X}\right) > n\}, \quad n \in \{0, \ldots, 8\}. \tag{B.4}$$

For $n = 0$, the image is dilated everywhere that the pixel has *at least one set neighbor*. This is equivalent to traditional dilation. Again, the extent of dilation can be set by the threshold n. For $n = 8$, no dilation occurs.

In its binary processing phase, the RL algorithm uses only $n = 0$ and $n = 1$ for both erosion and dilation. As noted before, for an 3×3 structuring element and $n = 0$, Equations (B.1) and (B.3), and Equations (B.2) and (B.4) are identical. For $n = 1$, however, Equation (B.3) can be expressed as

$$\mathbf{X} \overset{RL}{\ominus} \mathbf{B}_{n=1} = (\mathbf{X} \ominus \mathbf{B}_1) \cup \ldots \cup (\mathbf{X} \ominus \mathbf{B}_8), \tag{B.5}$$

and Equation (B.4) as:

$$\mathbf{X} \overset{RL}{\oplus} \mathbf{B}_{n=1} = (\mathbf{X} \oplus \mathbf{B}_1) \cup \ldots \cup (\mathbf{X} \oplus \mathbf{B}_8), \tag{B.6}$$

where each $\mathbf{B}_i$ corresponds to each of the eight possible 3×3 structuring elements with 7-connectivity about the center pixel. Unlike tradition erosion and dilation, RL erosion and dilation is invariant to neighborhood arrangement, and only depends on the *number* of neighbors.

Due to the restriction of a 3×3 structuring element, effectively dilating or eroding by a large structuring element must be accomplished via multiple iterations of the 3×3 structuring element. This proves to be computationally intensive.

B.2.3 Fast Erosion and Dilation Approximation

Erosion and Dilation as Convolution

The process of evaluating Equation (B.3) or Equation (B.4) for each input pixel x in an image can be compared to two-dimensional discrete convolution. For the RL method, where $n = 0$, dilation becomes

$$\mathbf{X} \oplus \mathbf{B} = \min\left(1, \mathbf{X} * \mathbf{B}\right), \tag{B.7}$$

and erosion, by the duality principle, becomes

$$\mathbf{X} \ominus \mathbf{B} = \left(\min\left(1, \mathbf{X}^c * \mathbf{B}\right)\right)^c. \tag{B.8}$$

This of course, is not equivalent to RL erosion and dilation where $n \neq 0$. It should be noted that the RL algorithm dilates and erodes with $n = 0$ for the sake of preserving contour characteristics of the ice edge. A similar affect may also be accomplished by using a different structuring element; for example, a diamond or disk. By writing erosion and dilation as a convolution, well-developed linear system theory can be exploited. In procedure, however, the convolution operator would be replaced with a binary masking convolution operator to improve performance.

Erosion and Dilation in the Fourier Domain

The duality principle of the Fourier transform allows us to write,

$$\mathbf{X} * \mathbf{B} \Leftrightarrow \mathcal{F}\left(\mathbf{X}\right)\mathcal{F}\left(\mathbf{B}\right) \tag{B.9}$$

Dilation and erosion may be performed in the Fourier domain as a simple product, exploiting the speed of fast Fourier transform (FFT) algorithms. However, this is only economical for large kernels and images. In a MATLAB simulation, convolution based dilation executed faster than Fourier-based dilation for kernel sizes up to 35×35 on a fixed Antarctic egg image (1940×1940).

Structuring Element Decomposition

Linear system theory may be further exploited. A system h is separable if it can be written the convolution of two systems, $h = h_1 * h_2$. Likewise, the structuring

element **B** can often be decomposed into smaller structuring elements which, when applied in series, minimize the computational time in producing the same result as **B**. Figure B.1 shows the decomposition of several common structuring elements.

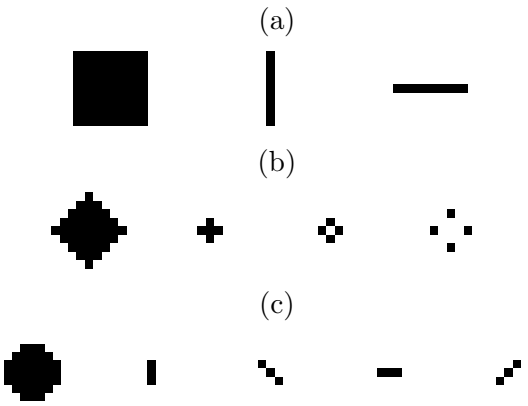

Figure B.1: Common structuring (far left) elements and their decompositions (remaining elements): (a) a 9-by-9 square decomposes into two sub-elements, (b) a diamond of radius 5 decomposes into three sub-elements, and (c) a disk of radius 4 decomposes into 4 sub-elements

Erosion and dilation procedures performed with the decomposed elements of the structuring element dramatically increases speed. For example, dilation by a 9×9 structuring element can be accomplished by dilating first with a 9×1 structuring element and then with a 1×9 structuring element. The performance improves (theoretically) by a factor of 4.5.

In MATLAB simulations, dilation and erosion via structuring element decomposition far outperformed Fourier- and convolution-based methods. Erosion and dilation can be approximated using well-developed linear system techniques. These faster operations can potentially speed up processing in the RL algorithm.

B.3 Filling and Cutting

B.3.1 RL Filling and Cutting

Large residual noise connected to the ice edge often cannot be effectively removed using erosion/dilation and region growing techniques. In the RL algorithm, large "ice" protrusions from the ice sheet and large "ocean" intrusions into the ice sheet (i.e., fingers and dents in [3]) are detected and removed using the ice mask from the previous day.

When an ice protrusion exceeds a maximum growth distance from the previous day's edge, the new edge at that location is replaced with the previous day's edge, i.e., the new edge is cut back to the old edge. Likewise, when an ocean intrusion exceeds a maximum melt distance from the previous day's edge, the new edge at that location is replaced with the previous day's edge, i.e., the new edge is filled back to the old edge.

The detection of a sea ice finger or dent is detected by dilating (or eroding) the previous day's mask by a specified length–equal to the maximum expected sea ice growth/retreat in a single day. Sea ice outside the eroded mask (or ocean inside the dilated mask) is flagged as a finger or dent.

B.3.2 Improvements

The detection of violations of sea ice growth/retreat constraints require multiple iterations of the RL dilation and erosion routines (over 50 for egg data, over 100 for slice data). This proves to be very slow, and in fact is longest computational operation in the entire RL algorithm. Computation time may drastically be reduced by simulating a large structuring element through structuring element decomposition, as described above. In a MATLAB simulation, fifty 3×3 erosion iterations was slower than a 52×52 decomposed erosion (these result in equivalent effective erosions) by a factor of 40 on a standard egg Antarctic image (1940×1940).

While cutting and filling filters out most residual edge noise, it is intolerant to anomalies. For example, Figure B.3.2 shows a case where the previous day's edge is

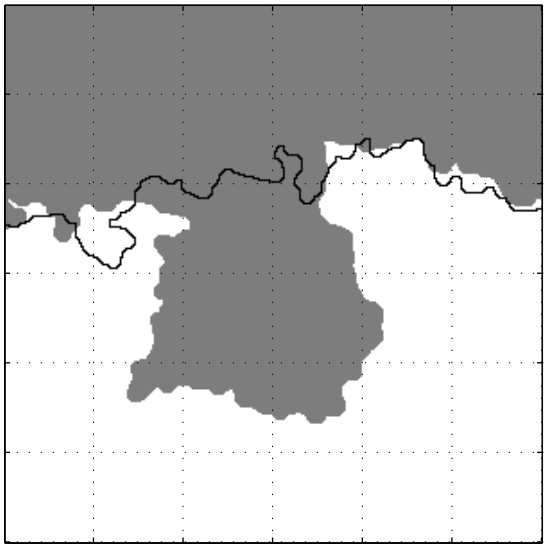

Figure B.2: Current day's ice (gray) with previous day's edge overlayed (black line)

in error.[2] The current day exhibits a large ice protrusion, and although it is correctly classified, exceeds the maximum growth distance and is cut by the RL algorithm. This problem is particularly disruptive since it propagates, i.e., each succeeding day will also be cut back until the ice retreats far enough towards the anomalous ice edge error.

A gradual recovery from such anomalies may be performed by cutting the protrusion to a *dilated* version of the previous day's ice edge. In this way, the clipped sea ice edge "grows" back into the true sea ice edge. This has been implemented in the RL algorithm at the time of printing of this thesis, as described in Chapter 3.

B.4 Ice Edge Extraction

The RL algorithm produces an ASCII file of longitude/latitude pair positions by using a spiral search contouring algorithm to locate edge pixels. This algorithm produces good results, but is computationally intensive.

[2]The previous day was misclassified and did not exceed the maximum melt distance to be corrected by a fill.

A simple method for extracting the ice edge from a mask is shown in Figure B.4. First, land is changed to ice. An eroded version of this mask is generated. The difference between the original and eroded versions produces the edge pixels. Simple ordering may be achieved by using a fast binary sort (by longitude) algorithm. This change has not been implemented.

Figure B.3: (a) image to contour (b) land changed to ice, (c) eroded image, (d) ice edge formed by subtracting image (c) from image (b)

B.5 Summary

The binary processing techniques in the RL algorithm are effective, but slow. Many steps in the binary processing sequence depend on dilation and erosion. Alternatives to RL dilation and erosion show a dramatic increase in speed at the cost of being approximations for RL dilation/erosion coefficients greater than zero. In addition, a slow recovery alternative to sea ice growth/retreat constraints are implemented to recover from large misclassification anomalies. Convolution-based erosion/dilation using structuring element decomposition (square kernel only) are implemented in the new algorithm of Chapter 4 for generating loss maps, and for spatial inclusion.

Appendix C

Local Reclassification

Under normal conditions, the Remund-Long (RL) algorithm generates satisfactory estimates of polar ice extent. In some cases, however, the sea ice maps generated by the RL algorithm contain localized misclassification errors. These misclassification errors or most commonly induced by surface melt events or persistent ocean storms. In the former case, sea ice is misclassified as ocean, and in the latter case, ocean is misclassified as sea ice.

This appendix explores the utility in reclassifying ice extent maps produced by the RL algorithm or by the new approach disclosed in this thesis. This is motivated by a desire to (1) correct misclassification errors, (2) detect polynias, and (3) adjust the reported sea ice edge to conform more closely to a desired sea ice concentration.

Part of this work was originally contained in a BYU MERS Lab internal report. Part of this work is also a direct result from a cooperative study with Joerg Haarpaintner of the National Ice Center.

C.1 Discrimination Parameters

The first motivation for performing reclassification is to correct misclassification errors. Misclassification errors are typically induced by surface melt events on the ice sheet, or by persistent ocean storms. Figure C.1 shows an example of a misclassification in the Antarctic due to persistent ocean storms. (Note the naming convention of the discrimination parameters in Figure C.1 is different from the remainder of the thesis, namely, $\gamma_{SW} = \mathrm{PR}$, $\kappa_v = V_v$, and $\kappa_h = V_h$.) In this case, the binary processing phase of the algorithm clusters together the misclassification induced by the storm.

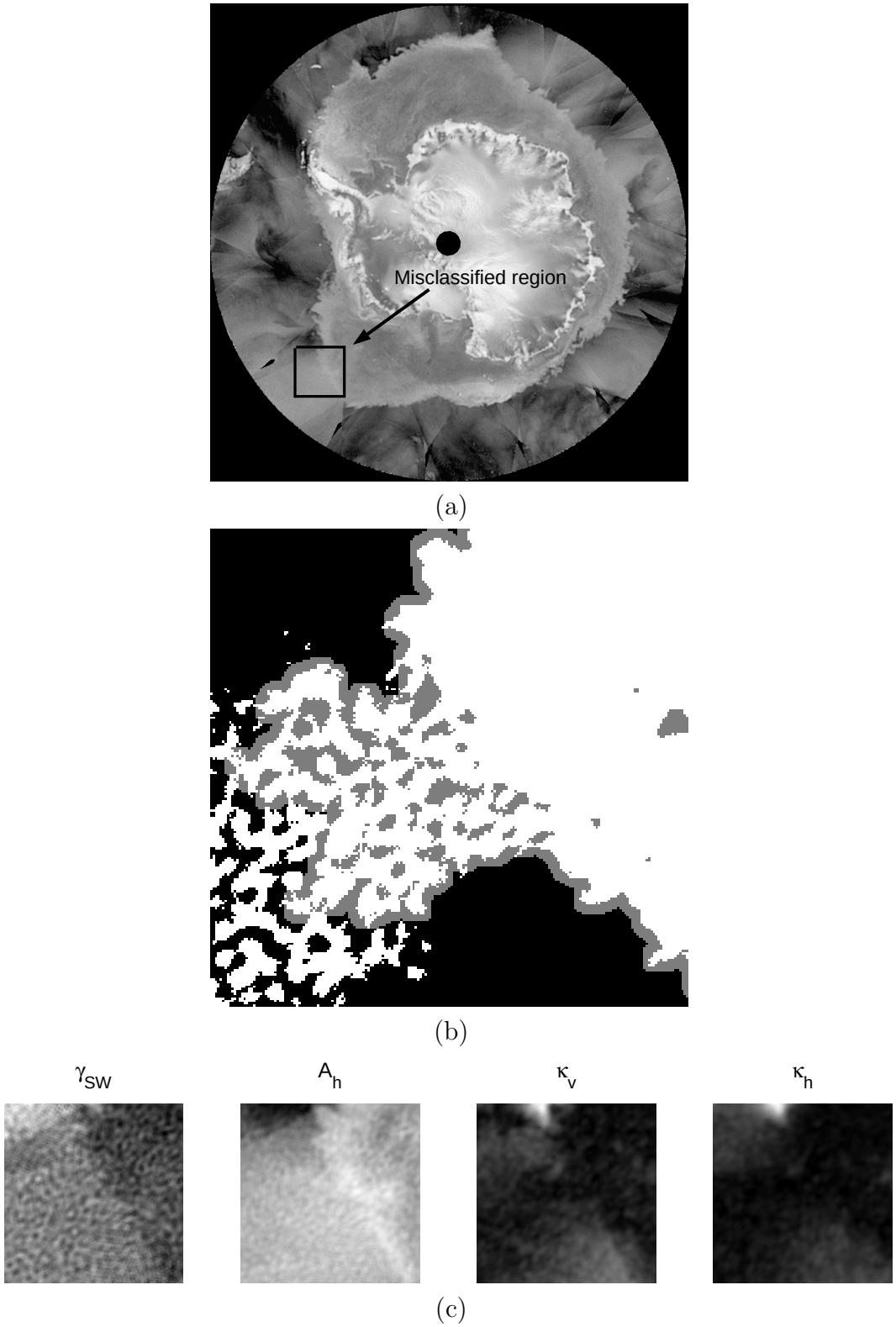

Figure C.1: Wind-induced misclassification: (a) QSCAT egg A_h image (JD 205, 2000) highlighting the region, (b) misclassified area (white=initial classification, gray=after binary processing), (c) the discrimination parameters for the region of interest.

Figure C.1 reveals some insight into the performance of each of the discrimination parameters during anomalous weather conditions. First, the polarization ratio (PR or γ_{SW}) shows good contrast between ice and ocean even during the storm. This is because PR is a function of incidence angle dependence and the depolarization caused by the medium of interest. Choppy ocean water does not severely affect these phenomena. However, since PR is computed by the difference of A_h and A_v, it suffers from amplified noise (the grainy appearance of the image) and decreased effective resolution. Each pixel is a linear combination of A_v and A_h imagery, whose effective resolutions are contained within different grids. This produces a spatial averaging effect.

The A_h imagery also reveals a bright line representing the ice edge. In this case, the high σ^o along the ice edge can be attributed to the rough new ice which forms with sea ice growth. However, the A_h imagery does not provide good contrast between sea ice and ocean when viewed as the ensemble. The brightness of the choppy ocean is nearly the same as the brightness of the inner portions of the sea ice. A_h does, however, provide the best effective resolution of the four discrimination parameters.

The variance parameters, V_v and V_h (κ_v and κ_h) are the most severely affected by the storm. Where the storm is most persistent, there is little variation in the surface scattering over the ocean between satellite passes. The variance parameters in this case are solely affected by azimuth modulation over the stormy ocean. Moreover, sea ice motion causes an increase in the variance parameters (see the top section of the variance images in Figure C.1). The low values for the variance parameters over ocean, and the high variance for mobile sea ice cause ambiguity in sea ice/ocean discrimination. Furthermore, the variance parameters are constructed in such a way (averaging) that degrades their effective spatial resolution. Note that the variance parameters were originally included in the RL algorithm to reduce spurious misclassification noise in the ocean [3].

In summary, each of the discrimination parameters exhibit strengths and weaknesses in sea ice edge detection during anomalous weather conditions. The PR exhibits the best discrimination, albeit with increased noise and decreased effective resolution. The A_h parameter yields the best spatial resolution, but yields to ambiguous decision boundaries when used univariately for sea ice discrimination. Although not discussed in this section, the A_h parameters also exhibits statistical ambiguity for surface melt events over sea ice. The variance parameters suffer from the effects of sea ice motion, surface melt events, and persistent storms, as well as degraded effective resolution.

C.2 Local Reclassification—Misclassification Correction

In light of the discussion above, two discrimination parameters—PR and A_h—are selected for a local reclassification scheme. These two parameters are selected in an effort to retain both effective resolution and high statistical contrast in anomalous weather conditions.

The RL algorithm inherently assumes ergodicity of sea ice/ocean observations in its global classification method. Although this is not an entirely bad assumption, regions with abnormal sea ice signatures are classified by the same metric as regions with nominal sea ice signatures. This presents a trouble spot for areas contaminated by anomalous weather conditions.

To ameliorate this problem, the local reclassification scheme is implemented:

1. The RL algorithm is used to get a high-level representation of sea ice extent using all four discrimination parameters.

2. The classification image is divided into sub-windows. The statistics of each sub-window are assumed to be ergotic, i.e., the statistics of individual pixels are equal to the ensemble statistics.

3. Each sub-window containing sea ice (results of the RL algorithm) is used to generate estimates of sea ice and ocean statistics.

4. Each sub-window is reclassified using a gutted-out version of the RL algorithm—only PR and A_h are used as discrimination parameters.

An important parameter in the reclassification scheme is the size of each sub-window. Each sub-window is selected such that population sizes are large enough to retrieve accurate estimates of the ensemble statistics, but small enough to assume ergodicity.

C.2.1 Reclassification Around the Sea Ice Edge

The method described above is used to reclassify sea ice maps produced by the RL algorithm. The reclassification sub-windows are restricted to lie along the sea ice/ocean interface. Sea ice and ocean statistics within the sub-window are estimated using the *a priori* estimate of sea ice location produced by the RL algorithm. The results of the local reclassification over sea ice are shown in Figure C.2 for a small window size, and Figure C.3 for a larger window size. In each case, the wind-induced misclassification has been corrected. However, reclassification with a larger window size misclassified a large number of pixels within the ice sheet.

C.2.2 Reclassification Over Entire Ice Map

Reclassification is performed again; however in this case, the sub-windows are not restricted to lie along the sea ice edge. This method may be adapted to detect polynias and leads within the ice sheet, and detect icebergs or ice floes which are disjoint from the main ice sheet. The results of the local reclassification over the entire image are shown in Figure C.4 for a small window size, and Figure C.5 for a larger window size. For the smaller window size, the misclassification error is corrected, but ocean noise is introduced. For the larger window size, the misclassification error is only partially corrected, and more ocean noise is introduced.

A reclassification scheme is developed in which the RL sea ice map is used as *a priori* data for computing local sea ice and ocean statistics. Reclassification corrects wind-induced classification errors, but also introduces misclassification errors, which may be corrected through binary processing.

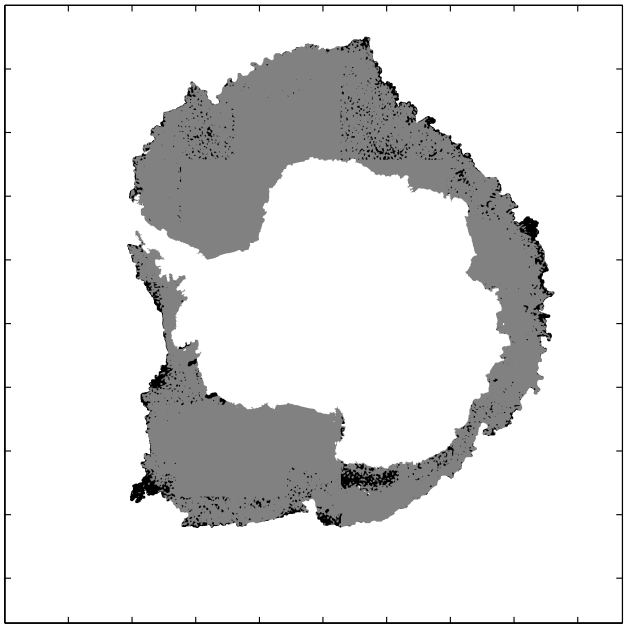

Figure C.2: Reclassification over ice using small window size (less than 12500 sea ice pixels per window). Black pixels correspond to ocean which was previously tagged as ice.

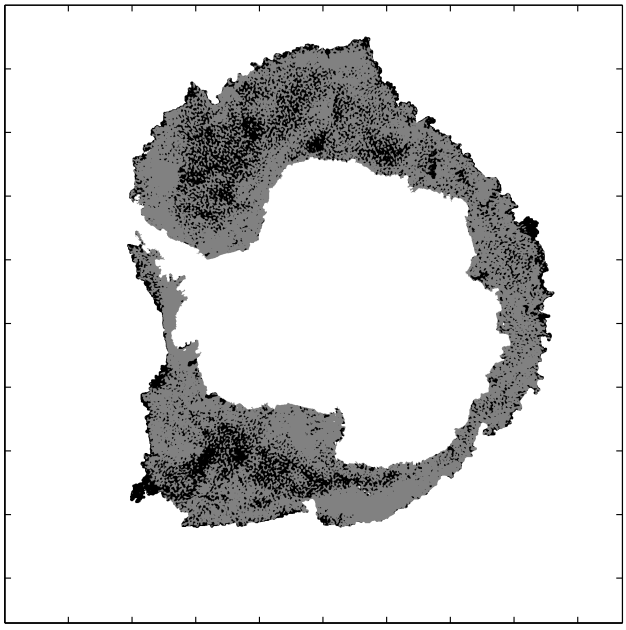

Figure C.3: Reclassification over using large window size (more than 12500 sea ice pixels per window). Black pixels correspond to ocean which was previously tagged as ice.

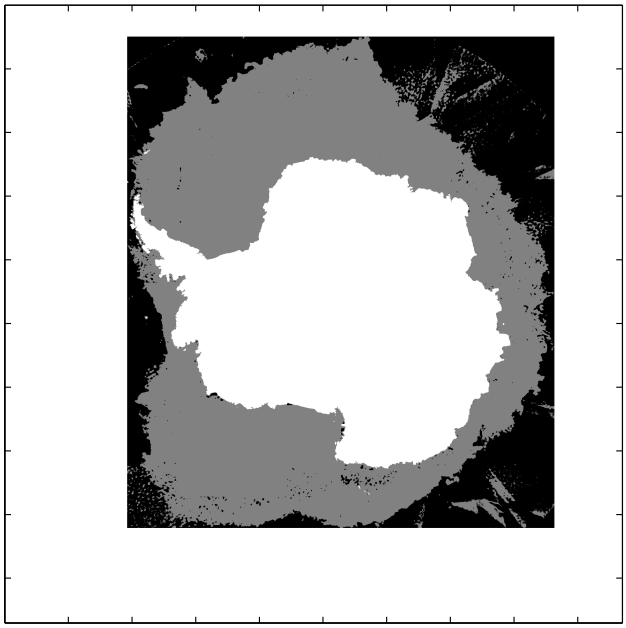

Figure C.4: Reclassification over entire sea ice map using small window size (less than 12500 ice pixels per window). The misclassification error is corrected, but more errors are introduced in the ocean.

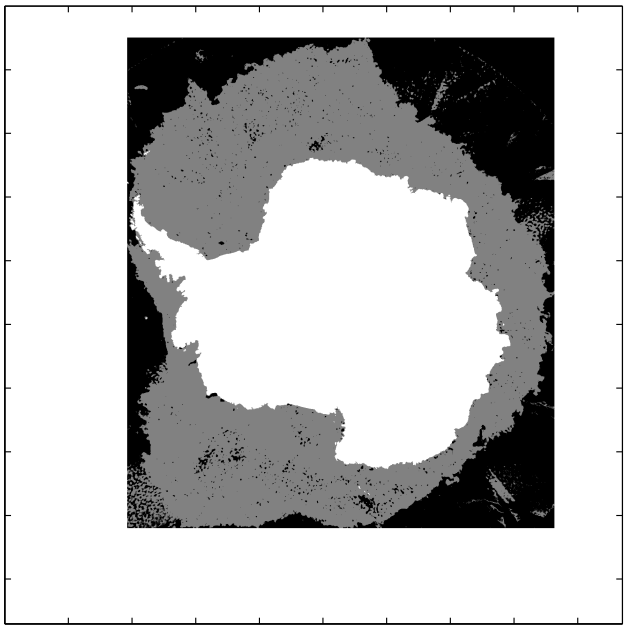

Figure C.5: Reclassification over entire sea ice map using large window size (greater than 12500 ice pixels per window). The misclassification error is only partially corrected, and more errors are introduced in the ocean.

A similar reclassification method may be implemented for detecting polynias within the ice sheet. It is suggested that the variance parameters V_v and V_h are discarded in a reclassification phase, as they are sensitive to surface melt, sea ice motion, and persistent ocean storms.

C.3 Local Reclassification to Extent Sea Ice Edge Contour

This section discusses the use of reclassification along the sea ice edge to extend the RL-reported ice edge—which typically correlates with the 30% SSM/I concentration edge—to a 15% sea ice concentration contour. The RL algorithm produces underestimates the nominal 15% ice edge primarily due to the variance parameters, V_v and V_h. As discussed above, these parameters induce classification ambiguity due to sea ice motion during the imaging interval. This is unfortunate, since the sea ice edge is in a constant state of motion. This study is a result of cooperative work with Joerg Haarpaintner of the National Ice Center.

The reclassification is motivated by the fact that the PR parameter is sensitive to depolarization of the h- and v-pol beams of the SeaWinds instrument. The extent of depolarization is related to the concentration and type of sea ice in a given area. Figure C.6 shows a scatter-plot of PR versus sea ice concentration data reported by the SSM/I NASA Team algorithm that lies within 30 km of the RL-derived ice edge. The correlation is not strong, and there is high variance, but this motivates the use of reclassification using PR to adjust the ice edge to better match a given concentration contour (15% in this case).

Sea ice pixels within 30 km of the RL-derived ice edge (extracted using dilation/erosion) are classified using a threshold on PR. Pixels which have PR values less than -0.5 (corresponding to approximately 15% sea ice concentration from Figure C.6) are classified as sea ice. The resulting classification is shown in Figure C.7. The actual sea ice concentration (average) corresponding to the new ice edge is 21%. This method may be modified to report more accurate sea ice extent estimates.

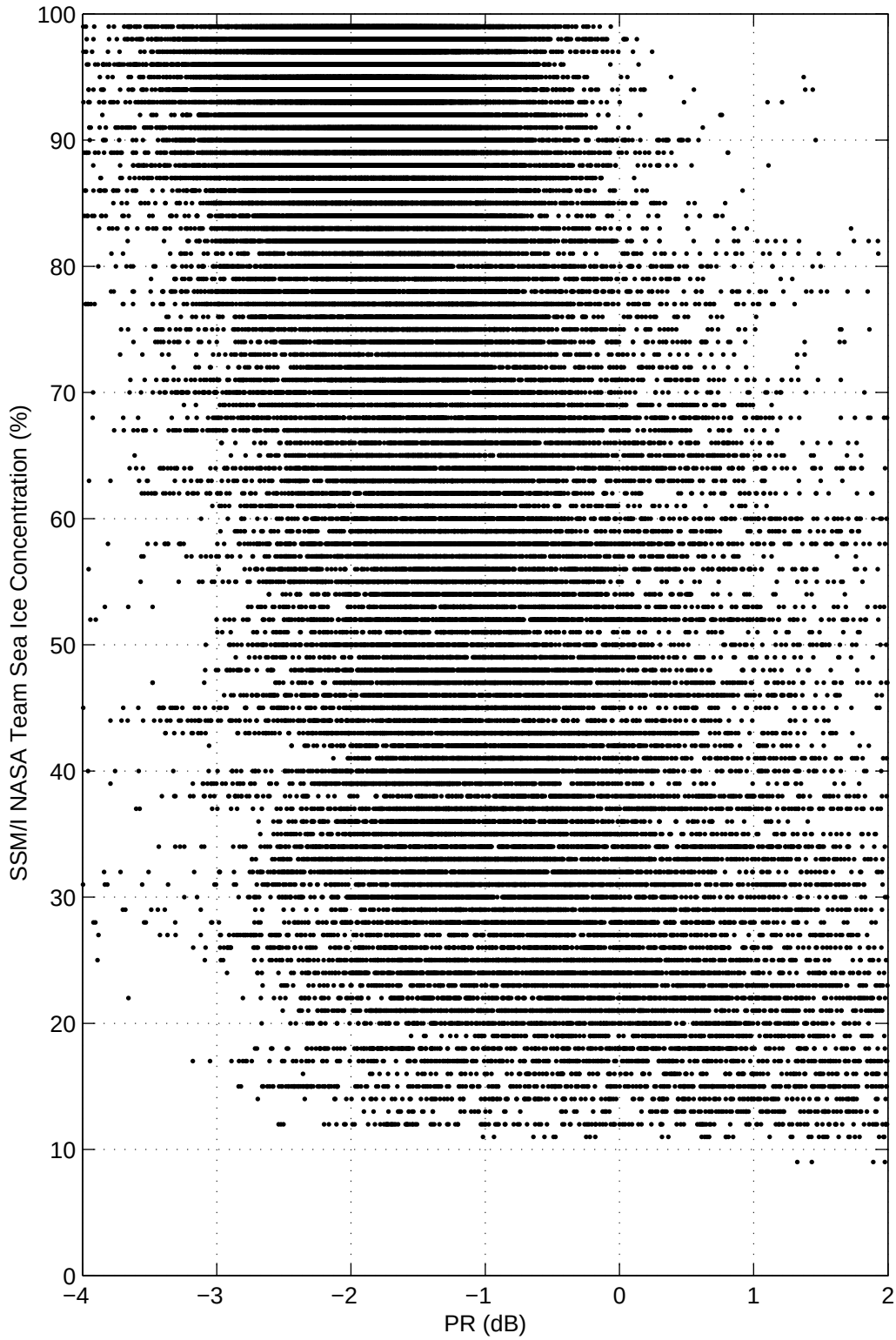

Figure C.6: Correlation of PR with SSM/I Sea ice concentration. Scatter plot is shown for all pixels within 30 km of RL-derived ice edge. The data are taken from JD 65, 2000. Note that SSM/I concentration for reported at integer values between 5 and 100%.

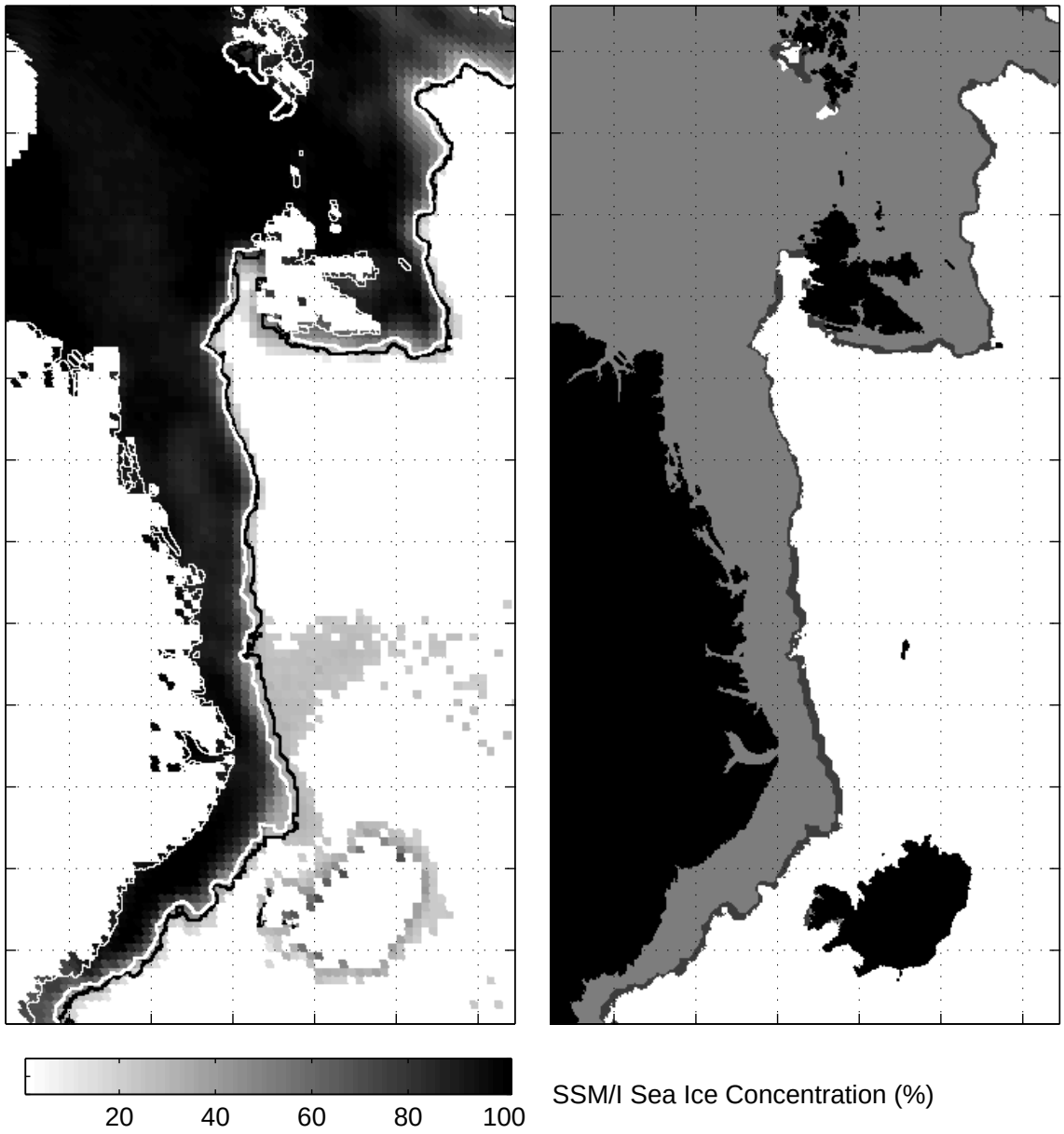

Figure C.7: Reclassification of ice edge using PR threshold. SSM/I Concentration map (left) overlayed with the original RL-derived edge (white) and PR-thresholded edge (black). (Right) This shows the difference in ice extent of the old and new edges. The dark gray line represents newly classified sea ice. Grid spacing is 250 km. (There are obvious errors in the SSM/I concentration map on the left.)

Bibliography

[1] F.T. Ulaby, R.K. Moore, and A.K. Fung, *Microwave Remote Sensing: Active and Passive*, vol. I, Artech House, Norwood, MA, 1981.

[2] Q.P. Remund and D.G. Long, "Sea Ice Mapping Algorithm for QuikSCAT and SeaWinds", *Proceedings of the International Geoscience and Remote Sensing Symposium*, vol. III, pp. 1686–1688, July 1998.

[3] Q.P. Remund, "Multisensor Microwave Remote Sensing in the Cryosphere", *Ph.D. Dissertation, Brigham Young University*, August 2000.

[4] Q.P. Remund and D.G. Long, "Sea-Ice Extent Mapping Using Ku-Band Scatterometer Data", *IEEE Journal of Geophysical Research*, vol. 104, no. C4, pp. 11515–11527, 1999.

[5] F.T. Ulaby, R.K. Moore, and A.K. Fung, *Microwave Remote Sensing: Active and Passive*, vol. II, Artech House, Norwood, MA, 1981.

[6] Q.P. Remund and D.G. Long, "Large-Scale Inverse Modeling of Microwave Backscatter from Sea Ice", *Proceedings of the International Geoscience and Remote Sensing Symposium*, pp. 494–496, July 2000.

[7] M.W. Spencer, C. Wu, and D.G. Long, "Tradeoffs in the Design of a Spaceborne Scanning Pencil Beam Scatterometer: Applications to SeaWinds", *IEEE Transactions on Geoscience and Remote Sensing*, vol. 35, no. 1, pp. 115–126, 1997.

[8] F. Naderi, M.H. Freilich, and D.G. Long, "Spaceborne Radar Measurement of Wind Velocity Over The Ocean – An Overview of the NSCAT Scatterometer System", *Proceedings of the IEEE*, vol. 79, pp. 850–866, June 1991.

[9] T. Lungu, Ed., *QuickSCAT Science Data Product User's Manual*, Jet Propulsion Laboratory, Pasadena, CA, 2001.

[10] D.G. Long, P. Hardin, and P. Whiting, "Resolution Enhancement of Spaceborne Scatterometer Data", *IEEE Transactions on Geoscience and Remote Sensing*, vol. 31, pp. 700–715, 1993.

[11] Q.P. Remund and D.G. Long, "Validation of the SIRF Resolution Enhancement Algorithm for Scatterometer Data Using SAR Imagery", *Proceedings of the International Geoscience and Remote Sensing Symposium*, vol. 2, pp. 1309–1311, 1999.

[12] F.D. Carsey, Ed., *Microwave Remote Sensing of Sea Ice*, American Geophyical Union, Washington, D.C., 1992.

[13] K. Steffen and A. Schwieger, "NASA Team algorithm for sea ice concentration retrieval from Defense Meteorological Satellite Program Special Sensor Microwave/Imager: Comparison with Landsat satellite imagery", *IEEE Journal of Geophysical Research*, vol. 96, no. C12, pp. 971–988, 1991.

[14] J. C. Comiso, D. J. Cavalieri, C. L. Parkinson, and P. Gloersen, "Passive Microwave Algorithms for Sea Ice Concentration: A Comparison of Two Techniques", *Remote Sens. Environ.*, vol. 60, pp. 357–384, 1997.

[15] Q.P. Remund, D.G. Long, and M.R. Drinkwater, "An Iterative Approach to Multisensor Sea Ice Classification", *IEEE Transactions on Geoscience and Remote Sensing*, vol. 38, no. 4, pp. 1843–1856, March 2000.

[16] J.P. Hollinger, J.L. Pierce, and G.A. Poe, "SSM/I Instrument Evaluation", *IEEE Transactions on Geoscience and Remote Sensing*, vol. 28, no. 5, pp. 781–790, September 1990.

[17] D. Cavalieri, "NASA Team Sea Ice Algorithm", http://nsidc.org/data/docs/daac/nasateam/index.html, 1996, visited 01-24-2003.

[18] S.H. Yueh, R. Kwok, S. Lou, and W. Tsai, "Sea Ice Identification Using Dual-Polarized Ku-Band Scatterometer Data", *IEEE Transactions on Geoscience and Remote Sensing*, vol. 35, no. 3, pp. 560–569, 1997.

[19] D.G. Long, "Model-Based Estimation of Wind Fields Over the Oceans from Wind Scatterometer Measurements", *PH.D. Dissertation, University of Southern California*, 1989.

[20] A.S. Fletcher, "An implementation of field-wise wind retrieval for SeaWinds on QuikSCAT", *Master's, Brigham Young University*, 2001.

[21] D.S. Early and D.G. Long, "Azimuthal Modulation of C-Band Scatterometer σ^o over Southern Ocean Sea Ice", *IEEE Transactions on Geoscience and Remote Sensing*, vol. 35, no. 5, pp. 1201–1209, 1997.

[22] Z. Liu and D. H. Bromwich, "Dynamics of the Katabatic Wind Confluence Zone Near Siple Coast, West Antarctica", *Journal of Applied Meteorology*, vol. 36, no. 2, pp. 97–118, Feb 1997.

[23] Z.A. Karian and E.J. Dudewicz, *Fitting Statistical Distributions: The Generalized Lambda Distribution and Generalized Bootstrap Methods*, CRC Press, Boca Raton, FL, 1st edition, 2000.

[24] R.L. Plackett, "A Class of Bivariate Distributions", *Biometrika*, vol. 9, pp. 159–315, 1965.

[25] K.V. Mardia, "Some Contributions to Contingency-type Distributions", *Biometrika*, vol. 54, pp. 235–249, 1967.

[26] A. Levy and M. Lindenbaum, "Sequential Karhunen-Loeve Basis Extraction and its Application to Images", *IEEE Transactions on Image Processing*, vol. 9, no. 8, August 2000.

[27] T.K. Moon and W.C. Stirling, *Mathematical methods and algorithms for signal processing*, Prentice-Hall, Upper Saddle River, NJ, 2000.

[28] J.B. Roseborough and H. Murase, "Partial Eigenvalue Decomposition For Large Image Sets Using Run-length Encoding", *IEEE Transactions on Pattern Recognition*, vol. 28, no. 3, pp. 421–430, 1995.

[29] G. Golub and C. Van Loan, *Matrix Computations*, Johns Hopkins University Press, Baltimore, MD, 1992.

[30] A.K. Jain, *Fundamentals of Digital Image Processing*, Prentice-Hall, Englewood Cliffs, NJ, 1989.